

UTTAC-73, 2005

UTTAC

ANNUAL REPORT 2004

TANDEM ACCELERATOR COMPLEX
Research Facility Center for Science and Technology
University of Tsukuba

<http://www.tac.tsukuba.ac.jp/>

UTTAC

ANNUAL REPORT 2004

April 1, 2004 – March 31, 2005

UTTAC-73 2005

Executive Editors: Hiroshi Kudo

Editors: Yoshihiro Yamato, Kimikazu Sasa, Tetsuro Komatsubara, Yasuo Nagashima

Cover photo: Summer at UTTAC.

UTTAC is a series of issues, which include annual reports of Tandem Accelerator Complex, Research Facility Center for Science and Technology, University of Tsukuba.

The issues may also include irregular reports written by English.

Copyright © 2005 by Tandem Accelerator Complex, Research Facility Center for Science and Technology, University of Tsukuba and individual contributors.

All reports are written on authors' responsibility and thus the editors are not liable for the contents of the report.

Tandem Accelerator Complex, Research Facility Center for Science and Technology,
University of Tsukuba

Tennodai 1-1-1, Tsukuba, Ibaraki 305-8577, Japan

<http://www.tac.tsukuba.ac.jp/>

annual@tac.tsukuba.ac.jp

PREFACE

University of Tsukuba Tandem Accelerator Center (UTTAC) restarted from the fiscal year 2004 as Tandem Accelerator Complex of Research Facility Center for Science and Technology. Accordingly, this is the first annual report of UTTAC under the new administration system. This annual report covers the activities during the fiscal year 2004 (1 April 2004 ~ 31 March 2005). The editorial board has decided that, from this issue, the report should include not only the research results based on the two tandem accelerators, but also the technical and maintenance activities in UTTAC.

The 12UD Pelletron tandem has been operated, overcoming two serious troubles which required the tank-opening for repair. The accelerator mass spectroscopy of ^{36}Cl has been used as a dating of modern groundwater. The hydrogen analysis with elastic recoil coincidence spectrometry has been applied to the geological research of the melt inclusions. Latent tracks of heavy ions have been applied to micro/nano-fabrication of rutile TiO_2 . In nuclear physics, systematical research of the analyzing powers in the $^6\text{Li}(d,p)^7\text{Li}$ reaction has been extended to 110 keV. The reaction mechanism for protons near the (p,n) threshold energy on ^{12}C and ^{118}Sn targets was studied. In atomic and condensed-matter physics, resonant coherent excitation of C ions in Si crystals has been observed with backward electron spectroscopy. Data compile of non-equilibrium charge states of swift heavy ions has been in progress for detailed understanding of the collision-induced charge changing processes.

The 1MV Tandetron has been used mainly for experiments with carbon cluster beams. In this year, we have found anomalous enhancement of the convoy electron yield, which should provide key information for the electronic cluster-surface interaction. The Tandetron was also used for trace-element analysis of thin foils by particle induced X-ray emission (PIXE), and for Rutherford backscattering spectroscopy (RBS) of synthesized semiconductor and magnetic films.

In this fiscal year, UTTAC organized two workshops entitled *Light Ions and Polarization Phenomena*, and *Electronic Excitation and Related Phenomena in Atomic Collisions 2005*. Also, 13 UTTAC seminars were held to stimulate research activities. It is worth noting that UTTAC accepted a series of accelerator-facility tour for totally 916 visitors this year, of which 598 are high-school students. UTTAC will continue such social services for promotion of ion-beam based science and technology, especially in the next generation.

Finally, Professor Y. Nagashima has succeeded the director of UTTAC, effective on 1 April 2005. Also, our colleagues, Professors K. Shima and Y. Tagishi, have retired on 31 March 2005. Their academic, technical, and administrative contribution to UTTAC since 1970s is greatly acknowledged.



Hiroshi Kudo
Director

CONTENTS

1. ACCELERATOR AND EXPERIMENTAL FACILITIES	
1.1 Accelerator operation 2004	1
1.2 Developments of tilted electrode gas ionization chamber	4
1.3 Application of ultrathin silicon detector in low energy nuclear reaction measurement	6
2. NUCLEAR PHYSICS	
2.1 Analyzing powers for the ${}^6\text{Li}(d,p_1){}^7\text{Li}$ reaction at incident energy of 110 keV	9
2.2 Proton total reaction cross section on ${}^{12}\text{C}$ near (p,n) threshold energy	10
2.3 ${}^{118}\text{Sn}(d,p)$ reaction in search for Coulomb stripping of deuteron II	12
2.4 Production of polarized ${}^{20}\text{F}$ by polarized deuteron beam and the beta-ray angular distribution	14
2.5 Nucleosynthesis of the p-nuclei	16
3. ATOMIC AND SOLID STATE PHYSICS, AND CLUSTER SCIENCE	
3.1 Fragments of accelerated atomic cluster ions	17
3.2 Resonant coherent excitation of C^{5+} observed with backward electron spectroscopy	19
3.3 Yield of secondary electrons induced by fast cluster ions	21
3.4 Abundance spectra of neutral metal clusters produced by magnetron-sputter-type gas aggregation cluster source	23
3.5 DSMC simulation of magnetron-sputter-type gas aggregation cluster source	24
3.6 Reactions between Ni_{13} cluster and oxygen atoms	25
3.7 Pulsed extraction of cluster ions from magnetron sputtering gas aggregation cluster source	27
3.8 Molecular dynamics calculations on hybrid clusters composed of Au atoms and Lennard-Jones atoms	29
3.9 The science of 3d transition-metal oxide system (2004-2005)	30
3.10 RBS characterization of various thin films	32
4. ION BEAM ANALYSIS AND APPLICATION	
4.1 Status of Tsukuba AMS system	33
4.2 Use of ${}^{36}\text{Cl}$ as a dating tool for modern groundwater	35
4.3 AMS of ${}^{36}\text{Cl}$ in shielding concrete of various accelerator facilities	37
4.4 Latent tracks and etched tracks in rutile TiO_2 single crystals	39
4.5 Radio isotope implantation using a sputtering negative ion source	41
4.6 Measurement of He distribution in 40keV He irradiated stainless steel by means of ERDA with 16MeV O^{5+} beam	42
4.7 Shape measurement of melt inclusion in a mineral sample	44
4.8 Development of ERCS hydrogen analysis for geological samples	46
4.9 Trace element determination of silicate rock reference material JB-1a by using particle-induced X-ray emission	48

5. TECHNICAL REPORT	
5.1 Design of a new beam slit system for beam analyzing magnet	51
5.2 Development of a beam slit controller by using XPort and Web I/O	53
6. RELATED TOPICS	
6.1 Mass measurements by isochronous storage ring in RIKEN RI beam factory	55
6.2 Design of the isochronous storage ring and the injection line for mass measurements in RIKEN RI beam factory	56
6.3 Reaction of gold cluster cations with silane at high temperature	57
7. LIST OF PUBLICATIONS	
7.1 Journals	59
7.2 Internal conferences	64
8. THESES	66
9. SEMINARS	67
10. SYMPOSIA	68
11. LIST OF PERSONEL	70

1.

ACCELERATOR AND EXPERIMENTAL FACILITIES

1.1 Accelerator operation 2004

K. Sasa, S. Ishii, T. Takahashi, Y. Yamato, H. Kimura, H. Oshima, Y. Tajima, K. Shima, T. Komatsubara and H. Kudo.

The 12UD Pelletron tandem accelerator

The total operating time and the experimental beam time were 1788.0 and 1364.0 hours, respectively. The operating time was about 87.3 % relative to that in 2003. Fig.1 shows the accelerator operation hours per month. The beam time histogram with respect to the terminal voltage is shown in Fig.2.

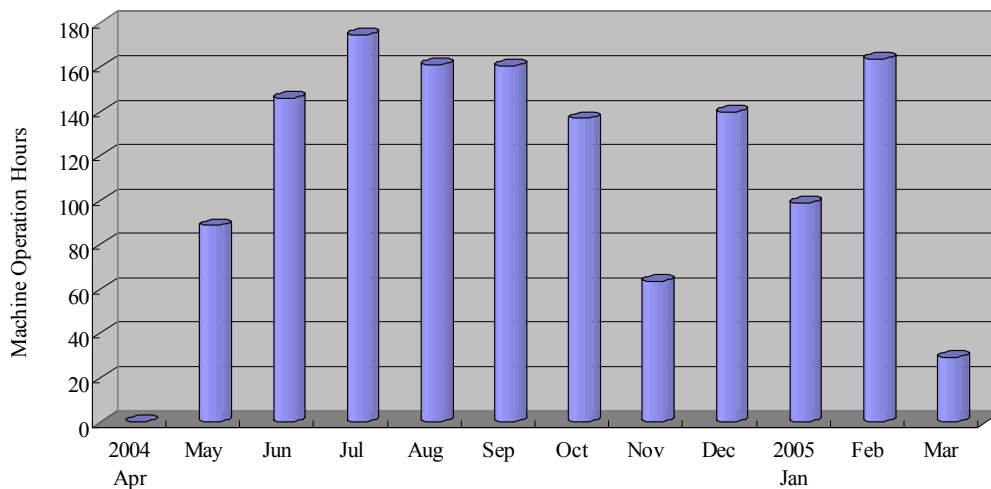


Fig.1. Accelerator operation hours per month for the fiscal year 2004.

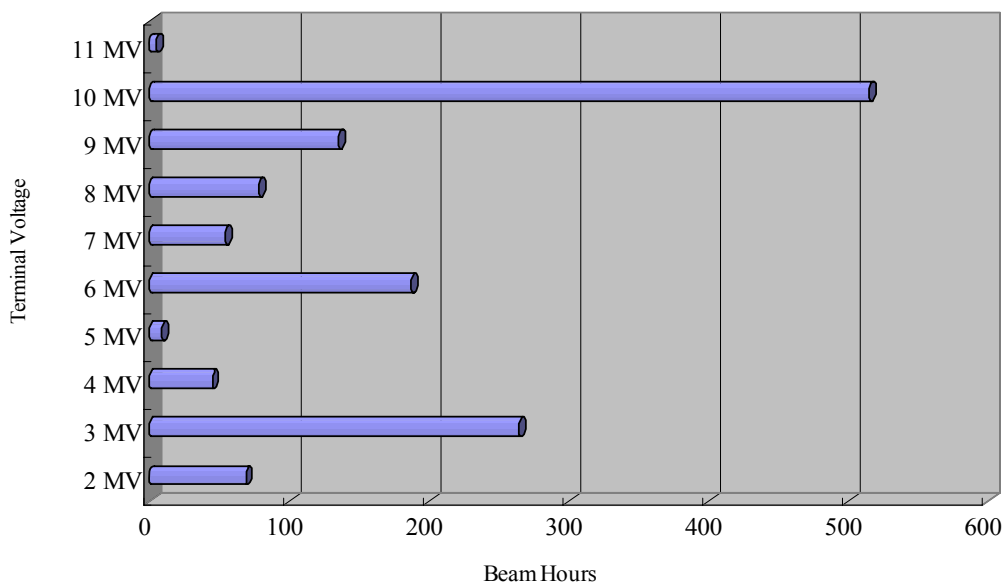


Fig.2. Beam time histogram as a function of the terminal voltage.

Fig.3 represents percentage operation time of the three ion sources and ion species. Fig.4 shows the percentage of experimental beam time of the running research fields.

On May and November 2004, the operation of the 12UD Pelletron tandem accelerator was in unstable state. We opened the accelerator tank and repaired the breakdown of the accelerator.

The scheduled maintenance in the spring 2005 was started on March 3 and finished on May 6. The image and the object slits for the analyzer magnet were replaced by the motorized slits for remote operation. Also, we have installed a new steering magnet in the second target room for control of the beams after passing through the analyzer magnet. The technical details are described in Chap. 5 of this annual report.

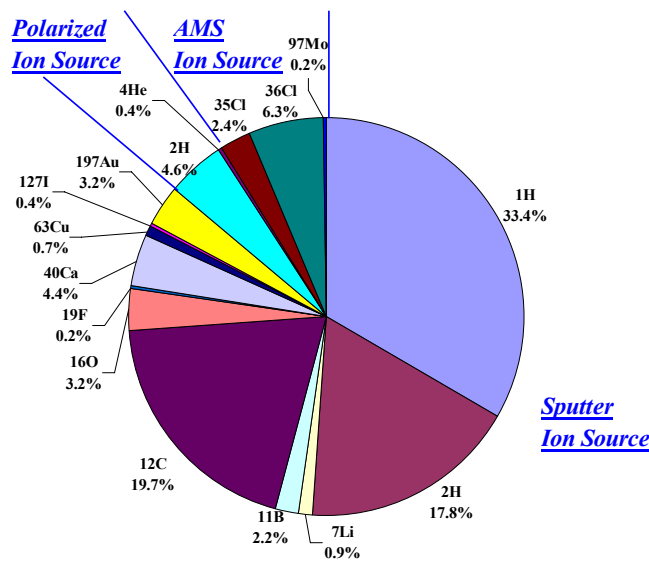


Fig.3. Percentage operation hours of the three ion sources.

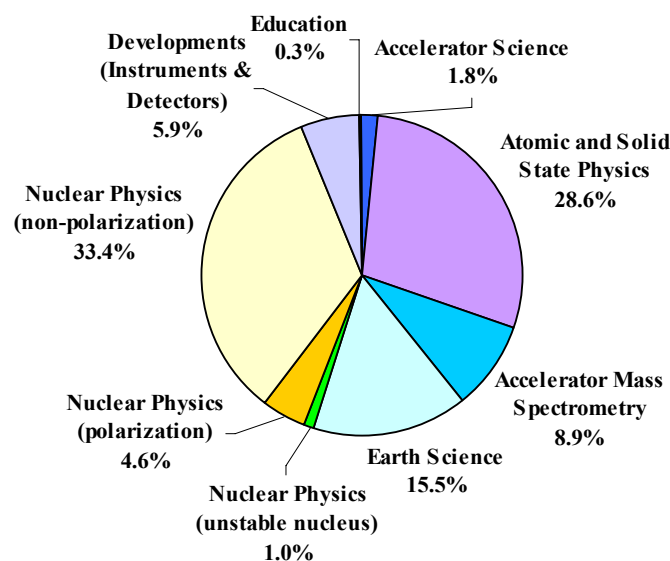


Fig.4. Percentage experimental beam time of the research

The 1MV Tandetron accelerator

The total experimental beam time of the 1MV Tandetron accelerator was 772.2 hours in the fiscal year 2004. The experimental beam time was about 222.7 % relative to that in 2003. Fig.5 shows the percentage of experimental beam time of the running research fields. The main research field of the 1MV Tandetron accelerator was the cluster physics. A research program, “Fast cluster impact processes”, including electron emission, sputtering, radiation damage, secondary particle emission has been under way using the 1MV Tandetron accelerator. The 1MV Tandetron accelerator was also used for trace-element analysis with particle induced X-ray emission (PIXE) and Rutherford backscattering spectroscopy (RBS).

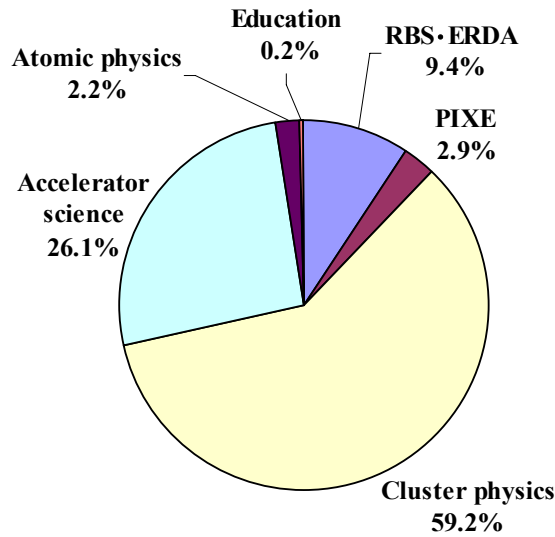


Fig.5. Percentage of experimental beam time of the running research fields with the 1MV Tandetron accelerator.

1.2 Developments of tilted electrode gas ionization chamber

T.Yasuno, A.Ozawa, A.Chiba, M.Yamaguchi, Y.Tagishi, T.Oonishi¹, K.Kimura²

We are developing tilted electrode gas ionization chambers (TEGIC) as energy-loss detectors to be used for high counting-rate experiments at RIKEN [1]. Cross-sectional view of the TEGIC is shown in Fig.1. In the TEGIC, beams pass through layers of tilted anode and cathode foils with 4 μm thickness. The thickness of the foils should be as thin as possible since the foils are dead layers for energy-loss measurements. Thus, we made new anode and cathode foils with 2 μm thickness. Tilted angle of the anode and cathode foils was originally 60° from the horizontal axis. However, the tilted angle was not optimized so far. To optimize the tilted angle, we measured energy resolution of the TEGIC by changing the tilted from 90° to 50° by 10°.

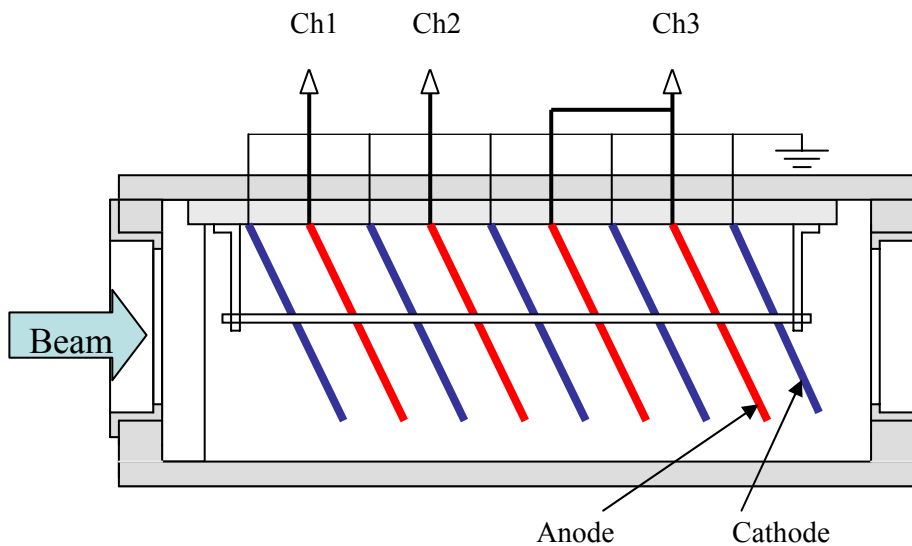


Fig.1. Cross-sectional view of TEGIC

The experiment was carried out at the 12UD Pelletron tandem accelerator. Ion beam of ^{12}C nucleus was accelerated to 60MeV. The ^{12}C ions, which were scattered elastically by a gold target, were irradiated to the TEGIC. Beam intensity was typically 10^4 cps. The TEGIC was operated using P-10 gas with 124.5 Torr. The energy resolution of the TEGIC with 2 μm thick foils was identical to the one with 4 μm thick foils. The tilted angle dependences of the energy resolution are shown in Figure 2. The energy resolution of ch1 and ch2 in the TEGIC becomes better as the tilted angle of the foils approaches to 90°. Further analysis is in progress.

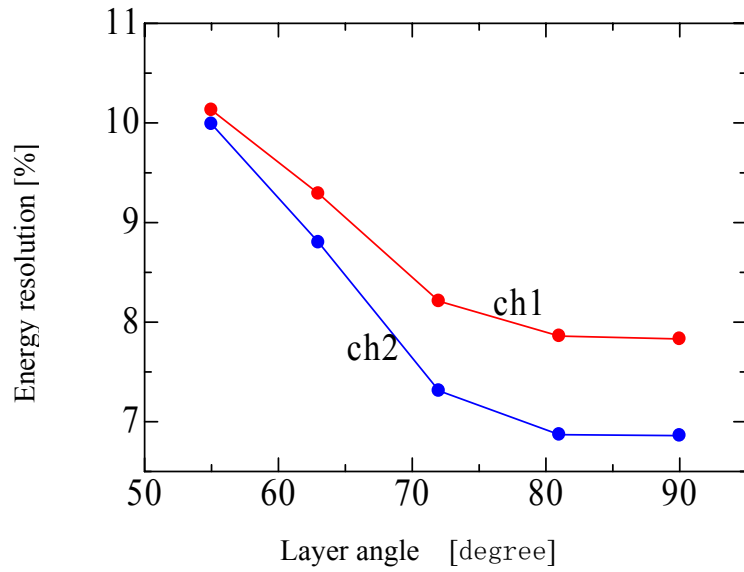


Fig.2. Tilted angle dependence of the energy resolution. Results of ch3 are not shown due to poor resolution by the noise.

References

- [1] K.Kimura, et al., Nuclear Instrumental & Methods in Physics Research A 538 (2005) 608-614

1 The Institute of Physical and Chemical Research (RIKEN), Wako, Saitama, 351-0198 Japan

2 Nagasaki Institute of Applied Science, 536 Abamachi, Nagasaki 851-0193 Japan

1.3 Application of ultrathin silicon detector in low energy nuclear reaction measurement

S. Nishimura¹, H. Fujikawa², M. K-Nishimura¹, S. Kubono², M. Kurokawa¹, J. J. He², T. Motobayashi¹, Y. Tagishi, H. Yamaguchi², and M. Yamaguchi

Recent progress in high-power accelerator facilities has enabled the study of nuclear reactions in the low-energy frontier, which is essential to clarify the astrophysical nucleosynthesis that occurred in the early stages of the Big Bang as well as the rapid-neutron capture process in supernovae explosions. In this scenario, the path ${}^4\text{He}(t,\gamma){}^7\text{Li}(n,\gamma){}^8\text{Li}(\alpha,n){}^{11}\text{B}(n,\gamma){}^{12}\text{B}(\beta,\nu){}^{12}\text{C}$ is a key reaction flow for explaining the synthesis of ${}^{12}\text{C}$ and heavy elements according to full network calculations[1]. While, the most interesting energy region of data below 1 MeV is missing due to the difficulties of particle identification of low-energy ions from the background particles.

A new experimental approach for exploring these low-energy nuclear reactions using a monolithic silicon telescope (MST) has been studied using the simulation code GEANT4 [2]. Our feasibility study indicates that the ultrathin silicon detector could be applied to the measurements of the low-energy nuclear reaction products as a novel technique. In this article, the performance of the MST will be reported using low-energy ${}^{11}\text{B}$ and ${}^7\text{Li}$ ions from an accelerator together with α particles from a source (${}^{241}\text{Am}$).

The primary beam of ${}^{11}\text{B}$ and ${}^7\text{Li}$ ions accelerated up to 12 MeV by the Pelletron tandem accelerator at UTTAC is first degraded and scattered by a $\sim 3\ \mu\text{m}$ Au foil. The energies of ions are roughly adjusted by altering the angle of the Au foils and chosen by adjusting the downstream magnetic setting of a spectrometer (Q-D-Q magnets) tilted at a 35 degree angle. Two different sizes of collimator with hole sizes of 3 and 10 mm ϕ are installed in front of the MST at the end of the spectrometer. A single MST consists of two 508- μm -thick silicon detectors (E) assembled on a 14 pin IC socket. In addition, five ultrathin silicon pads (ΔE) of 1 μm thickness are arranged on the surface of each of the E layers [3]. Two signals from the ΔE and E layers provide the dE/dx and the total energy deposited by the incident ions, simultaneously. The size of each ΔE pad is set to $3 \times 4\text{mm}^2$ to reduce the capacitance down to 2 nF in order to reduce the noise level with the use of a standard preamplifier. The signals from the preamplifiers go to shaping amplifiers (ORTEC 641) for precise pulse height measurements. Data is gathered using a self-triggering mode on the MST, requiring a minimum energy deposit of above ~ 100 keV in one of the ΔE pads. Figure 1 shows the compiled scatter plot between ΔE and E in arbitrary units for ${}^{11}\text{B}$ and ${}^7\text{Li}$ ions. The figure was created by superimposing the data taken at different magnetic settings of the spectrometer. The α particles data is also added using an ${}^{241}\text{Am}$ source under the slow pressure control of air as an energy degrader. Our result suggests that the MST has an excellent capability for identifying the low-energy ${}^{11}\text{B}$ from the ${}^7\text{Li}$ ions and α particles down to the energy of 0.11 MeV/u, which is the lowest separation energy of this detector as determined by the stopping range of the incident ${}^{11}\text{B}$ ions within the first ΔE layer. The bands in the low ΔE region correspond to the hit events on other pads. The incident angle dependence of the energy spectrum is also measured by changing the angle of the MST with respect to the direction of the incident particles. Our preliminary results show possible channeling effects of the incident ions in the ΔE

¹RIKEN

²Univ. of Tokyo, CNS

layer at the particular angle of the incident ions to the MST around 0 degrees (perpendicular). This effect disappears within 2.5 degrees and shows up again around 35 ~ 40 degrees. Fortunately, this feature is expected to be negligible because our design of the MST allocation and its kinematics in the gas target will result in fewer occurrences of these events.

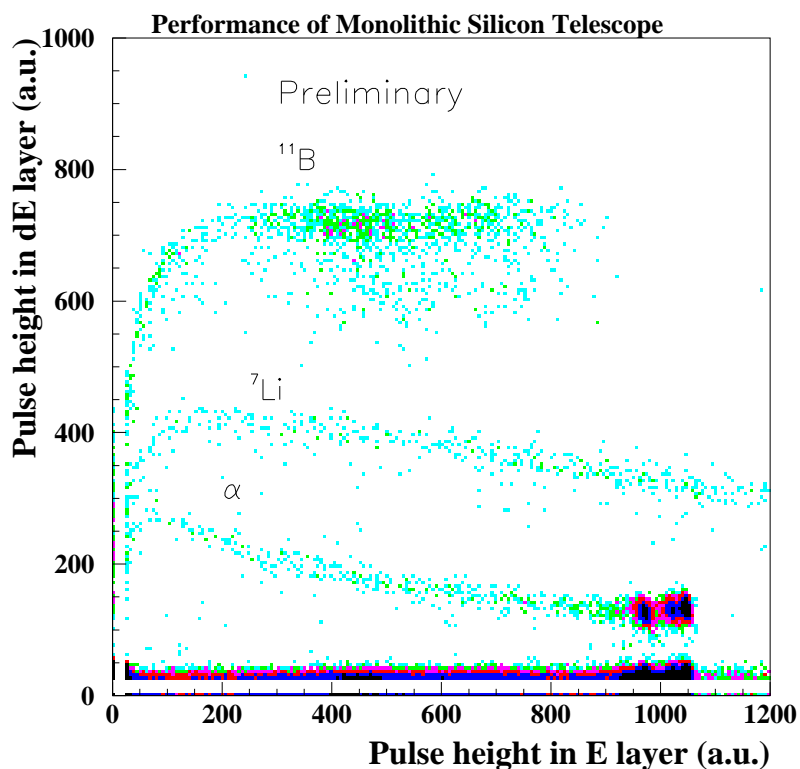


Fig. 1. Correlation between the energy deposited in ΔE and E layers by different incident ions. The clear separation among the ^{11}B and ^7Li , and α particles in the low-energy region evidences the excellent performance of the MST for the $^8\text{Li}(\alpha, n)^{11}\text{B}$ reaction measurement.

References

- [1] M. Terasawa et al.: *Astro. J.* **562**, 470 (2001).
- [2] M. K-Nishimura et al.: *RIKEN Accel. Prog. Rep.* **37**, 183 (2004).
- [3] A. Musumarra et al.: *Nucl. Inst. Meth. A* **409**, 414-416 (1998).

2.

NUCLEAR PHYSICS

2.1 Analyzing powers for the ${}^6\text{Li}(d,p_1){}^7\text{Li}$ reaction at incident energy of 110 keV

M. Yamaguchi, T. Shinba and Y. Tagishi

Analyzing powers for the ${}^6\text{Li}(d,p_1){}^7\text{Li}$ reaction at incident energy of 110 keV were measured. The experimental setup is almost the same as the one in Ref.[1]. At this time, we shortened the distances between the target and the detectors because the cross section of this reaction is smaller than that of the ${}^6\text{Li}(d,p_0){}^7\text{Li}$ reaction. Fig. 1 shows the result of the experiment. In forward angles, we could not separate the p_0 and p_1 peaks in spectra. Consequently, those data have large ambiguity, so we omitted those data. Lines in the figures represents the result of the analysis in terms of (l,s,J) reaction matrix elements. Details of the analysis was explained in Ref.[1]

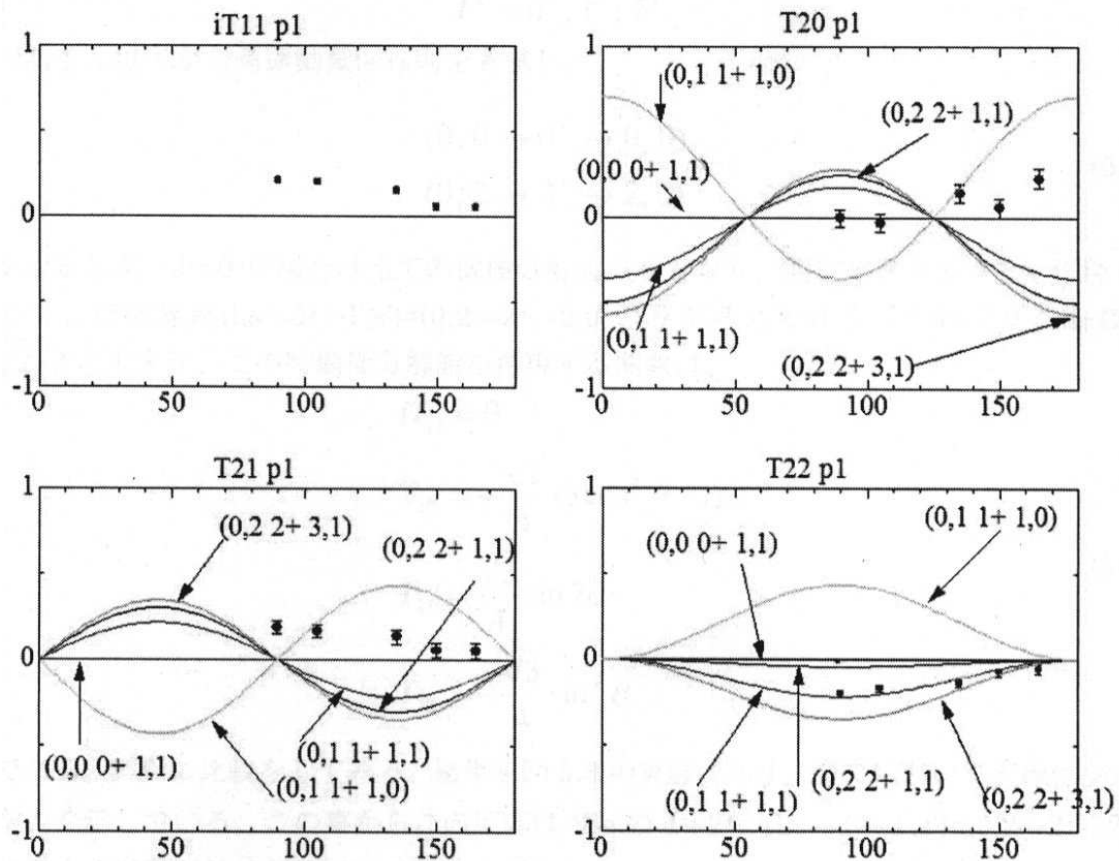


Fig. 1. Results of the experiment and the analysis in terms of (l,s,J) reaction matrix elements.

References

- [1] M. Yamaguchi, Y. Yoshimaru and Y. Tagishi, UTTAC annual report 2003 (2004) 17

2.2 Proton total reaction cross section on ^{12}C near (p,n) threshold energy

T.Ishikawa, M.Iijima, S.Igarashi, Y.Ito and Y.Aoki

Resonance like behavior may be expected in the energy dependence of nucleon-nucleus effective potential [1] near the nucleon transfer reaction threshold energy. We think that this anomaly appears especially in energy dependence of total reaction cross section σ_R near (p,n) threshold energy. In 1995 we started development of measuring system of σ_R , and observed the anomaly in $^{nat}\text{Si}+p$ system in 2000 [2]. Since 2003, We are trying to observe the anomaly in $^{12}\text{C}+p$ system.

We use attenuation method [3] in measurement of σ_R , which uses the following expression,

$$\sigma_R = \frac{1}{nx} \left(\frac{I_0 - I}{I_0} - \frac{i_0 - i}{i_0} \right)$$

where I_0 and i_0 are the number of projectiles, I and i are the number of ejectiles and nx is the nucleon density of target ^{12}C . Upper case and lower case letters in this expression correspond to target in/out measurement, respectively. Fig.1 shows the experimental arrangement of counters and target. Target thickness is 8.0 and 16.0 mg/cm^2 . Counting detectors of I_0 and I are proportional counter and plastic scintillation counter respectively. Details of attenuation method and our measuring system are described in [4].

In 2004 we improved following points in measuring system, 1) minor change of the system of upstream active slit and I_0 counter(Fig.1), 2) improvement of target positioning system. Target positioning accuracy is $\pm 0.5 \text{ mm}$.

Measured σ_R however was not very stable, i.e., attenuation rate $(i_0 - i)/i_0$ varied occasionally. We thought that the source of the error is due to fluctuations of beam intensity and pressure in proportional counter. By reducing these fluctuations, the error is decreased than that of last year. And we measured energy dependence of σ_R in February, 2005 (Fig.2).

The present results are compared with those of Makino et al.,[5] in Fig.2. Absolute value of our data is not reliable, because elastic and inelastic corrections are not properly made yet. Error bar, however, include some elastic corrections.

In near future, we will clear up those difficulties (reduction of measurement error and correction of systematic error). And we will also introduce the beam diffuser for stabilizing the beam intensity.

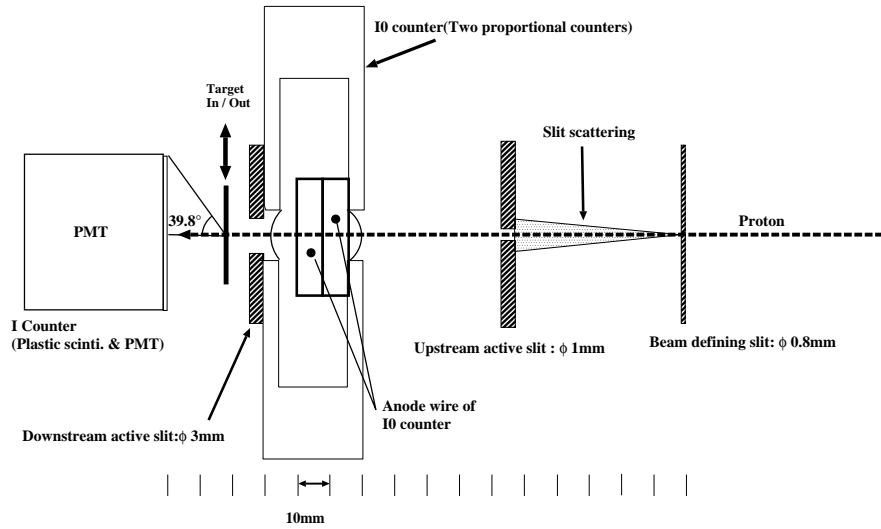


Fig. 1. Cross-sectional view of measurement system

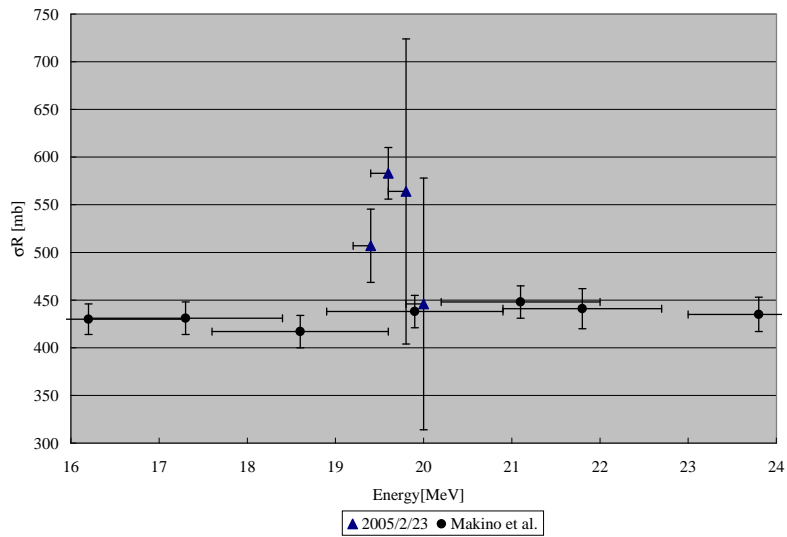


Fig. 2. Energy dependence of σ_R in $^{12}\text{C}+p$ system ($Q_{(p,n)}^{lab} = -19.63\text{MeV}$). Energy is the laboratory value. 2005/02/23 is present data. Another one is the data of Makino *et al.*[5].

References

- [1] N.K.Glendenning, Direct Nuclear Reactions(1983), Academic Press
- [2] N.Okumura, Doctral Thesis, University of Tsukuba, 2000
- [3] T.J.Gooding *et al.*, Nucl. Phys. **12**, 241(1959)
- [4] T.Ishikawa, Graduation Thesis, University of Tsukuba, 2004
- [5] M.Q.Makino *et al.*, Nucl. Phys. **68**, 378(1965)

2.3 $^{118}\text{Sn}(\text{d},\text{p})$ reaction in search for Coulomb stripping of deuteron II

M.Iijima, Y.Aoki, S.Igarashi, T.Ishikawa, Y.Ito, Y.Tagishi and M.Yamaguchi

In order to estimate the effect of Coulomb breakup of deuterons below Coulomb barrier, we started an experiment to measure energy dependence of differential cross section $\sigma(\theta)$ for $^{118}\text{Sn}(\text{d},\text{p}_0)$ reaction. In February 2004, we measured $\sigma(\theta)$ at $E_{\text{lab}} = 7.5, 8.0$ MeV [1].

We subsequently measured $\sigma(\theta)$ at $E_{\text{lab}} = 4.5 \sim 7.0$ MeV and the details will be described here. The experiments were carried out in July and August 2004 using 12 UD Pelletron at UTTAC. The target was ^{118}Sn of 4.8 mg/cm^2 thick with 95.75 % enrichment. Detectors were two sets of $E - \Delta E$ counter telescopes, each of which was comprised of two identical SSDs with $28 \times 28 \text{ mm}^2$ active areas. Solid angles of the detectors were approximately 40 and 60 msr. We also installed a monitor counter at $\theta_{\text{lab}} = 45^\circ$. Beam current on target was less than 1 nA to keep deuteron count rate below 1000cps, which was required to prevent pile-ups of electronic signals.

Fig.1(a) and Fig.1(b) are the spectra taken at $E_{\text{lab}} = 6.0$ MeV for deuterons and protons, respectively. In fig.1(a) we see peaks of elastically scattered deuterons from ^{12}C , ^{16}O and ^{118}Sn . Fig.1(b) shows peaks of protons from $^{118}\text{Sn}(\text{d},\text{p})$ reactions leading to the ground state and 1.250 MeV excited state of ^{119}Sn . We emphasize here that both states have orbital angular momenta of $\ell_n = 0$. Though there should be several excited levels with $\ell > 0$ between these two levels, yield to these levels might be suppressed due to low orbital angular momenta of the incident deuterons.

Fig.2 shows excitation curve for $^{118}\text{Sn}(\text{d},\text{p}_0)$ reaction. Experimental points are arithmetic averages of $\sigma(\theta)$ between $\theta_{\text{lab}} = 110^\circ \sim 155^\circ$ because we did not measure $\sigma(\theta)$ at forward angles. We also take the arithmetic averages of DWBA values between $\theta_{\text{lab}} = 110^\circ \sim 155^\circ$ and these values are multiplied by the factor of 1.51 for the normalization at $E_{\text{CM}} = 6.88$ MeV. We also calculated Gamow's theoretical values using the following equation:

$$\sigma(E) = \frac{S(E)}{E} \exp(-2\pi\eta)$$

The values thus obtained were also multiplied by a constant to be normalized at $E_{\text{CM}} = 6.88$ MeV. After the normalizations we can conclude that DWBA calculations fit experimental values considerably well. Since Coulomb breakup should get enhanced at lower energy [2], we are going to measure $\sigma(\theta)$ at incident energy lower than 4.5 MeV.

References

- [1] M.Iijima, Y.Aoki, N.Okumura, H.Ishiguro, S.Igarashi, T.Ishikawa, M.Yamaguchi and Y.Tagishi, UTTAC ANNUAL REPORT, 11(2003)
- [2] Y.Aoki, N.Okumura, H.Ishiguro, UTTAC ANNUAL REPORT, 22(2002)

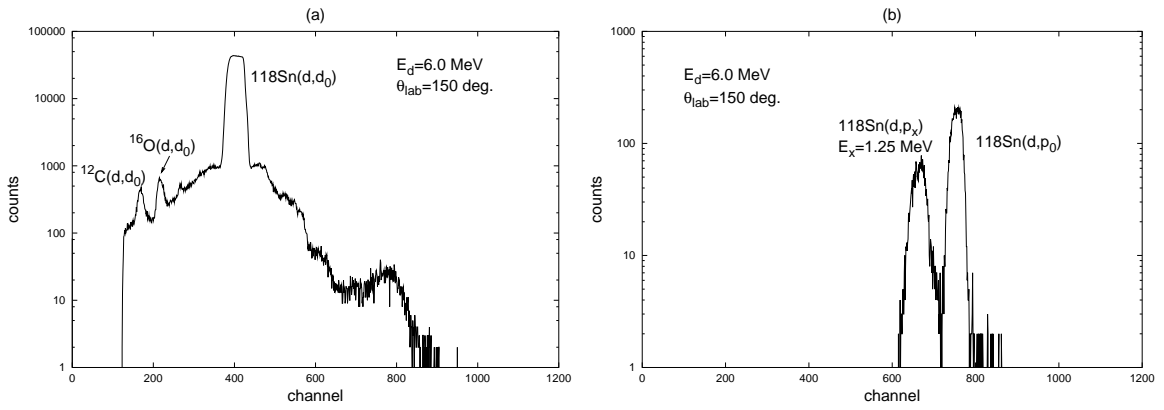


Fig. 1. Spectra of (a)deuterons and (b)protons

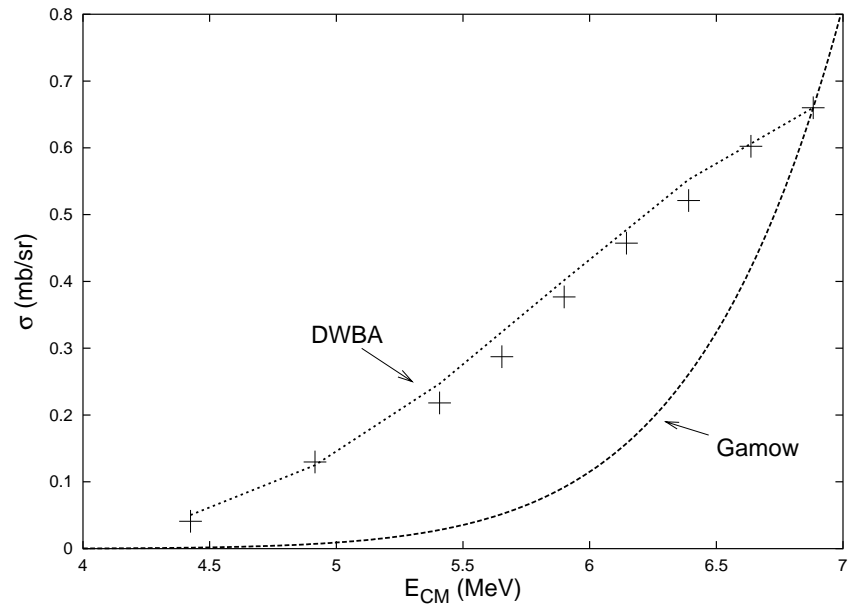


Fig. 2. Excitation curve for $^{118}\text{Sn}(d,p_0)$ reaction. + denotes experimental points. The curves referred to as 'Gamow' and 'DWBA' are explained about in detail in the text.

2.4 Production of polarized ^{20}F by polarized deuteron beam and the beta-ray angular distribution

K. Matsuta¹, Y. Tagishi, T. Nagatomo¹, A. Ozawa, M. Yamaguchi, H. Fujiwara¹, T. Yasuno, A. Chiba, R. Matsumiya¹, M. Mihara¹, M. Fukuda¹, K. Minamisono² and T. Minamisono³

The Lamb shift type polarized ion source in Univ. of Tsukuba Tandem Accelerator Complex (UTTAC) is very helpful for various fields of physics including nuclear structure and reactions, and fundamental interactions in β decay. It provides unique chances to measure nuclear moments and very precise β -ray angular distributions, utilizing the polarization transfer through the light ion reactions such as (d,p), (d,n), (p,n) (p, α) reactions with polarized incident beams. This polarization technique has been established in the 1970's at Stanford Univ. and been applied for the nuclear moment measurements [1]. We applied this polarization technique to the precise measurement of the β -ray angular distribution, especially the alignment correlation term, which is a unique probe of the G-parity irregular term in the weak nucleon currents and the meson exchange effect in the nucleus. In the present study, the polarization transfer in the $^{19}\text{F}(d,p)^{20}\text{F}$ reaction induced by a polarized deuteron beam has been observed, and then the β -ray distribution from aligned ^{20}F was precisely measured.

The experimental setup is as shown in Fig. 1. ^{20}F ($I^\pi = 2^+$, $T_{1/2} = 11$ s) nuclei were produced in the reaction $^{19}\text{F}(d,p)^{20}\text{F}$. A 0.5-mm thick target of NaF, CaF_2 or MgF_2 single crystal, or a 0.1-mm thick target of MgF_2 , which was tilted 45° , was bombarded with a polarized deuteron beam of about 1.2 nA at 15 MeV or 6 MeV, extracted from the Tandem Accelerator in UTTAC. Typical beam polarization was 72%. The ^{20}F nuclei recoiled to various reaction angles were stopped inside the target. The target, also working as a recoil catcher, is placed in a strong magnetic field of about 2.5 kOe to maintain the polarization. Beta rays from the ^{20}F nuclei were detected by two sets of plastic scintillation counter telescopes placed above and below the target/catcher relative to the polarization. Typical β -ray counting rate was approximately 50 k counts/s. In order to reject unwanted background radiation, the deuteron

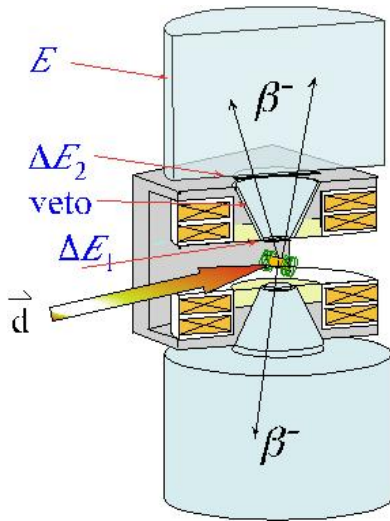


Fig.1. Experimental setup.

beam was chopped by a mechanical chopper, so that the beam was on for 11 s and was off for 22 s, and β rays were observed while the beam was off. Degree of polarization was detected by the β -ray asymmetry between the two counters, in terms of the β -ray angular distribution, $W(\theta) = 1 + (v/c)AP\cos\theta$, where, A is the asymmetry parameter which is predicted for ^{20}F to be $-1/3$, theoretically, P is the polarization and θ is the β -ray emission angle relative to the polarization. To cancel the geometrical asymmetry in these counters, beam polarization was flipped between up and down periodically. For the more reliable measurement, asymmetries were also measured flipping the nuclear polarization by means of the nuclear magnetic resonance (NMR) technique, to check the consistency. For the

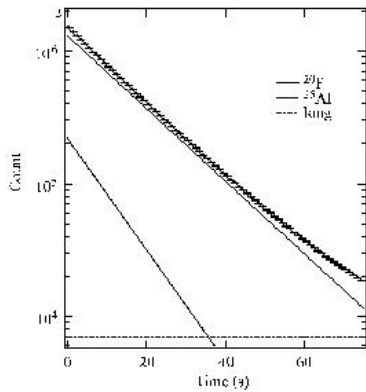


Fig. 2. Typical β -ray time spectrum.

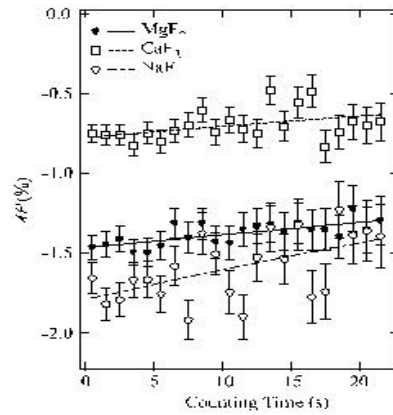


Fig. 3. Time dependence of the polarization.

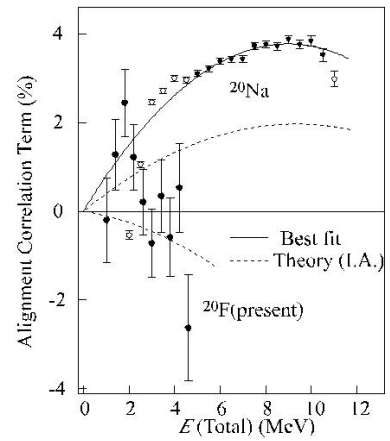


Fig. 4. Alignment correlation Term.

NMR, radio-frequency (rf) oscillating magnetic field H_1 was applied by a pair of coils set around the target/catcher. Adiabatic fast passage (AFP) method in NMR technique was used to invert the nuclear spin polarization.

Beta-ray time spectrum was observed as shown in Fig. 2. The main component was ^{20}F , while small component of ^{25}Al was produced from Mg in the case of MgF_2 target. The polarization of ^{20}F was observed by comparing the β -ray asymmetries, which is the counting rare ratio between the upper (0°) and the lower (180°) counters, for beam polarization up and down. As a result, polarization of 4 ~ 5% was observed at 15 MeV for NaF or MgF_2 targets, as shown in Fig. 3, where the asymmetry parameter was assumed to be $-1/3$. At 6 MeV, the polarization of about 6 % was also observed for MgF_2 . These results are consistent with the data for ^{20}F by J.W. Hugg[1] at Stanford Univ. From the fitting analysis to the time dependence of the polarization shown in Fig. 3, the relaxation times T_1 in NaF, CaF_2 and MgF_2 were deduced to be 90_{-22}^{+45} , 104_{-31}^{+76} , 173_{-54}^{+144} , respectively.

In the next step, the polarization of ^{20}F was converted to the alignment by means of the β -NMR technique, and the β -ray angular distribution was measured. The alignment correlation term was extracted as a function of β -ray energy from the energy spectra from both positively and negatively aligned ^{20}F nuclei. The obtained alignment correlation term for ^{20}F is shown in Fig. 4, together with the one for the mirror partner ^{20}Na previously measured [2] at TRIUMF using Laser optical pumping method. The difference between the alignment correlation terms for ^{20}F and ^{20}Na β decays is sensitive to the G-parity irregular induced tensor term in the weak nucleon currents, which induces nuclear β decay. The alignment correlation term for ^{20}F has been measured using recoil polarization. However, the obtained polarization of approximately 1.3 % was not large enough for the measurement.

References

- [1] T. Minamisono et al., Phys. Rev. Lett. **34** (1975) 1465; Phys. Lett. **61B** (1976) 155;
Phys. Rev. **C14** (1976) 376; Hyperfine Interactions **2** (1976) 315. and J.W. Hugg, PhD thesis, 1979.
[2] K. Minamisono et al., Nucl. Phys. **A746** (2004) 673c.

¹ Department of Physics, Osaka Univ., Toyonaka, Osaka 560-0043 Japan

² NSCL, Michigan State Univ., East Lansing, MI 48824-1321, USA

³ Fukui Univ. of Technology, Fukui 910-8505 Japan

2.5 Nucleosynthesis of the p-nuclei

T.Hayakawa¹, T.Shizuma¹, T.Komatsubara, K.Miyakawa

The astrophysical origin of the p-nuclei has been discussed for long years. The p-nuclei are rare isotopes (typically 0.1 ~ 1 %) and are located in the neutron-deficient side from the β -stability line. The nucleosynthesis by photodisintegration reactions in type II supernova (SN) explosions have been proposed (γ -process or p-process)[1, 2]. Analyzing the solar system abundance, we reported two universal scaling laws concerning the p- and s-nuclei with the same atomic number [3]. These scalings are an evidence of the γ -process origin of the p-nuclei [3]. However the scalings indicate that $^{92,94}\text{Mo}$ and $^{96,98}\text{Ru}$ isotopes have different origin. In addition standard SN model calculations cannot reproduce the relative abundances of these isotopes. The fact that they are located near the neutron magic number $N=50$ suggests that proton capture reactions may have an important role for the nucleosynthesis of them. Since proton-capture cross-sections for elements heavier than a Ce isotope have not been measured, we develop a measurement technique based on the activation method for the proton-capture cross-sections.

In order to measure a beam current with a high accuracy, we newly made a irradiation chamber. This chamber had a target folder and a Faraday cup with a diameter of 114 mm and a length of 300 mm. We set a beam slit of a diameter of 5 mm to constrain the beam optics. The natural Pd target was irradiated by the proton beam with 4.3 MeV energy, which was provided by the Tandem accelerator in the University of Tsukuba. The thickness of the target was 0.0125 mm. The target was moved to the front of the HPGe detector with a lead shield after the irradiation. The efficiency of the HPGe detector was calibrated by ^{152}Eu and ^{133}Ba standard sources. The energy resolution of the detector was approximately equal to 2.8 keV. We evaluated the proton capture cross-sections of the $^{102}\text{Pd}(p,\gamma)^{103}\text{Ag}$ reaction. Özkan et al. have been measured the proton-capture cross-sections of this reaction [4]. Our result cannot show a good agreement with this previous value. This may be originated from the instability of the beam current and the beam focus of a diameter of 6 mm at the target. We should thus improve the beam optics and the stability.

References

- [1] M. Arnould, *Astron. Astrophys.* **46**, 117 (1976).
- [2] S. E. Woosley and W.M. Howard, *Astrophys. J. Suppl.* **36**, 285 (1978).
- [3] T. Hayakawa et al., *Phys. Rev. Lett.* **93**, 161102 (2004).
- [4] N. Özkan et al., *Nucl. Phys. A* **710**, 469 (2002).

¹Japan Atomic Energy Research Institute, Kyoto, Kizu, Umemidai 8-1, 619-0215

3.

ATOMIC AND SOLID STATE PHYSICS,

AND

CLUSTER SCIENCE

3.1 Fragments of accelerated atomic cluster ions

K. Sasa, S. Ishii, K. Shima, S. Tomita and H. Kudo

The atomic cluster ion beams of B_n^+ , C_n^+ , Al_n^+ , Si_n^+ , Ni_n^+ and Cu_n^+ have been obtained with the MeV energy range from the 1MV Tandetron accelerator [1]. Negative cluster ions produced by the sputtering ion source were inflected 30° by an inflection magnet and accelerated by a positive voltage on the high voltage terminal. In the high voltage terminal, negative cluster ions should be stripped by SF_6 gas to positive ions and the latter are accelerated in the second section of the accelerator. We measured fragments of accelerated atomic cluster ions after passing through the stripping gas at the terminal. Accelerated atomic cluster ions and their fragments were selected by a magnetic analyzer and transported to the 11° beam course. The beam current of the atomic cluster ion beam was measured by a Faraday cup at the 11° beam course. Fig.1 shows fragments of accelerated C_8^- with the terminal voltage of 0.9 MV. Due to dissociation of C_8^- during the charge exchange in the stripping gas, there are positive C_1 - C_8 ions having different energies and charge states at the accelerator exit. The parameters of the beam transport were optimized for 1.9MeV C_8^+ beam, therefore the beam spectrum of C_8^+ beam have a sharp peak. It is confirmed that the intensity of the odd number fragmentary cluster ions (C_{2n+1}^+) is strong as compared with the even numbers (C_{2n}^+).

We found accelerated multi charged cluster ions to analyze fragments of atomic cluster ions. Fig.2 shows the beam spectrum of C_5^{2+} obtained through the fragment of C_6^- . If atomic cluster ions have the same charge to mass ratio, they follow the same trajectory through the magnetic analyzer. For example,

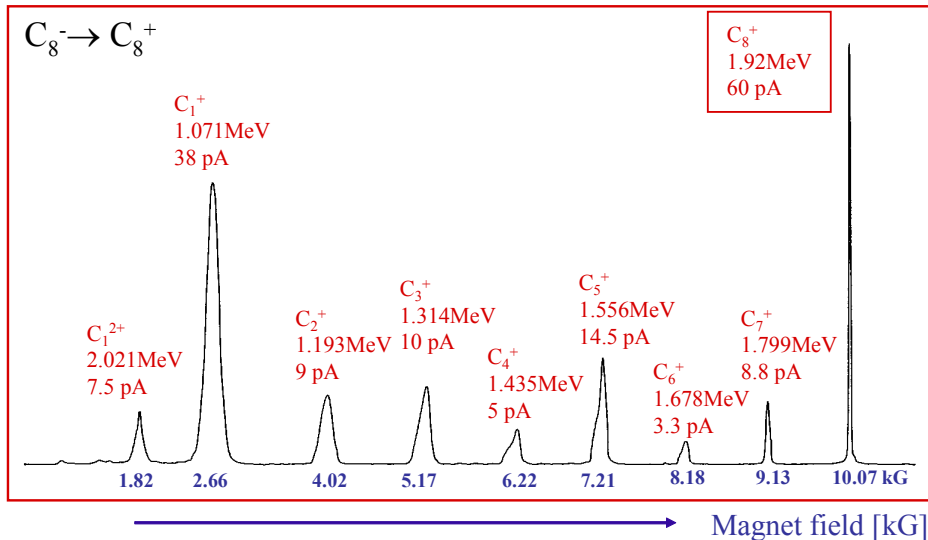


Fig.1. Fragments of accelerated C_8^- with the terminal voltage of 0.9 MV. The parameters of the beam transport were optimized for 1.9MeV C_8^+ beam.

C_6^{2+} and C_3^{1+} have the same magnetic rigidity for C_6^- injection, therefore these are not able to be distinguished. By reason of this, we are not able to get C_{2n}^{2+} beams by means of our experimental set-up. Table 1 shows the list of accelerated multi charged cluster ions obtained from the 1MV Tandatron accelerator at present.

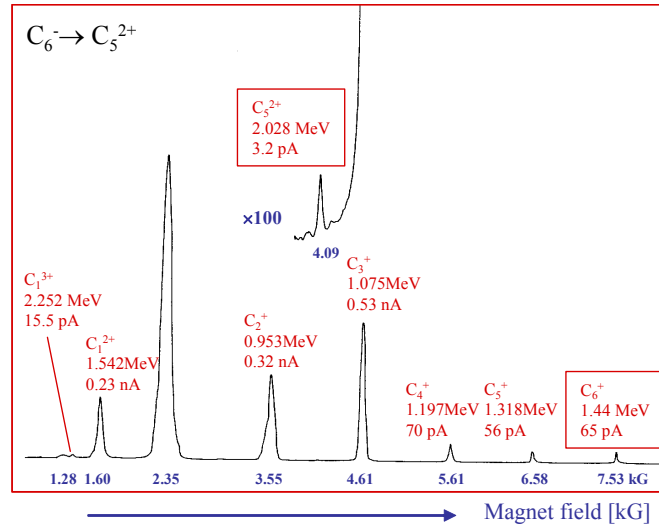


Fig.2. Fragments of accelerated C_6^- with the terminal voltage of 0.71MV. The parameters of the beam transport were optimized for C_5^{2+} beam.

Table 1 List of accelerated multi charged cluster ions obtained from the 1MV Tandatron accelerator.

Accelerated multi charged cluster ions	Beam energy [MeV]	Beam current [pA]	Injected cluster ion species	Injected beam current[nA]	Terminal voltage [MV]
C_3^{2+}	1.07	3.4	C_3^-	450	0.35
C_5^{2+}	2.03	3.2	C_6^-	400	0.71
C_7^{2+}	2.51	0.4	C_7^-	32	0.83
Al_2^{3+}	0.94	10	Al_2^-	1700	0.23
Al_3^{2+}	1.07	45	Al_3^-	330	0.35

References

- [1] K. Sasa et al., UTTAC72 (2004) 1.

3.2 Resonant coherent excitation of C^{5+} observed with backward electron spectroscopy

H. Wakamatsu, T. Shimada, R. Uchiyama, M. Furutani, J. Baba, S. Tomita, and H. Kudo

When an ion passes along an axial direction of a crystal, it experiences a periodic Coulomb field of frequency v/d , where v is the ion velocity and d is the atomic spacing. The ion can then be excited resonantly when the frequency matches the excitation energy of the bound electron I , i.e., $I = Nh\nu/d$, where h is the Planck constant and $N = 1, 2, 3, \dots$ [1]. This phenomenon, resonant coherent excitation (RCE), occurs also for planar channeling. RCE has so far been observed mainly by charge-state analysis of channeled ions passed through thin, self-supported crystals. RCE also affects the photon emission, or the convoy electron emission. Under RCE conditions, the loss electron yield might be increased by the easier ionization from an excited state than from the ground state. This is actually a two-step loss process in contrast to the normal (non-resonant) loss process [2]. From a viewpoint of ion-induced electron spectroscopy, it is of essential interest to investigate the influence of RCE on the production of loss electron yield from a bulk target since, unless it is negligibly small, it must be taken into account when crystalline targets are used.

The C^{5+} and C^{6+} beams in the energy range 2.8-3.2 MeV/u were obtained from the tandem accelerator at the University of Tsukuba, and were incident on a chemically cleaned Si(100) surface at room temperature under a pressure of 8×10^{-7} Pa. For Si<100>, the RCE condition for $N = 2$ (2nd harmonics) from the ground state to the first excited state ($n = 1$ to 2) of C^{5+} is satisfied at 3.01 MeV/u ($I = 367.2$ eV, $d = 5.43$ Å). The <100> perpendicular to the Si surface was chosen to observe RCE. The energy spectra of the ion-induced electrons were measured at 180° with respect to the beam direction over a solid angle of $\sim 2 \times 10^{-3}$ sr. The relative energy resolution ($\Delta E/E$) of the spectrometer was $\sim 5\%$, which is sufficient for the present analysis of the loss electron yield.

Figure 1 shows energy spectra of the emitted electrons induced by 3.01 and 3.11 MeV/u C^{5+} and C^{6+} under Si<100> channeling conditions. E_L indicates the loss-peak energy which is the kinetic energy of the electron moving at the same velocity with the ion. The ionized electrons from the ion contribute to the backward electron yield at energies lower than $\sim E_L$. It is recognizable that for C^{5+} yield below E_L is higher than for C^{6+} , irrespective of the two ion energies. This is due to the loss electrons anticipated not for C^{6+} , but for C^{5+} . Increase of the loss electron yield can be clearly seen for the 3.01 MeV/u ions, compared with that for the 3.11 MeV/u ions. For a better statistics, we have integrated the electron yield in the three fixed ranges, i.e., 0.9-1.1, 1.1-1.3, and 1.3-1.5 keV, and the normalized loss yield L has been defined by $L = (Y_{\text{int}}^{5+} - Y_{\text{int}}^{6+}) / Y_{\text{int}}^{6+}$, where $Y_{\text{int}}^{5,6+}$ are the integrated yields. L is actually the ratio of the loss yield to the binary-encounter yield.

Figure 2 shows ion-energy dependence of L for the electron energy ranges. At the calculated resonance energy of 3.01 MeV/u, the enhanced value of L can be clearly recognized for the 0.9-1.1 and 1.1-1.3 keV energy ranges, which is an experimental evidence for the RCE-assisted loss electron process.

Since the most probable energy of the produced loss electrons is the loss-peak energy E_L , the typical

loss yield observed at energy of ε should have an escape length of $(E_L - \varepsilon)/S_e$, where S_e is the electron stopping power of Si. Using the value of $S_e = 1.6 \text{ eV/\AA}$ for 1.6 keV electrons, we can obtain the mean escape lengths for the three ranges. They are 350 \AA , 240 \AA and 130 \AA for the 0.9-1.1, 1.1-1.3, and 1.3-1.5 keV ranges, respectively. In Fig. 2 it is obvious that the RCE-peak is more pronounced for the lower energy ranges. The deeper the loss electrons are generated from the Si surface, the higher RCE-peak is formed. Therefore, RCE-assisted electron loss process can be related to the number of collisions with the target atoms.

The width of the present RCE-peak is much sharper than that observed with charge state measurements by Moak et al. [3]. One of the reasons for the sharper peak should stem from small projectile energy loss. In the present case, the RCE-assisted loss yield within the surface layer of $\sim 350 \text{ \AA}$ thickness can be reflected in the loss electron yield. Furthermore, the energy loss of 3 MeV/u C passing through $\sim 350 \text{ \AA}$ is $\sim 21 \text{ keV}$, i.e., 0.0018 MeV/u, which is estimated with the assumed channeling stopping power of 60 eV/ \AA . The ratio of the ion energy loss to the ion energy at the RCE condition is $0.0018/3.01 = 0.059\%$. Therefore, the effect of projectile energy loss is too small to influence the observed RCE curve shown in Fig. 2. The present study has provided a unique observation technique of RCE. Further experiments are now under way to investigate the initial stage of RCE.

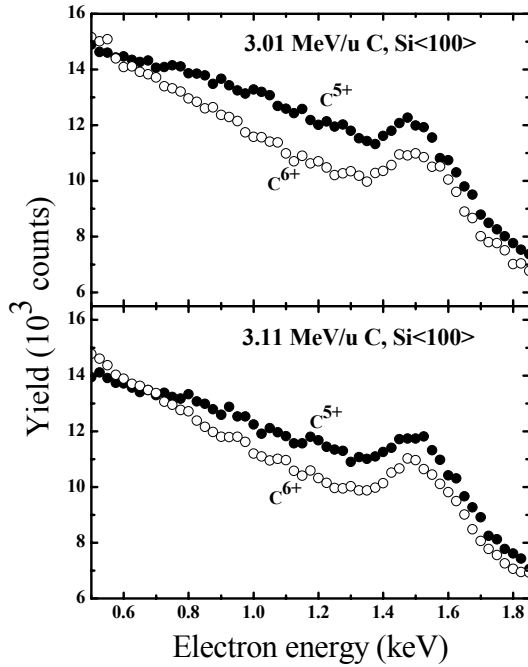


Fig.1. Energy spectra of electrons emitted from Si bombarded by 3.01 and 3.11 MeV/u C^{5+} and C^{6+} under $\langle 100 \rangle$ axial incidence conditions.

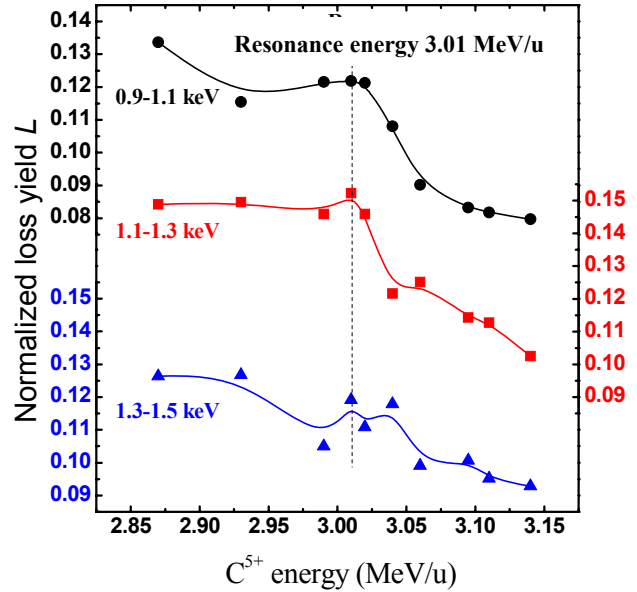


Fig.2. Dependence of the normalized loss yield L on the C^{5+} incidence energy, shown for the three integrated electron-energy ranges.

References

- [1] V. V. Okorokov, Zh. Ehksp. Theor. Fiz. Pis. Red. 2 (1965) 175 [JETP Lett. 2 (1965) 111].
- [2] N. Stolterfoht, R. D. DuBois, R. D. Rivarola, Electron Emission in Heavy Ion-Atom Collisions (Springer, Berlin, Heidelberg, 1997), Sect. 6.4.
- [3] C.D.Moak et al, Nucl. Instr. and Meth. 194 (1982) 327.

3.3 Yield of secondary electrons induced by fast cluster ions

R. Uchiyama, T. Shimada, M. Furutani, H. Wakamatsu, H. Kudo, S. Tomita, K. Shima, K. Sasa, S. Ishii

An accelerated cluster ion induces correlated atomic impacts when it is incident on a solid target. This causes radiation damages different from the sum of those induced by impact of individual constituent atoms. The effects are called “vicinage effect” and actually observed for fast cluster ions in the MeV/atom velocity range. These radiation effects by fast atom clusters have been summarized in recent reviews [1, 2].

We have investigated on the vicinage effects by measuring energy spectra of secondary electrons under irradiation of fast cluster ions. The beams of C_n^+ ($n = 1-8$), Al_n^+ ($n = 1-5$) were obtained from the 1MV Tandetron accelerator at UTTAC. They were incident on the samples of highly oriented pyrolytic graphite (HOPG) with a cleaved (0001) surface, chemically cleaned Si, and sputter-cleaned polycrystalline Au. The surface of the Si sample was cut $\sim 2.5^\circ$ off from the (100) surface so that the ions suffer no channeling effect under incidence in the normal direction of the surface. The emitted electrons from the bombarded targets were measured at 180° with respect to beam direction, using a 45° parallel-plate electrostatic spectrometer of the double deflection type. The solid targets were negatively biased at $V_1 = 50$ V to separate the background electron near zero energy from the spectra, and to improve the transmission efficiency of low-energy electrons through the spectrometer. The electrons were detected by channeltron detector that the acceleration potential of +200V was applied to the entrance electrode to enhance the detection efficiency. In the present pre-acceleration method noted above, the relative energy resolution of the spectrometer is given by $\Delta E/(E+eV_1) = 3\%$.

Figure1 shows energy spectra of electrons emitted from HOPG bombarded by C_n^+ ($n = 1,8$) with velocity of 0.24MeV/atom. It is clearly seen that the electron yield per atom is reduced for the cluster incidence compared to the single ion in the wide range of electron energy. The reduction effect strong for the low energy electrons and becomes weaker with increasing electron energy. This is reasonable because the high energy electrons are mainly generated by close collisions in which the influence from neighbor atoms become smaller.

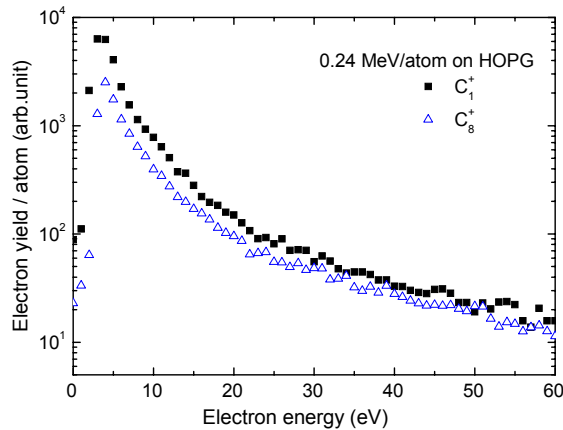


Fig.1: Energy spectra of electrons emitted from HOPG bombarded by 0.24MeV/atom C_n^+ ($n = 1,8$). The yields are normalized to the same number of the incident C atoms.

Figure 2 shows the integrated yields Y_n per C_n cluster ion. The yields are normalized to the case of single atom incidence. Interestingly the electron yields increase linearly with the number of constituent. This means that the contribution from one additional constituent is independent on the size of cluster ions. The same behaviour can be seen for various targets even though the absolute yields should be different according to the stopping power of each target.

Figure 3 shows the integrated yield Y_n per C_n cluster for Si, together with those for Al_n for comparison. Clearly, the vicinage effect is more pronounced for C_n than for Al_n . Since these ions lie in a similar velocity range (0.75MeV/atom C_n and 1.76MeV/atom Al_n are of equal velocity), the same ionization mechanism, i.e., mainly the binary-encounter processes, is expected. The pronounced effects are probably due to the shorter interatomic spacing of 1.3Å than 2.6Å of Al_n .

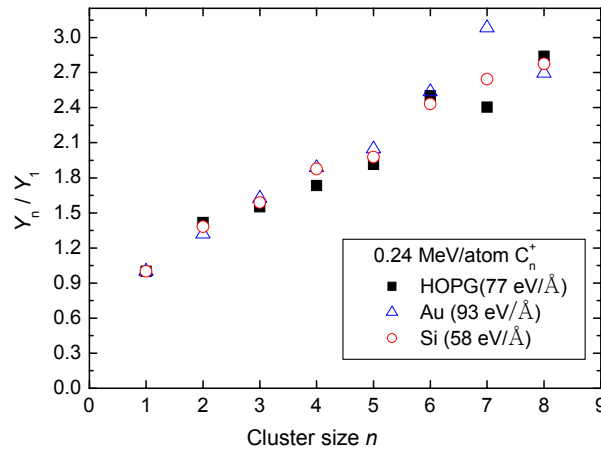


Fig.2: Integrated electron yield Y_n per 0.24MeV/atom C_n cluster for various target (HOPG, Au, and Si), which were normalized to the case of $n = 1$.

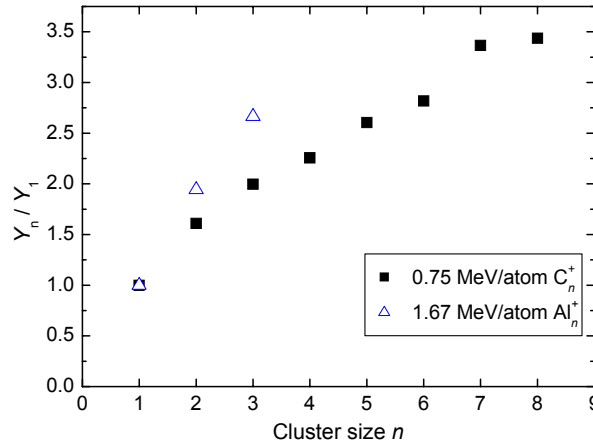


Fig.3: Integrated electron yield Y_n per 0.75MeV/atom C_n cluster for Si, together with the case of 1.67MeV/atom Al_n cluster, which were normalized to the case of $n = 1$.

References

- [1] D. Jacquet, Y. Le Beyec, Nucl. Instrum. Methods B 193 (2002) 227.
- [2] E. Parilis, Nucl. Instrum. Methods B 193 (2002) 240.

3.4 Abundance spectra of neutral metal clusters produced by magnetron-sputter-type gas aggregation cluster source

T. Suzuki, H. Mishiba, H. Sasaki¹, and I. Arai

We have developed a magnetron-sputter-type gas aggregation cluster source. It is about a half-sized version of our previously developed one. So far, we have observed the metal cluster cations with a size of up to 50 and more with use of the previously developed one. Unfortunately, neutral clusters were not measured at that time because of experimental limitation. We have recently realized that the observation of neutral clusters is important for enough understanding of the cluster formation mechanism in the gas aggregation source. We are now carrying out an experiment to measure abundance spectra of neutral metal clusters produced by the newly-developed gas aggregation source. Al and Cu are used for sputtering target. The neutral cluster beam coming from the gas aggregation source is irradiated and ionized by the laser Nd:YAG-Laser of 266nm in wave length. For the measurement, we use a Wiley-McLaren-type time-of-flight mass analyzer. The cluster cation is accelerated by an extraction field of 3kV and extracted into a field-free drift region. At the end of drift region, it is detected by a microchannel plate detector. The time of flight in drift region is analyzed with use of a multi-stop time-to-digital converter combined with a personal computer. Finally, a spectrum of the mass to charge ratio for cluster cation is obtained. In the present test run, we have confirmed Al clusters of the size up to 4 (see Fig. 1) and Cu clusters of the size up to 17(see Fig.2).

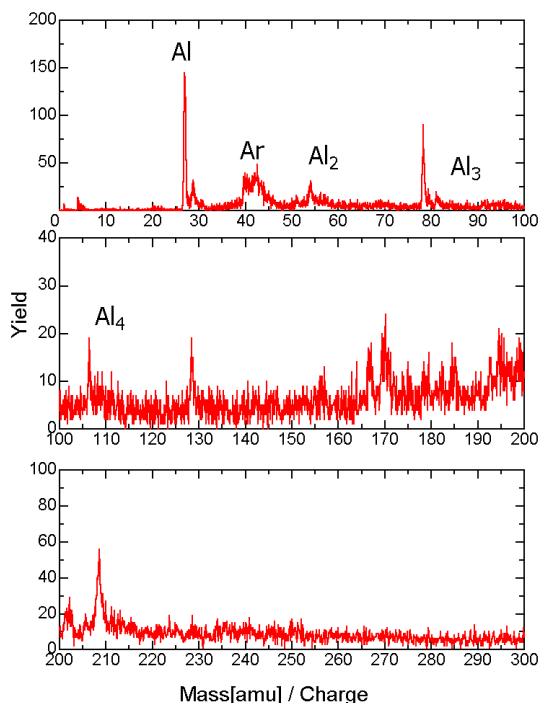


Figure 1. Abundance Spectrum of Al Clusters

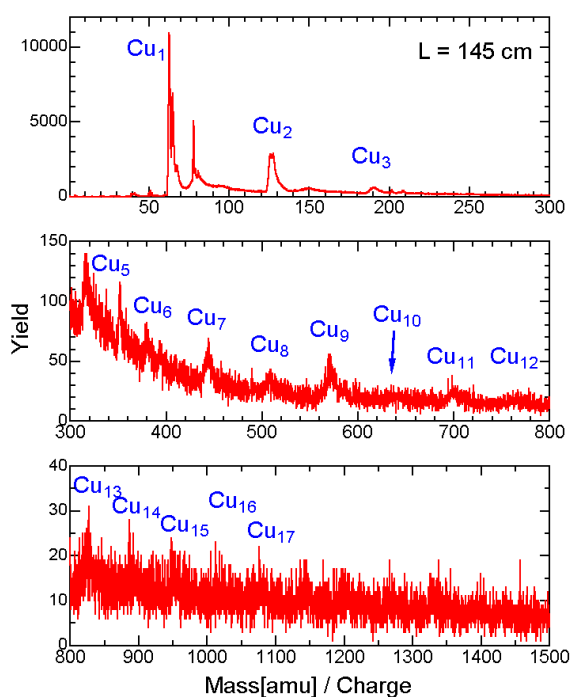


Figure 2. Abundance Spectrum of Cu Clusters

¹ EENA Co. Ltd., Tsukuba, Ibaraki 305-0035, Japan.

3.5 DSMC simulation of magnetron-sputter-type gas aggregation cluster source

S. Hamajima and I. Arai

A new type of magnetron-sputter-type gas aggregation cluster source is now under development. The apparatus is functionally divided into two parts, i.e., a magnetron sputtering part and a gas aggregation cell. In the magnetron sputtering part, ionized Ar atoms sputter the sample surface mounted on the magnetron cathode producing a number of monomer atoms, which are mixed with a carrier gas and transferred to the gas aggregation cell. The carrier gas is a mixture of Ar and He. The gas aggregation cell is cooled by liquid nitrogen and the monomer atoms aggregate together into clusters there. Furthermore, some clusters are ionized by the photon emitted by excited He atoms in the carrier gas. The cluster growth in the aggregation cell is thought to be controlled by the parameters such as (1) the cluster growth length and (2) the temperature, pressure and flow of carrier gas. The performance of cluster source is expected to be greatly improved by optimizing the above parameters. Enough understanding should be accomplished with accounting for real gas flow in the gas aggregation cell. To simulate a real gas flow as precisely as possible, we adopt a direct simulation Monte Carlo (DSMC) method. In present, we have obtained the following characteristic features; (1) the flow of carrier gas in the aggregation cell is very much dependent on the size of orifice at the exit port, (2) the average residual time of monomer atoms in the aggregation cell is essential for the cluster growth rate, and (3) the average residual time is determined by the control parameters such as the cluster growth length, the temperature, pressure and flow of carrier gas, and so on. Figure 1(a) and Figure 1(b) show the mean arrival time of monomer atoms at the certain longitudinal position in the aggregation cell and its variance, respectively. These figures suggest that the sputtered monomer atoms are thermalized at the cluster growth length of 4cm, moving along with the carrier gas and gradually diffusing.

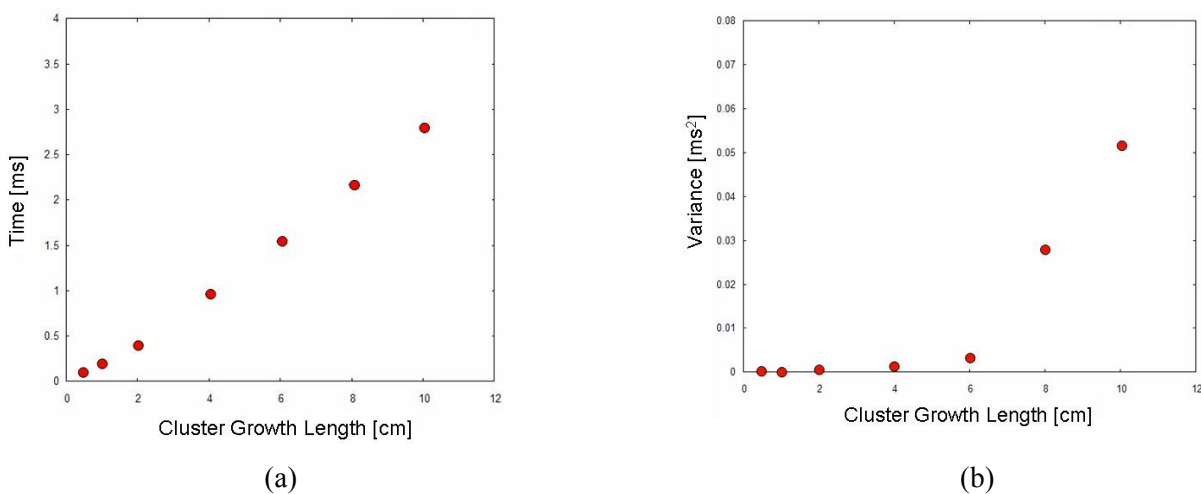


Figure 1. Mean arrival time of monomer atoms at the certain longitudinal position in aggregation cell (“Cluster Growth Length”) and its variance; the orifice radius is 1.5mm.

3.6 Reactions between Ni_{13} cluster and oxygen atoms.

M. Kubo, I. Arai, and K. Sugawara

In a recent experimental study, $Ni_{13}O_8$ cluster has been found to be a terminal product of the oxidation reaction of Ni_{13} cluster. To understand the situation in terms of the inter-atomic interactions, we have carried out a molecular-dynamics simulation of the reaction between Ni_{13} and O atoms. In the simulation, an oxygen atom collides with the cluster $Ni_{13}O_n$ sequentially to produce $Ni_{13}O_{n+1}$ at 150K and the energy profile of oxygen atoms is examined as a measure of stability of the resulting hybrid clusters. In addition, the simulation at 170K has been done for comparison. For numerical integration, Verlet's finite difference method is used. The time step is 2fs and the total time is 4ns.

The potential energy of n atoms transition metal cluster is given by the Gupta potential

$$V(r_{ij}) = \sum \left[\epsilon_0 \sum_{i \neq j} e^{-p \left(\frac{r_{ij}}{r_{0n}} - 1 \right)} - \sqrt{\xi^2 \sum_{i \neq j} e^{-2q \left(\frac{r_{ij}}{r_{0n}} - 1 \right)}} \right] \quad (1)$$

where p, q, ϵ_0 , ξ , and r_{0n} are material-dependent parameters, and r_{ij} is inter-atomic distance. For nickel clusters, $r_{0n}=2.5$, $p=16.999$, $q=1.189$, $\epsilon_0=0.0376$, $\xi=1.070$.

The potential energy of other interactions is given by the Lennard-Jones potential

$$V = 4\epsilon \left[\left(\frac{\sigma}{r} \right)^{12} - \left(\frac{\sigma}{r} \right)^6 \right] \quad (2)$$

where ϵ and σ are material-dependent parameters. For oxygen-oxygen interaction, $\epsilon=5.63 \times 10^{-3}$ eV, $\sigma=3.0$ Å. For nickel-nickel interaction, we refer to the energy minimum and the inter-atomic distance of Gupta potential for nickel dimer. The parameters of Lennard-Jones potential are determined as $\epsilon=0.95$ eV, $\sigma=2.25$ Å. For nickel-oxygen interaction, we estimate two parameters of Lennard-Jones potential using the Lorentz-Berthelot combining rules as $\epsilon=0.073$ eV and $\sigma=2.725$ Å.

Fig.1 shows the resulting $Ni_{13}O_8$ in the simulation at 150K. All the oxygen atoms are adsorbed on the surface of Ni_{13} cluster core. It is found that more than 10 oxygen atoms can be adsorbed in this way. Fig.2 shows the resulting $Ni_{13}O_8$ in the simulation at 170K. All the oxygen atoms are adsorbed on the surface of Ni_{13} cluster core in a similar manner. However, more than 8 oxygen atoms can not be adsorbed and $Ni_{13}O_8$ becomes a terminal product. Fig.3 and Fig.4 show the energy profile, i.e., the population of binding energy sampled at each time step, of the oxygen atom involved in $Ni_{13}O_8$ at 150K and at 170K, respectively. At 150K, the oxygen atom transits among the states with binding energy less than -0.5×10^{-2} eV. At 170K, the maximum binding energy begins to reach near 0eV just after adsorption of 8 oxygen atoms. The energy states around 0eV are considered to give a possible pathway to unbound state. Therefore, the oxygen atom can not be adsorbed on the surface of $Ni_{13}O_8$ anymore. As a result, $Ni_{13}O_8$ becomes a terminal product.

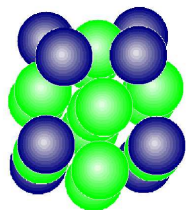


Fig. 1. $Ni_{13}O_8$ cluster at 150K(Oxygen:blue, Nickel:green)

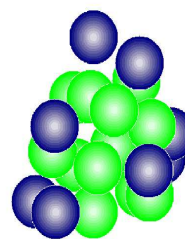


Fig. 2. $Ni_{13}O_8$ cluster at 170K(Oxygen:blue, Nickel:green)

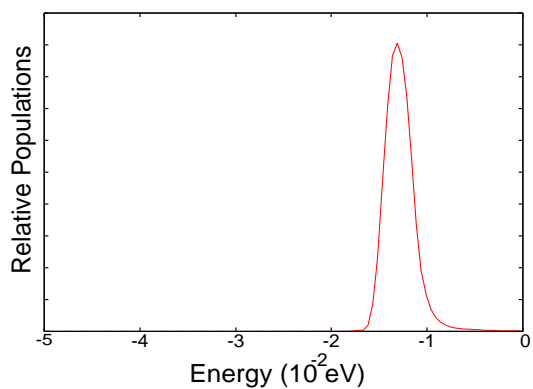


Fig. 3. Energy profile of the oxygen atom involved in $Ni_{13}O_8$ cluster at 150K.

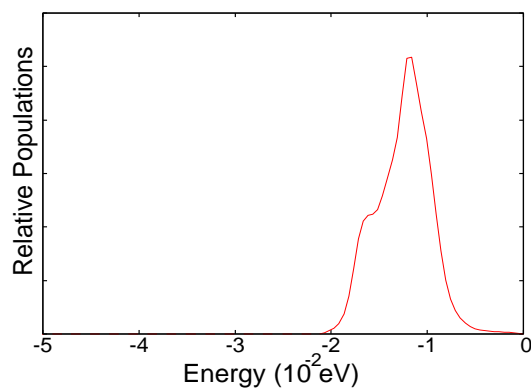


Fig. 4. Energy profile of the oxygen atom involved in $Ni_{13}O_8$ cluster at 170K.

3.7 Pulsed extraction of cluster ions from magnetron sputtering gas aggregation cluster source

H. Mishiba, T. Suzuki, H. Sasaki, and I. Arai

The purpose of this study is a development of the apparatus for pulsed extraction of cluster ions, which is joined to a magnetron sputtering gas aggregation cluster source. The magnetron sputtering gas aggregation cluster source can provide clusters of broad mass distribution, so that it is used extensively not only for academic researches but also industrial ones.[1]

Fig.1 shows a schematic view of the apparatus. The magnetron sputtering gas aggregation cluster source consists of a magnetron sputtering head and a gas aggregation cell. Ionized Ar atoms sputter metal sample on a cathode of magnetron sputtering head. Monomer atoms are released from the sample surface and carried into the aggregation cell by carrier gas, i.e., a mixture of Ar and He. The aggregation cell is cooled down by liquid nitrogen. While passing through it, the monomer atoms aggregate together into clusters. In addition, photons coming from excited He atoms ionize some fraction of the clusters. The pulsed accelerator is put just downstream of the aggregation cell. It consists of seven electrodes. One out of them is operated in a pulsed mode, where the acceleration pulse is applied in addition to a constant bias voltage in a very short time. The others are fixed to constant bias voltages. When the acceleration pulse is not applied, the constant bias voltage blocks the cluster ions. The acceleration pulse is 1KV in amplitude, 2μ s in width, and 1ms in inter-pulse duration. Its timing is used as a start signal of the time-to-digital converter(TDC). Two steerers are introduced to displace the trajectories of cluster ions. The displacement of a few cm is necessary to prevent the light from the magnetron sputtering head to enter the detector. We use an Even-cup-type detector, where the secondary electrons are produced by the collision of cluster on the metal surface and multiplied with use of MCP. The preparation of apparatus has been finished. The experimental check is now under progress.

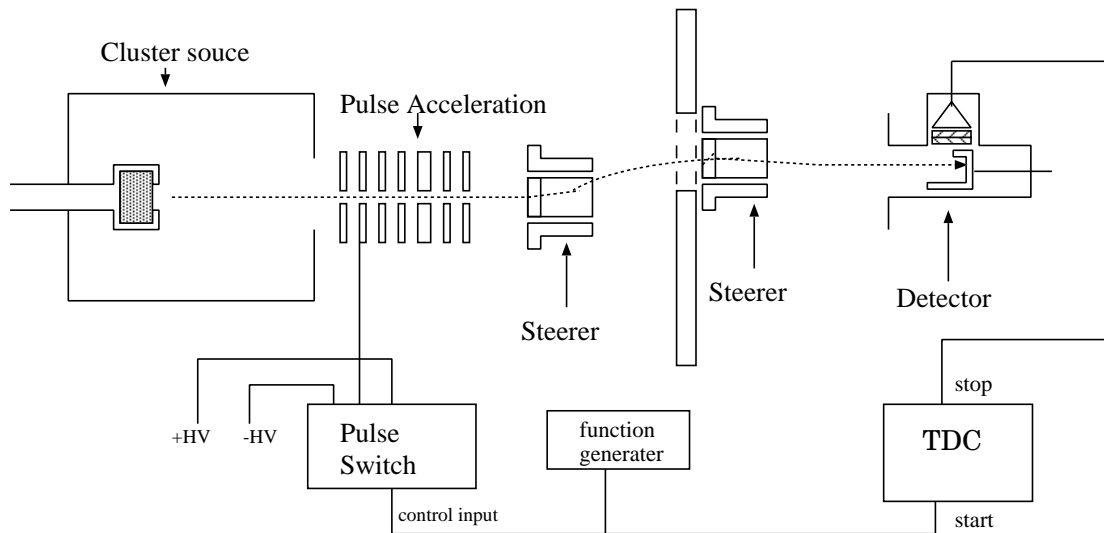


Fig. 1. Schematic view of apparatus

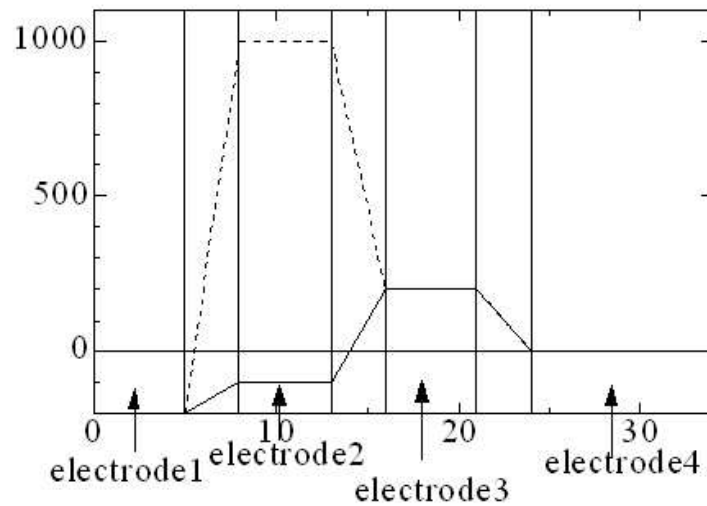


Fig. 2. Bias condition for pulsed acceleration

References

- [1] C.Xirouchaki and R.E. Palmer., *Phil Trans.*,**362**, 1814(2003)

3.8 Molecular dynamics calculations on hybrid clusters composed of Au atoms and Lennard-Jones atoms

A. Kondo, M. Kubo and I. Arai

We have carried out molecular dynamics(MD) calculations on reaction between an Au atom cluster and a Lennard-Jones atom cluster under changing the potential depth ϵ_{LJ} and the temperature T . We have examined the morphology of resulting hybrid cluster. Because the effective potential is predetermined by a material itself, this trial is expected to give some suggestion on how to control cluster structure by a combination of materials. As for effective potentials, we use a Gupta potential for the interaction among Au atoms[1] and a Lennard-Jones potential for the binary interaction between LJ atoms. A Lennard-Jones potential is also used for the binary interaction between an Au atom and an LJ atom and the Lorentz-Berthelot mixing rule is applied to estimate its potential depth and bond length. MD calculations are made as follows. At first, an Au atom cluster and an LJ atom cluster are brought up in separate runs, respectively. Then, both clusters are set close to each other at constant distance and the generation of a hybrid cluster is carried out. Since the Au atom cluster is expected to take a structure following to the face-centered cubic lattice, we choose Au_6 and Au_{13} clusters as smaller-sized clusters with good symmetry,. As for the LJ atom cluster, we use LJ_8 cluster. In the MD calculations, we use a Verlet method and chase the position and speed of each atom. Time step is 0.25fs and we calculate up to 1ps. When we change the potential depth ϵ_{LJ} over the range between 0.0032eV and 32eV, it is found that the structure of hybrid cluster is classified into the following three categories; (1)Low ϵ_{LJ} : the LJ atoms adhere to the surface of Au cluster.(Core-shell; see Fig. 1a), (2)Medium ϵ_{LJ} :the LJ atoms are mixed with the Au atoms.(Mixed; see Fig. 1b), and (3)High ϵ_{LJ} :Both clusters are separated in groups and deformed considerably but in contact with each other.(Separated; see Fig. 1c). In order to examine a possible temperature effect, MD calculations are carried out at the different temperatures $T=100K$, $300K$ and $500K$. Only when ϵ_{LJ} is small, the temperature effect is observed slightly.

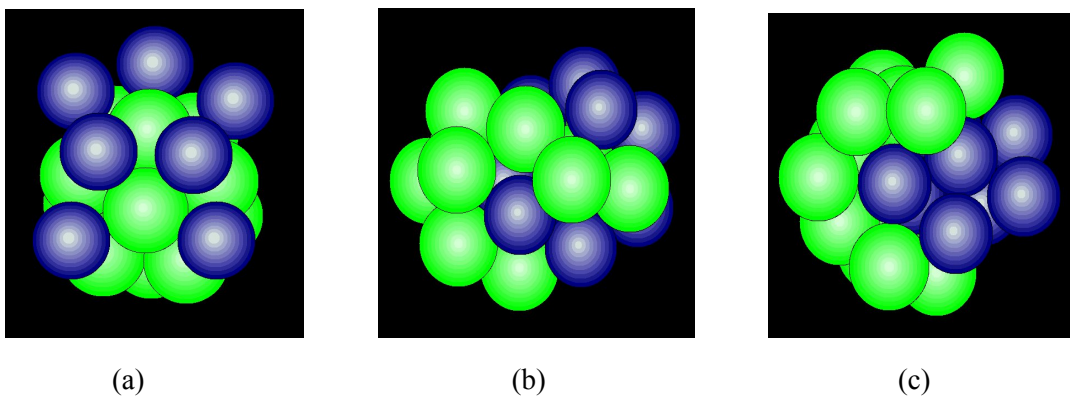


Figure1. Morphology of $Au_{13}LJ_8$ hybrid cluster at $T=100[K]$; (a) $\epsilon_{LJ}=0.0032eV$ (Core-shell), (b) $\epsilon_{LJ}=0.16eV$ (Mixed), and (c) $\epsilon_{LJ}=1.6eV$ (Separated) (Au atom: green; LJ atom: blue.)

References

[1] F. Cleri and V.Rosato, Phys. Rev. B, 48, 22(1993)

3.9 The science of 3d transition-metal oxide system (2004–2005)

M. Onoda, J. Hasegawa, T. Ikeda, T. Isobe, K. Takao, A. Sasaki, Y. Shinmura and A. Yamada

The structural and electronic properties of 3d transition-metal oxides and bronzes have been explored by means of x-ray four-circle diffraction and through measurements of magnetic resonance (NMR and EPR), magnetization, and electronic transport, in order to extract characteristic properties in the correlated electron system, electron-phonon-coupling system, quantum spin-fluctuation system, and novel materials. At the Tandem Accelerator Center, Varian continuous-wave and Bruker pulse NMR spectrometers have been used.

In 2004–2005, the following investigations were mainly performed and a part of them have been published elsewhere [1, 2]: (1) **quantum spin-fluctuation system** — *geometrical frustrations in $Cd_xZn_{1-x}V_2O_4$ and spin-gap states in δ - $M_xV_2O_5$ ($M = Ag, Tl, Na, K$ and Sr)*; (2) **correlated-electron and electron-phonon-coupling systems** — *metal-insulator transitions in V_6O_{13} and $Cu_xV_4O_{11}$* ; (3) **a new type of superconductors** — *superconducting properties of $Na_xCoO_2 \cdot yH_2O$, and geometrical frustrations and electronic properties of M_xVO_2 and M_xCoO_2 with $M = Li$ and Na* ; (4) **composite crystal system** — *superspace group approach to $Cu_xV_4O_{11}$* ; (5) **secondary ion battery system** — *Li insertion effects in $M_{1+x}V_3O_8$ ($M = Li, Na$ and Ag), $Ag_2V_4O_{11}$, $Cu_xV_4O_{11}$ and V_6O_{13}* . This report describes briefly recent progress for the secondary ion battery system.

Secondary ion battery system

$Li_{1+x}V_3O_8$ and $Li_xV_6O_{13}$ are typical insertion electrode systems for vanadium oxides. The former can accommodate around three or four additional Li ions per formula unit of LiV_3O_8 and the latter system eight ions per V_6O_{13} . These lithiations may supply new kind of compound series for the investigation on quantum-spin fluctuation and correlated electron systems. In order to construct this situation and to improve battery performances, it is important to study the basic properties as a function of the Li concentration, although the crystal structures for this system are rather complicated as compared with those for the well known insertion electrode systems.

The cw-NMR results for the linewidths of 7Li nuclei in $Li_{1+x}V_3O_8$ presented in a report in 2003–2004 are considered in detail. The main spectra for polycrystalline specimens with $x = 0, 0.25, 2.9$ and 4.6 are close to single Gaussian for all of the compositions. Since for $x \neq 0$, the Li ions have surely several independent sites, this result suggests that the several resonance lines are superimposed and/or the *localized* motional process is significant. The compositions with $x = 0$ and 0.25 correspond to $\gamma 1$ -phase ($0 \leq x < 1.5$) having the Li_2O_4 tetrahedra and that with $x = 4.6$ is $\gamma 2$ -phase ($x > 3.5$), in which all of cations are surrounded octahedrally. The linewidths for the $\gamma 2$ -phase are much larger than those for the $\gamma 1$ -phase. For both of the phases, the linewidths above room temperature decrease rapidly with increasing temperature, which indicates that the *long-range* motion of Li ions becomes significant, although the lineshape still remains like a Gaussian for the temperature region measured. Below room temperature, the linewidths with $x = 0$ are constant down to about 10 K, below which they exhibit a slight upturn. The results for $x = 0.25$ are almost similar to those for $x = 0$, but the former data have a slight peak at about 220 K. The linewidths with $x = 4.6$ are nearly temperature-independent from room temperature to about 100 K, below which they increase significantly with decreasing temperature. For $x = 2.9$ with the presence ratio of the $\gamma 1$ -phase $r \approx 0.5$, the resonance lines ascribed to the $\gamma 1$ - and $\gamma 2$ -phases should appear. However, the data are very similar to those for $x = 4.6$, which suggests that the Li signals for the $\gamma 1$ -phase is masked with those for the $\gamma 2$ -phase and/or the local environment around Li ions for the maximum concentration in the $\gamma 1$ -phase is close to that for the $\gamma 2$ -phase.

Table 1: Results of the analysis for the narrowing of Li NMR linewidth in $\text{Li}_{1+x}\text{V}_3\text{O}_8$.

x	Low temperatures			High temperatures	
	B (mT)	Δ (K)	W_0 (mT)	B (μT)	Δ (10^3 K)
0.0	0.363(2)	9(1)	0.51(2)	0.03(7)	3.7(7)
0.25	0.364(8)	5(4)	0.62(19)	0.08(16)	3.1(6)
2.9	0.57(10)	31(18)	0.95(6)	0.3(3)	2.9(3)
4.6	0.59(2)	31(5)	0.90(1)	0.2(2)	3.0(4)

The NMR linewidths in paramagnetic materials are generally caused by several interactions between the investigated nucleus and its surroundings. The second moments from the internuclear dipolar interaction and from the magnetic field for the powder grains give significant effects for the linewidths. First, the present data are analyzed with the assumption that the line narrowing occurs in two stages corresponding to the temperature regions above and below 100 K. Using the formalism of $W = 1/[(1/B - 1/W_0)\exp(-\Delta/T) + 1/W_0]$, where B is a temperature-independent linewidth, W_0 is the rigid-lattice linewidth and Δ is an activation energy, the results are obtained as listed in table 1. Here W_0 for the high-temperature side above 100 K is assumed to agree with B at low temperatures in order to reduce the number of parameters. At high temperatures, all of the compositions have $\Delta \approx 3 \times 10^3$ K, which may be responsible for the long-range motion of Li ions. At low temperatures for the γ_1 -phase, the Δ values are smaller than 10 K and the W_0 ones are significantly larger than the dipolar widths. They indicate the narrowing model in two stages to be inadequate and another contribution from the magnetic field for powder grains should be considered. This contribution is given by $2.3 \times 10^{-3}(\chi H_0)^2$, where χ is the magnetic susceptibility and H_0 is the resonance field, on the assumption of cubic close packing of spherical particles. Since the upturn behaviour at low temperatures is explained successfully, the linewidths below room temperature for the γ_1 -phase are basically regarded as the dipolar widths for the rigid lattice. On the other hand, the low-temperature behaviour for the γ_2 -phase seems to provide the Δ values reasonable for the narrowing model in two stages. For $x = 2.9$ and 4.6, the linewidths at the lowest temperature agree roughly with the dipolar widths considering that the numbers of unpaired electrons may range from 2 to 3 on the basis of the susceptibility results; that is, the Li ions are ordered at the lowest temperature. The narrowing behaviour at the low-temperature side seems to be correlated with the susceptibility anomalies. The order-disorder effect of Li ions may cause a slight change of superexchange coupling.

The correlation times for the long-range motion of Li ions for $x = 0$ and 0.25 estimated by $\tau_m \simeq (4\ln 2/\gamma_{\text{Li}}\pi W)\tan[(\pi/2)(W/W_0)]$, where γ_{Li} is the gyromagnetic ratio of ^7Li and W_0 is equal to B at low temperatures, are $\tau_m \simeq 0.12$ and 0.071 ms at 400 K, respectively. The corresponding diffusion coefficients are calculated as $D \simeq 5.6 \times 10^{-12}$ and 9.2×10^{-12} $\text{cm}^2 \text{s}^{-1}$ from the relation $D = l^2/n\tau_m$, where the hopping distance l and the number of near neighbouring sites n are taken as 3.6 Å and 2, respectively. These values are one order of magnitude smaller than those obtained from galvanostatic intermittent titration and pulse polarization methods, although the activation energies are similar to each other.

References

- [1] M. Onoda, T. Ohki and Y. Uchida: J. Phys.: Condens. Matter **16** (2004) 7863–7871.
- [2] M. Onoda: J. Phys.: Condens. Matter **16** (2004) 8957–8969.

3.10 RBS characterization of various thin films

H. Yanagihara, T. Onuma, T. Suemasu, T. Makimura, S. Chichibu, K. Akimoto and H. Kudo

Rutherford backscattering spectrometry (RBS) is a conventional and powerful method to characterize thin film structures. An RBS spectrum contains the depth profile of chemical composition and the thickness of the films. We can readily extract those quantitative information from the spectrum by using a commercial simulation program based on simple model fits. Since each measurement takes only a few minutes, the beam time were usually shared by a couple of groups. In the fiscal year 2004, we performed the RBS experiments for various samples; metals, oxides, nitrides, silicides, and nano-particle prepared by many different kinds of techniques.

An experimental setups are as follows. 1.5 MeV $^4\text{He}^+$ ions accelerated by the Tandetron accelerator at UTTAC were used for RBS experiments. The D-course is exclusively used to this experiment and the geometry of the incident angle(α), exit angle(β) and scattering angle(θ) are 30, 0 and 150 degrees, respectively. We used a solid-state detector placed at 70 mm from the sample surface. Most of RBS data were analyzed by a commercial simulation program (SIMNRA) which works on Windows based PC. Since this program has functions of both the RBS data fitting and the spectrum simulation with graphical interface, we can easily estimate the depth profile of chemical composition and the film thickness. As an example, typical samples measured the last fiscal year are shown in the following table.

materials	preparation methods	the number of samples	user group	reference
SiO_x	laser ablation	10	Murakami and Makimura	[1]
SiO_x+Er	laser ablation	10	Murakami and Makimura	[1]
InGaN	MVPE	1	Chichibu	[2]
(Ga, <i>R</i>)N	MBE	14	Akimoto and Sakurai	
(Ba, Sr)Si ₂	MBE	2	Suemasu	
TiN	sputter	4	Kita and Yanagihara	
CrO ₂	CVD	2	Kita and Yanagihara	
Fe ₃ O ₄	MBE	3	Kita and Yanagihara	

Table 1. Typical samples measured with RBS. *R* indicate Eu and/or Tm.

In summary, employing the RBS equipment, we have performed the structural characterization of various thin films. Since this method is very useful as well as powerful to investigate the film structures, the easily accessible RBS facility at UTTAC gives us a great advantage to improve our film growth processes.

References

- [1] Tetsuya Makimura, Hiroshi Uematsu, Keiichi Kondo, Changqing Li and Kouichi Murakami, Applied Surface A, **79**, 799-802 (2004).
- [2] T. Onuma, A. Chakraborty, B. A. Haskell, S. Keller, S. P. DenBaars, J. S. Speck, S. Nakamura, U. K. Mishra, T. Sota and S.F. Chichibu, Appl. Phys. Lett., **86**, 151918 (2005).

4.

ION BEAM ANALYSIS AND APPLICATION

4.1 Status of Tsukuba AMS system

Y.Nagashima, K.Sasa, T.Takahashi, R.Seki, Y.Tosaki, K.Sueki, K.Bessho, H.Matsumura and T.Miura

In last year's Annual Report we reported our new multi gas $\Delta E - SSD E$ counter telescope with which ^{36}S background events in ^{36}Cl yield can be reduced. The performance of the counter is sufficient for the current AMS measurements and it helps to measure ^{36}Cl samples with very low ^{36}Cl content such as 10^{-14} ratio of ^{36}Cl to Cl . The $SSD E$ detector with $48\text{mm} \times 48\text{mm}$ active area was changed to a small $28\text{mm} \times 28\text{mm}$ $SSD E$ detector with no observation of detection losses of particle in ^{36}Cl AMS measurements.

We lost, this year, several scheduled AMS machine times because of unexpected problems happened on the 12UD tandem. Therefore, half of AMS measurements we planned were canceled and consequently the AMS activities were a little bit slowing down. In spite of these conditions, two ^{36}Cl measurements were performed. One was the ^{36}Cl measurement in shielding concrete of various accelerator facilities and another one was the measurement of ^{36}Cl as a tracer in groundwater hydrology. The results of both measurements are reported in the consecutive sections of this annual report.

In the ^{36}Cl -AMS measurements, the fluctuation of ^{36}Cl to ^{35}Cl ratio of the ^{36}Cl standard sample becomes large and sometimes its width is too big to accept as a result. A long effort to find out the origin of the abnormal fluctuation has been executed. At this moment, we have not yet get any clear conclusion, but we are wondering if an AMS ion source works properly or not because we see that a ratio of ^{37}Cl to ^{35}Cl fluctuates abnormally. This abnormal fluctuation is observed at just after a 120degree bending magnet of the ion source. The ^{37}Cl to ^{35}Cl ratio is continuously varied according to the current of Chlorine. This ratio must be constant and be the ratio of a natural abundance of ^{37}Cl and ^{35}Cl . The improvement of the ion source is under going.

Two cooperative studies have been just commenced. One is the joint research work for the ^{36}Cl measurement of 3000m ice core from the Fuji doom in the Antarctic Continent. The drilling of the ice core is progressing smoothly at the Fuji doom as a national project. It has started last summer time and will be continued up to the summer period of 2006. In the last summer time, the ice core has been drilled from surface to about 2000m depth and it has been transferred to the National Institute of Polar Research, Japan. As a first step of the ^{36}Cl AMS of the ice core, we are planning to measure ^{36}Cl in an old ice core which was get at 2002 in order to know the amount of Cl and ^{36}Cl roughly and to estimate the volume of ice core we need for one ^{36}Cl AMS measurement. This project is supported partially by the Grant-in-Aid for Science Research (A)(1) and is executing under the co-operation of the Tsukuba University, the Tokyo University, the Hirosaki University, and the National Institute for Environmental Studies.

A ^{129}I AMS measurement in the soils of the Semipalatinsk nuclear test site is another co-research project. In the period of the Soviet Union, 467 nuclear tests were carried out in this nuclear test site. And consequently, the field has been affected by the very strong radioactive contamination. The radioactive substances produced by a lot of nuclear tests were widely spread in to atmosphere and they were drop on the surface widely as heavy radioactive fallout. Many habitants were influenced by the radioactivity. It is

estimated that the number of peoples who were bombed are more than 1.2 million and still about 350 thousand persons are in pain. Iodine-131, ^{131}I , is a one of major element which is created by the nuclear bomb. Iodine element is one of fundamental element to keep our life. So, it is important to know a spread of ^{131}I radioactive contamination and its density profile of the contamination as accurate as possible from the view point of health examination of victims of radioactivity. the measurement of ^{131}I , however, is almost impossible because a half-life of the ^{131}I is only 8 days and it is almost disappeared now. On the other hand, Adding to the ^{131}I , ^{129}I radio isotope is also created by the nuclear bomb test. Its creation cross section is very small, but a half-life of ^{129}I is long enough, 15.7 million year. This means that the number of ^{129}I is very limited and the ratio of ^{129}I to ^{127}I might be very small, but there is some possibility to be able to measure ^{129}I by our AMS method. Hence, we decided to measure ^{129}I instead ^{131}I to investigate the influence of fallout on the human life. This project is just started as a co-operative study with the Hiroshima University.

4.2 Use of ^{36}Cl as a dating tool for modern groundwater

Y. Tosaki, N. Tase, Y. Nagashima, R. Seki, T. Takahashi, K. Sasa, K. Sueki, T. Matsuhiro¹, M. He², T. Miura³, K. Bessho³, H. Matsumura³ and G. Massmann⁴

Tritium (^3H) has been one of the useful environmental tracers for age dating of modern groundwater (~50 years) because its concentrations in precipitation increased largely as a result of atmospheric nuclear tests conducted during the 1950s and 1960s. Due to the short half-life of ^3H (12.43 years), however, the ^3H “bomb pulse” has been attenuated recently through radioactive decay. Hence, another dating tool which can evaluate the residence time of modern groundwater is necessary in place of ^3H .

The application of long-lived radionuclide chlorine-36 (^{36}Cl) was proposed by Bentley *et al.* [1] as a replacement for ^3H . The fallout rates of ^{36}Cl also increased primarily as a result of nuclear tests at oceanic sites in the 1950s [2]. The ^{36}Cl has a half-life of 301000 years which is much longer than that of ^3H , so the attenuation through radioactive decay can be neglected for the time scale of several decades to centuries. Therefore, the ^{36}Cl bomb pulse has a potential to be a dating tool for modern groundwater. However, there are few detailed studies using the ^{36}Cl bomb pulse as a tracer or dating tool in groundwater.

The objectives of this study are to clarify the relationship between ^{36}Cl content and residence time of groundwater and to demonstrate background level and peak level of the ^{36}Cl bomb pulse and investigate the potential use of ^{36}Cl as a dating tool for modern groundwater.

Groundwater samples were collected at the Oderbruch polder, Germany. In the Oderbruch polder, the shallow aquifer is mainly recharged by the infiltration from the Oder River. Sampling points are located along the flow path of groundwater. Other groundwater samples were collected at Tsukuba Upland, Ibaraki, Japan. The sampling depth ranges from 7 m to 240 m below the surface.

For ^{36}Cl analysis, groundwater samples were prepared as AgCl [3]. The $^{36}\text{Cl}/\text{Cl}$ ratios of groundwater samples were measured by the AMS (accelerator mass spectrometry) at the Applied Accelerator Division, Research Facility Center for Science and Technology, University of Tsukuba.

From the results of measurements, background level of $^{36}\text{Cl}/\text{Cl}$ ratios at the Oderbruch polder was estimated to be $7\text{-}9 \times 10^{-14}$. The $^{36}\text{Cl}/\text{Cl}$ ratios of groundwater samples which were dated by $^3\text{H}/^3\text{He}$ method [4] showed good agreement with Dye-3 ice core data [2] (Fig. 1). Consequently, it was revealed that the distribution of bomb-produced ^{36}Cl (bomb- ^{36}Cl) in groundwater corresponded to the fallout pulse.

The depth profile of $^{36}\text{Cl}/\text{Cl}$ ratios of groundwater samples at Tsukuba Upland showed a peak around 30 m below the surface (Fig. 2), and it agreed well with that of ^3H concentrations (Fig. 3). From the $^{36}\text{Cl}/\text{Cl}$ ratios of groundwater deeper than 55 m, background level at Tsukuba Upland was estimated to be $1\text{-}2 \times 10^{-13}$. From the time series of $^{36}\text{Cl}/\text{Cl}$ ratios (input $^{36}\text{Cl}/\text{Cl}$ values to groundwater) at Tsukuba Upland estimated using Dye-3 data, residence time of groundwater was estimated to be about 50 years at 40 m and 30 years at 30 m (Fig. 4).

In conclusion, it was demonstrated that the residence time of groundwater in a region could be estimated if

¹ Present address: Saitama Rubber Mfg. Co., Ltd.

² Present address: Department of Nuclear Physics, China Institute of Atomic Energy, China

³ Radiation Science Center, High Energy Accelerator Research Organization

⁴ Department of Earth Sciences, Free University of Berlin, Germany

the determination or estimation of time series of $^{36}\text{Cl}/\text{Cl}$ ratios is possible.

Acknowledgements

We are grateful to Dr. Masaya Yasuhara and Dr. Makoto Takahashi (Geological Survey of Japan, AIST) for allowing us to take groundwater samples and assisting us with the sampling at Tsukuba Upland. We also thank Mr. Seong Won Lee (Master's Program in Environmental Sciences, University of Tsukuba) for his assistance in the groundwater sampling.

References

- [1] H.W. Bentley, F.M. Phillips, S.N. Davis, S. Gifford, D. Elmore, L.E. Tubbs and H.E. Gove, *Nature* **300** (1982) 737.
- [2] H.-A. Synal, J. Beer, G. Bonani, M. Suter and W. Wölfli, *Nucl. Instr. Meth.* **B52** (1990) 483.
- [3] Y. Nagashima, R. Seki, T. Takahashi and D. Arai, *Nucl. Instr. Meth.* **B172** (2000) 129.
- [4] J. Sültenfuß and G. Massmann, *Grundwasser* **9** (2004) 221.

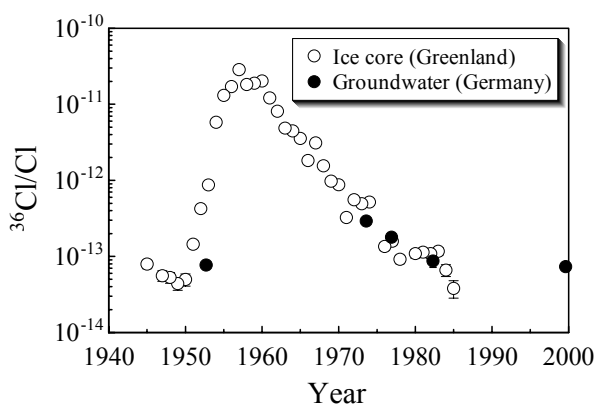


Fig. 1. Comparison of $^{36}\text{Cl}/\text{Cl}$ ratios in groundwater and ice core [2].

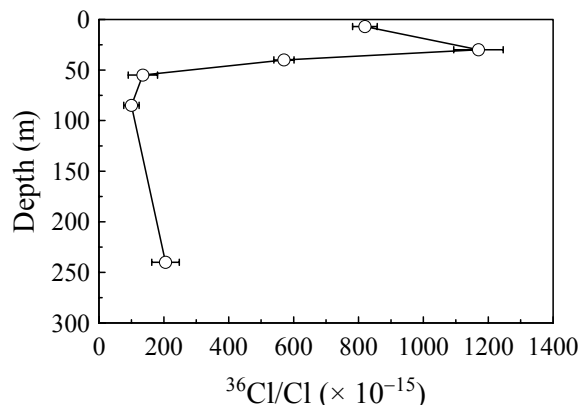


Fig. 2. Depth profile of $^{36}\text{Cl}/\text{Cl}$ ratios in groundwater at Tsukuba Upland.

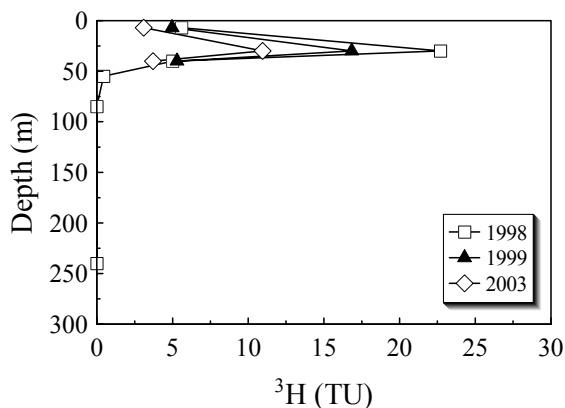


Fig. 3. Depth profiles of ^3H concentrations in groundwater (Yasuhara, M., private communication).

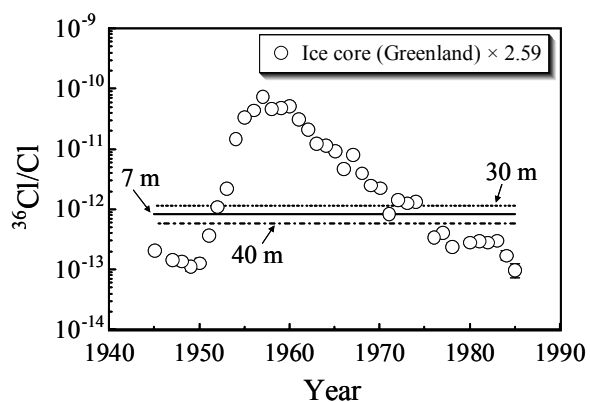


Fig. 4. Estimation of groundwater residence time at Tsukuba Upland.

4.3 AMS of ^{36}Cl in shielding concrete of various accelerator facilities

K. Bessho¹, H. Matsumura¹, T. Miura¹, Q. Wang¹, K. Masumoto¹, Y. Nagashima, R. Seki, T. Takahashi, K. Sasa, K. Sueki, and Y. Tosaki

At accelerator facilities, concrete components around beam lines are exposed to secondary particles during machine operation, and various long half-life radionuclides, such as ^3H , ^{22}Na , ^{36}Cl , ^{46}Sc , ^{54}Mn , ^{60}Co , ^{134}Cs , and ^{152}Eu , are accumulated in the concrete. Concentrations of the radionuclides induced in the concrete are important for radioactive waste management of accelerator facilities. If we can obtain the thermal neutron fluence during machine operation, it will be useful information for estimating the radioactivities of the nuclides because most of the radionuclides are mainly produced by thermal neutron-capture reactions. In our previous studies, we have developed a method for AMS of ^{36}Cl in concrete of accelerator buildings, successfully applied for various accelerator facilities, and suggested that the measurements of isotope ratios of ^{36}Cl to ^{35}Cl ($^{36}\text{Cl}/^{35}\text{Cl}$) is suitable for monitoring the thermal neutron fluences [1,2].

In this year, concrete samples were newly collected at two kinds of accelerator facilities, which are a cyclotron at the Nishina Memorial Cyclotron Center (The Japan Radioisotope Association) and 45 MeV Electron LINAC (Hokkaido University), and the depth profiles of $^{36}\text{Cl}/^{35}\text{Cl}$ and specific activities of γ -ray emitters and ^3H in the concretes were obtained by AMS, γ -ray spectrometry, and β -ray counting, respectively. Based on these results, the suitability of $^{36}\text{Cl}/^{35}\text{Cl}$ as a monitor for thermal neutron fluence was discussed.

The target-preparation procedure and AMS of ^{36}Cl were described in detail in our previous reports, and accuracy and reproducibility of the analysis had been confirmed [1,2]. An example of the results obtained for the Nishina Memorial Cyclotron Center is reported.

Fig. 1 shows the depth profiles of $^{36}\text{Cl}/^{35}\text{Cl}$ together with the specific radioactivities of ^{60}Co , ^{152}Eu , ^{134}Cs , ^{46}Sc , ^{54}Mn , and ^3H in the floor concrete of the cyclotron facility. The maximum $^{36}\text{Cl}/^{35}\text{Cl}$ was observed at approximately 5 cm in depth from the surface, and the depth profile of $^{36}\text{Cl}/^{35}\text{Cl}$ was good agreement with those of ^{60}Co , ^{152}Eu , ^{134}Cs , ^{46}Sc , and

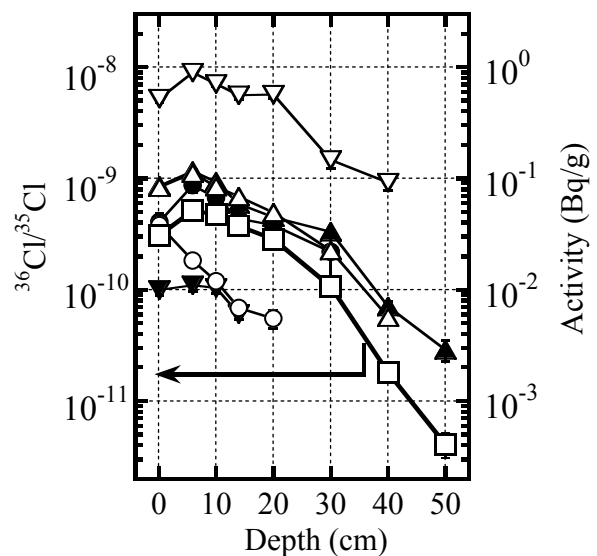


Fig. 1 Depth profiles of $^{36}\text{Cl}/^{35}\text{Cl}$ (\square) and the specific radioactivities of ^{60}Co (\blacktriangle), ^{152}Eu (\bullet), ^{134}Cs (\blacktriangledown), ^{46}Sc (\triangle), ^{54}Mn (\circ), and ^3H (\triangledown) induced in the floor concrete at the Nishina Memorial Cyclotron Center. The scale of $^{36}\text{Cl}/^{35}\text{Cl}$ is shown in the left-hand axis, and those of radioactivities of other nuclides are shown in the right-hand axis.

¹ Radiation Science Center, High Energy Accelerator Research Organization

^3H , which are nuclides formed by thermal-neutron induced reactions. In contrast with these nuclides, ^{54}Mn , which is formed by fast neutrons, showed the maximum activity at the surface and monotonously decreased with increase in the depth from the surface. These characteristics were also observed at other accelerator facilities [1,2] and attributed the ^{36}Cl productions in the concrete to thermal neutron capture of ^{35}Cl .

In order to examine the capability of ^{36}Cl AMS for thermal neutron monitor, the thermal neutron fluences estimated from the $^{36}\text{Cl}/^{35}\text{Cl}$ are compared with those estimated from the isotope ratios of ^{60}Co and ^{152}Eu to stable Co and Eu. The concentrations of Co and Eu in the floor concrete of the accelerator facility were determined to be 7.4 ppm and 0.68 ppm by using instrumental neutron activation analysis.

In the evaluation of neutron fluences from the radioactivity of ^{60}Co and ^{152}Eu , it was assumed that the cyclotron had been continuously operated and the neutron flux at the sampling point had been constant since 1989 to 2003. The cross sections used to estimate thermal neutron fluences were 43.6 barn for $^{35}\text{Cl}(n,\gamma)^{36}\text{Cl}$, 37.2 barn for $^{59}\text{Co}(n,\gamma)^{60}\text{Co}$, and 5900 barn for $^{151}\text{Eu}(n,\gamma)^{152}\text{Eu}$, respectively [3].

The estimated fluences calculated by the data of three nuclides are shown in **Fig. 2**. The results show good agreement with each other, which confirmed that the $^{36}\text{Cl}/^{35}\text{Cl}$ measurement is suitable for monitoring the thermal neutron fluences irradiated during the accelerator operations. The estimation of neutron fluences generally depends on the relation between the half-life of radionuclides and the operational history of accelerator, which is difficult to be exactly clarified. In case of evaluation using ^{36}Cl AMS, operational histories of accelerators are not indispensable because radioactive decay of ^{36}Cl during accelerator operation can be neglected. Furthermore, $^{36}\text{Cl}/^{35}\text{Cl}$ can be directly determined. AMS of ^{36}Cl enables simple and reliable evaluations of neutron fluences without indefinite assumptions, and this technique will be powerful and effective tool for monitoring cumulative neutron fluences for a long period.

References

- [1] K. Bessho et al., UTTAC-71 (2003) 99.
- [2] K. Bessho et al., UTTAC-72 (2004) 73.
- [3] R.B. Firestone, V.S. Shirley, ed.: Table of Isotopes, 8th ed., Wiley-Interscience, New York 1996.

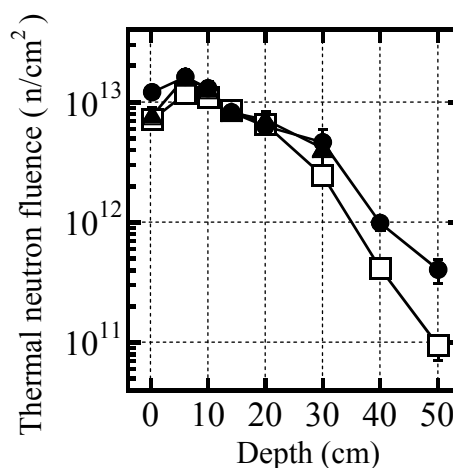


Fig. 2. Thermal neutron fluences estimated with $^{36}\text{Cl}/^{35}\text{Cl}$ (□) and the specific radioactivities of ^{60}Co (▲) and ^{152}Eu (●) in the floor concrete at the Nishina Memorial Cyclotron Center.

4.4 Latent tracks and etched tracks in rutile TiO₂ single crystals

K. Awazu¹, T. Ikeda², T. Komatsubara

Introduction

In most insulators a strongly damaged zone is induced along the ion path by the slowing down of a swift heavy ion. Although much work has been done in order to describe damage mechanism, structure of latent track from the view point of material science has not been clear. Our experiment in 2004 aimed to observe the structures of latent tracks. Also the authors examined why the damaged doze was well dissolved in hydrofluoric acid to create etched tracks.

Experiment

The samples used in the present experiment were (100) rutile TiO₂ single crystal plates synthesized by the Verneuil flame-fusion method. To avoid overlap of the latent tracks, a very low accumulated dose, typically $1 \times 10^{10} \text{ cm}^{-2}$, was applied by diffusing the ion beam with a freestanding foil in forward scattering geometry. High-resolution electron microscope (HREM) were also employed to observe the sample surfaces. Chemical etching was performed with 20% hydrofluoric acid, (hereinafter 20% HF), at room temperature.

Results and discussion

Fig.1. (a) and (b) show HREM bright images with different scales of the rutile (100) single crystal subjected to irradiation with 50MeV and 115MeV Br ions at an accumulated dose of $1.0 \times 10^{10} \text{ cm}^{-2}$, respectively, an appropriate dosage for observing individual latent tracks without overlap. In Fig. 1.(a) and (b), latent tracks are seen to have a milky color, and an amorphous “island” with a radius of $1.5 \pm 1 \text{ nm}$ and $2 \pm 0.6 \text{ nm}$, respectively, can be observed in the “sea” of crystallographic orientation. It is also clear that atoms far from the latent track were in place; however, the pattern of the atoms near the latent track, probably as a result of the stress introduced by the passage of a swift heavy ion. The radius of the stressed region in TiO₂ bombarded with 50MeV and 115MeV Br ions was estimated about $2.5 \text{ nm} \pm 0.4 \text{ nm}$ and $2.6 \text{ nm} \pm 0.5 \text{ nm}$, respectively.

After etching with 20% hydrofluoric acid for TiO₂ plates bombarded with 50MeV and 115MeV Br ions, HREM observation was performed and shown in Fig.1. (c) and (d), respectively, and the diameter of each etched parts was estimated at $2.5 \text{ nm} \pm 0.4 \text{ nm}$ and $4.0 \text{ nm} \pm 0.6 \text{ nm}$, respectively. It is noticed that the etched part is not only amorphous region but stressed region.

¹ National Institute of Advanced Industrial Science and Technology

² Waseda University

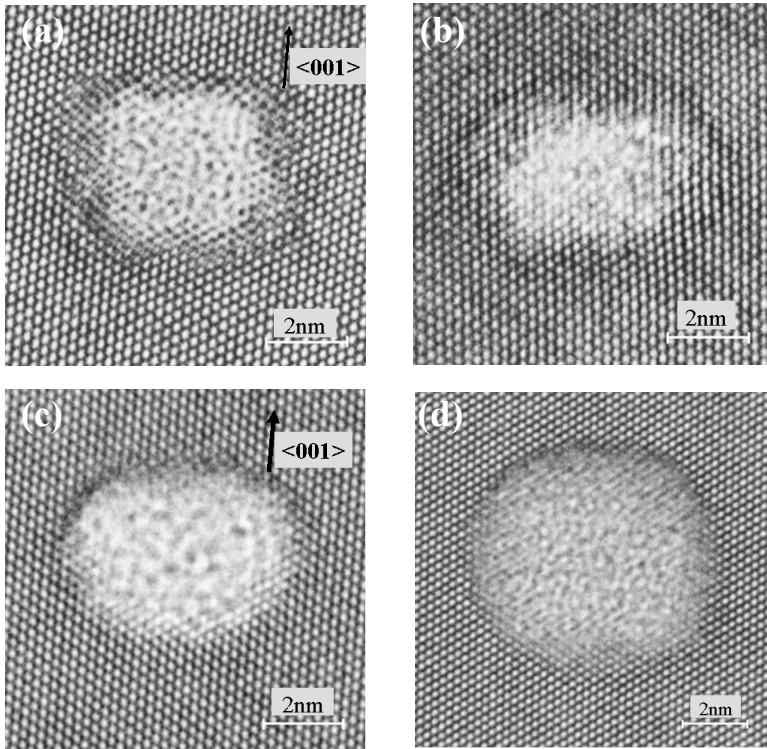
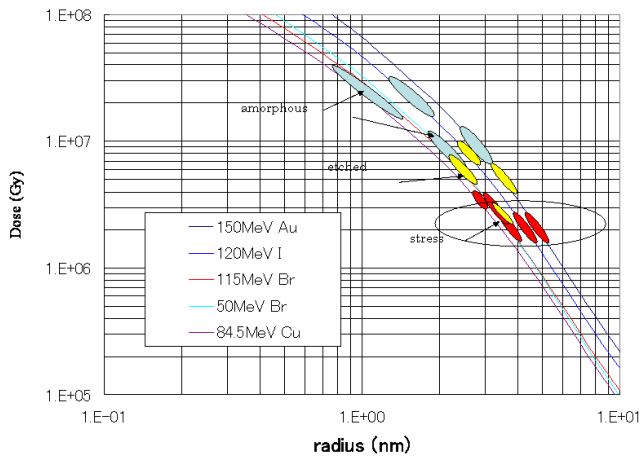


Fig.1. High-resolution electron microscope (HREM) observation of rutile single crystals of TiO_2 bombarded with (a) 50MeV Br and (b) 115MeV Br ions. After etching with 20% hydrofluoric acid were shown in (c) and (d), respectively.

Monte Carlo calculations [1] of the radial distribution of dose in TiO_2 were performed for 150MeV Au, 120MeV I, 115MeV Br, 50MeV Br and 84.5MeV Cu ions and shown in Fig.2. Also radius of amorphous, stressed and etched parts directly observed by HREM was plotted with open circles. Radius of the etched



parts was located between radius of amorphous parts and radius of stressed parts.

Fig.2. Radial distribution of energy deposited around the path of ions. Circles were data from HREM views of amorphous, etched and stressed parts.

The research involved with this project was made possible through funds from the Atomic Study Research Funding of the Ministry of Education, Culture, Sports, Science, and Technology based on an assessment of the Japanese Atomic Energy Commission.

References

- [1] M.P.R. Waligorski, R.N. Hamm and R.Katz, Nucl. Tracks Radiat. Meas., 11, 309 (1986).

4.5 Radio isotope implantation using a sputtering negative ion source

T. Aoki and N. Yoshikawa¹⁾

It is interesting to implant particular radioisotope, ^{111}In , into many kind of substances to get samples for perturbed angular correlation (PAC) experiment. The ^{111}In isotope is quite suitable nucleus to investigate electron transition rates and electron densities in the substance by performing PAC experiment. Since ^{111}In nucleus decays to ^{111}Cd nucleus through electron capture process (EC), the daughter nucleus ^{111}Cd has many electron holes in electron orbits just after the EC process. The holes generate strong electro magnetic force onto the ^{111}Cd nucleus. Therefore the ^{111}Cd nucleus is affected by the force and shows strong perturbation in the angular correlation pattern. The lifetimes of the holes are related to the electron transition rates and electron density of the substances. If the holes are destroyed, the perturbation is ceased. Therefore, observing the degree of the perturbation leads to knowledge of life of holes and density of the electrons. To do this kind of experiments, it is essential to get ability to implant ^{111}In into many substances easily. From this point of view, a test for implanting ^{111}In nucleus was made by using a sputtering negative ion source in the RI division

The radio isotope ^{111}In was produced by reaction $^{109}\text{Ag}(\alpha, 2n)^{111}\text{In}$. The Ag foil target was put on cathode head and was bombarded for several hours by the α beam accelerated by the tandem accelerator. The beam energy was 20 MeV and the intensity was about 100 nA. After cooling short lifetime activities for 12 hours, the cathode head was set in the ion source. The activity ^{111}In was sputtered by Cs ion and was extracted and accelerated to the energy of 147 keV. Mass of the activity was analyzed by a magnet and the activity was implanted into Al foil. Gamma ray spectrum from ^{111}In implanted in the Al foil was shown in Fig.1 along with that from the cathode before implantation. Implantation efficiency, which is given as ratio of the intensity of radiation from implanted isotope to that from the cascade before implantation process, is seen to be about 0.2 % judging from Fig.1. Typical efficiencies for other radioisotopes, ^{32}P and ^{125}I , were of the order of 10 to 20 % usually. The extremely small value of 0.2 % was obtained because failure in ion source operation happened this time.

1

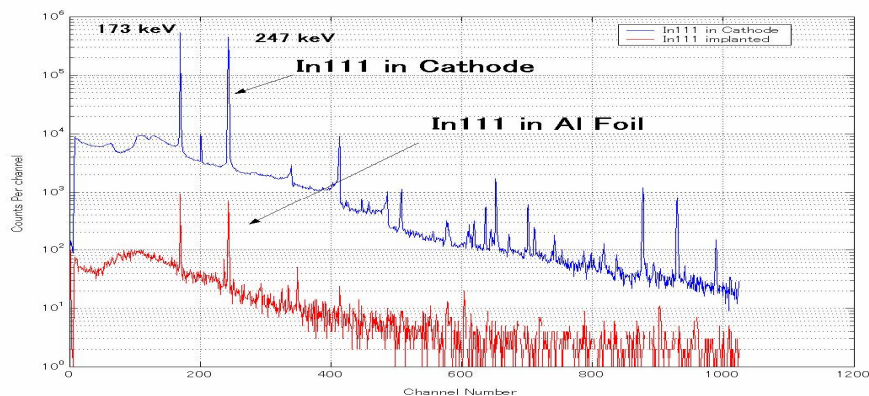


Fig 1. ^{111}In Gamma-ray spectra from cathode and Al backing.

¹ K.E.K. Tsukuba-shi, Oho 1-1, 305-0801, Japan

4.6 Measurement of He distribution in 40keV He irradiated stainless steel by means of ERDA with 16MeV O⁵⁺ beam

T. Toriyama¹, H. Wakabayashi¹, T. Kawabata¹, S. Uemura¹, K. Sasa, K. Shima, N. Hayashi² and I. Sakamoto³

Austenitic stainless steels such as SUS304 are used as structural materials for super-conducting magnets in fusion reactors. Since the nuclear cross section of the constituent elements (Fe, Cr and Ni) for (n, α) reactions are considerably large for fast neutrons, helium is produced and accumulated in the materials by neutron irradiation. Thus it becomes important to understand the influence of the helium accumulation in austenitic stainless steel, especially the decrease of the strength through the He induced martensitic transformation of fcc (γ) to bcc (α) structure. The direct irradiation of He ions has been utilized to observe this transformation process efficiently and its transformation has been investigated using Conversion Electron Mössbauer Spectroscopy (CEMS) and X-ray Diffraction (XRD) [1, 2]. In these studies, it was found that the martensitic transformation was induced by the He gas bubbles formed in the implanted layer. Furthermore, the SUS304 austenitic stainless steel foils (100 μm in thickness) annealed for eliminating the stress-induced martensitic phase were irradiated by 40 keV He ions in the dose of 3.6×10^{17} , 7.2×10^{17} and 10.8×10^{17} ions/cm² and investigated by CEMS, XRD and Secondary Electron Microscope (SEM) [3, 4]. As a result, it was found that before He-irradiation induced martensitic transformation has occurred, the modified austenitic phase (γ'') whose lattice constant is about 0.5% larger than that of γ -phase is formed. At the present time, the He induced martensitic transformation in SUS304, SUS304S and SUS316 austenitic stainless steels has been studied by CEMS, XRD and SEM. In these studies, it becomes to be important to investigate the relation between the depth of martensitic transformation and the irradiated He distribution for SUS304 and SUS316 samples [5].

Elastic Recoil Detection Analysis (ERDA) is the most suitable technique for observing the distribution of light elements in surface region of the samples. Fig.1 shows an experimental setup of ERDA with 16MeV O⁵⁺ beam. The beam is collimated by the first aperture of 1.0 mm in diameter and the second aperture of 2.0

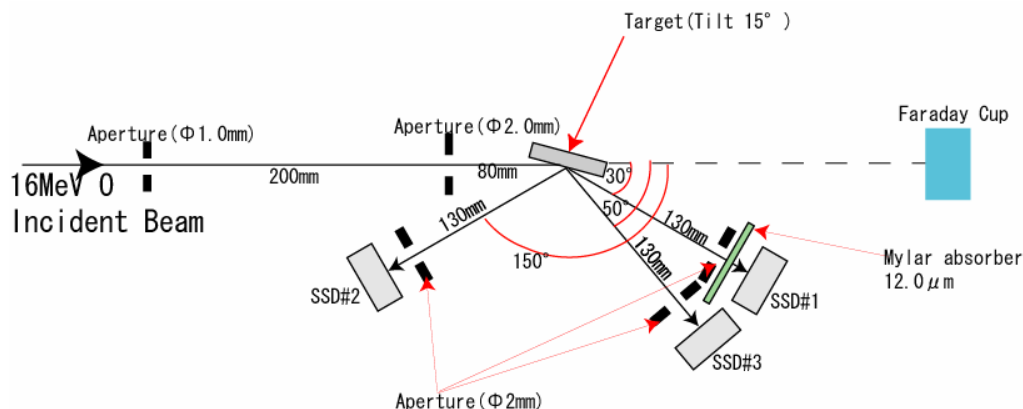


Fig.1. Experimental setup for ERDA

¹ Musashi Institute of Technology, ² Kurume Institute of Technology, ³ Advanced Industrial Science and Technology

mm in 200 mm distance. The sample surface is tilted at the angle of 15° relative to the beam and ERDA detector (SSD#1) is placed at the scattering angle of 30° and 130 mm distance. A Mylar absorber with thickness of $12.0\ \mu\text{m}$ was used for preventing the forward scattered O beam from impinging on SSD#1. Two RBS detectors, SSD#2 and SSD#3 with the aperture of 2 mm diameter were placed at the scattering angles of 150° and 50° and both 130 mm distances, respectively. The former was used for measuring the dose of O beam to the sample and the latter was used for monitoring the forward scattering O and elastic back-scattering light elements.

Fig.2 shows ERDA spectra for 40 keV He irradiated SUS316 samples with dose of a) 7.2×10^{17} ions/cm² and b) 10.8×10^{17} ions/cm². The fitted solid line curves obtained using the simulation program SIMNRA [6] also are shown in the spectra, respectively. For the former with dose of a) 7.2×10^{17} ions/cm², only the modified austenitic phase (γ'') was observed by XRD and it was confirmed that the He bubbles in the surface are not formed by SEM. On the other hand, for the latter with dose of b) 10.8×10^{17} ions/cm², it was confirmed that the He induced martensitic transformation occur by CEMS and XRD and also the He bubbles in the surface are formed by SEM. It could successfully be observed that for the sample with dose of b) 10.8×10^{17} ions/cm² a part of the He atoms moves nearer to the surface than those for the sample with dose of a) 7.2×10^{17} ions/cm².

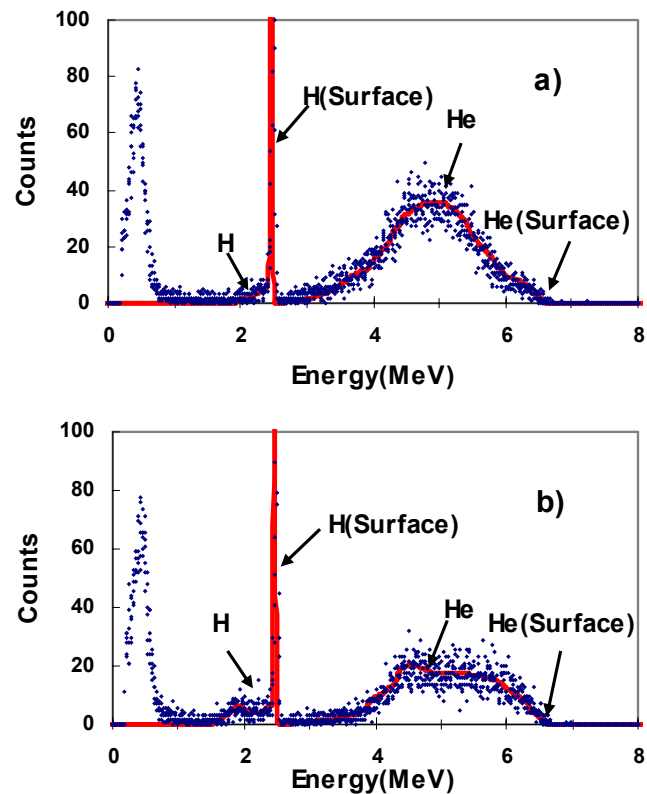


Fig.2. ERDA spectra for 40 keV He irradiated SUS316 sample with dose of a) 7.2×10^{17} ions/cm² and b) 10.8×10^{17} ions/cm².

References

- [1] N. Hayashi and T. Takahashi, Appl. Phys. Lett. **41**, (1982) 1100.
- [2] E. Johnson, L. Gråbæk, A. Johansen, L. Saholt-Kristensen, P. Børgensen, B.M.U. Scherzer, N. Hayashi and I. Sakamoto, Nucl. Instr. and Meth. in Phys. Research **B39** (1989) 567.
- [3] T. Toriyama, T. Ishibashi, N. Hayashi, I. Sakamoto, K. Nishio, H. Wakabayashi and H. Iijima, IEEE, Ion Implant. Technol. vol. **2**, (1999) 783.
- [4] T. Namiki, C. Kaneko, H. Wakabayashi, T. Toriyama, N. Hayashi and I. Sakamoto, Rep. Res. Cent. Ion Beam Technol., Hosei Univ., Suppl. **18** (1999) 179.
- [5] Y. Matsui, C. Kaneko, H. Wakabayashi, T. Toriyama, N. Hayashi and I. Sakamoto, Proceedings of First 21st Century Combination Symposium -Science, Technology and Human- (Mirai CAN Hall, Tokyo, 2002 Nov.) pp.415-418 (in Japanese).
- [6] Matej Mayer, SIMNRA, <http://www.rzg.mpg.de/~mam/index.html>.

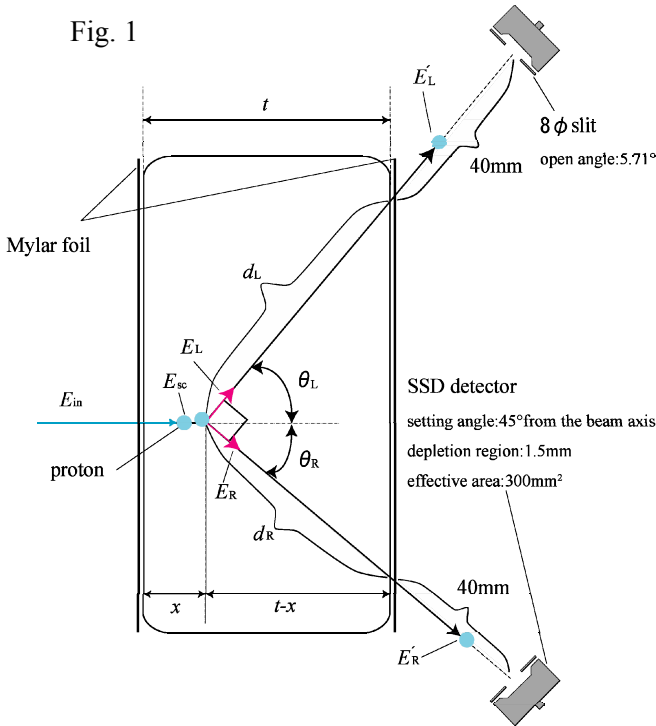
4.7 Shape measurement of melt inclusion in a mineral sample

K.Satou, K. Komatsubara, T. Kurosawa, K. Sasa, S. Ishii, Y. Yamato and K. Miyakawa

To analyze hydrogen density inside a solid state sample, ERCS (Elastic recoil coincidence spectrometry) method [1] using 30 μm proton micro beam of 20 MeV from the tandem accelerator has been developed at UTTAC. In this method, both kinetic energies of two protons, which are scattered inside the sample elastically, are measured simultaneously by two SSDs which are set at 45 degrees with respect to the beam axis. Sum of the measured kinetic energies (sum energy spectrum) provide a depth profile of hydrogen content. Figure 1 shows an experimental setup.

It is important to formulize the energy spectrum of SSDs. The stopping power ($S(E)$:[MeV/ μm]) of proton inside a target can be well approximated using the formula of as follow,

$$S(E)=a\rho E^b(a, b: \text{fitting parameters}, \rho: \text{density})---(1).$$



The fitting parameters “a” and “b” depend on an element composition of a target material. Those for quartz are 0.0228 and -0.779, respectively. When an incident proton with energy E_{in} passes through a uniform target having depth t , the out-put energy E_{out} can be calculated as

$$E_{in}^{1-b}-E_{out}^{1-b}=a\rho(1-b)t---(2).$$

Since we now take into account only the elastic scattering, the relation between scattering conditions (E_{sc} , x , $\theta_{L,R}$) and measured proton energy ($E'_{L,R}$) can be formulized as

$$\rho x = \frac{E_{in}^{1-b} \cos^{3-2b} \theta_L - E'_L \cos \theta_L - a(1-b)\rho t}{a(1-b)(\cos^{3-2b} \theta_L - 1)}$$

$$= \frac{E_{in}^{1-b} \sin^{3-2b} \theta_L - E'_R \sin \theta_L - a(1-b)\rho t}{a(1-b)(\sin^{3-2b} \theta_L - 1)} ---(3).$$

Therefore the scattering point x [μm], scattering angle (θ_L , θ_R), and recoil energy (E_L , E_R) can be obtained with the help of the measured kinetic energy (E'_L , E'_R) and the target-depth t using eq. (3). Furthermore, for the case of the multi-layer target like fig. 2 we can formulize the energy E'_{out} as follows,

$$E'_{out} = \left[\left\{ E_{in}^{1-b} - a\rho(1-b)x \right\}^{(1-b)/(1-b')} - a'\rho'(1-b')t' \right]^{(1-b)/(1-b')} - a\rho(1-b)(t-x-t')$$

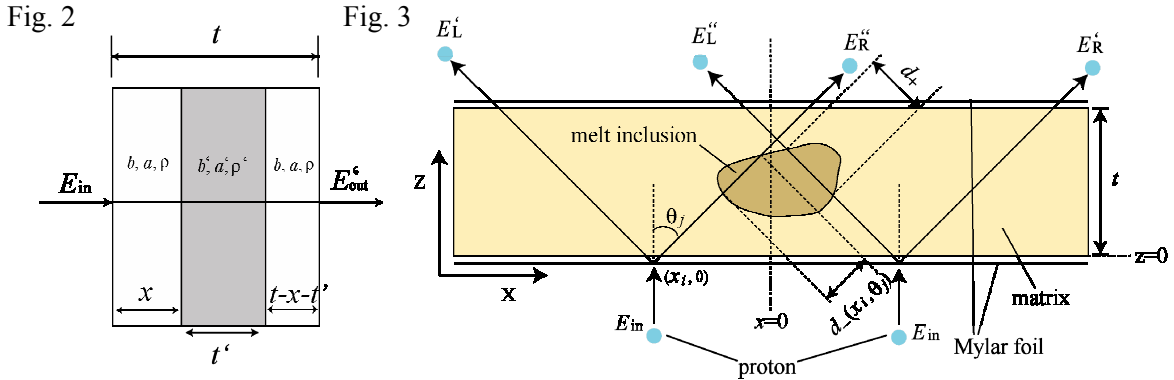
if $b \approx b' \approx b''$ and $a \approx a' \approx a''$, then

$$= E_{in}^{1-b} - a\rho(1-b)t + a''(1-b'')(\rho - \rho')t' ---(4).$$

Note that the eq. (4) is independent of x .

We have applied this method to hydrogen analysis of a melt inclusion included in a volcanic rock. Here, the melt inclusion contains hydrogen inside and has a similar element composition to the matrix, thus has similar “a” and “b” values, but its density ρ is differ from that of the matrix. For instance, for the case of

the Boninite outputted in Titijima island, (a, b, ρ) values of the matrix are $(0.0201, -0.0753, 3.45 \text{ [g/cm}^3\text{)})$, while those of the melt inclusion are $(0.0201, -0.750, 2.74 \text{ [g/cm}^3\text{)})$. When size of the melt inclusion is sufficiently large compared to the beam size of about $30 \mu\text{m}$ and the target thickness of $100 \sim 200 \mu\text{m}$, the sample can be regarded as a simple multi layer target like Fig. 2. However, when the size is comparable with the target thickness, we need its shape information for accurate analysis.

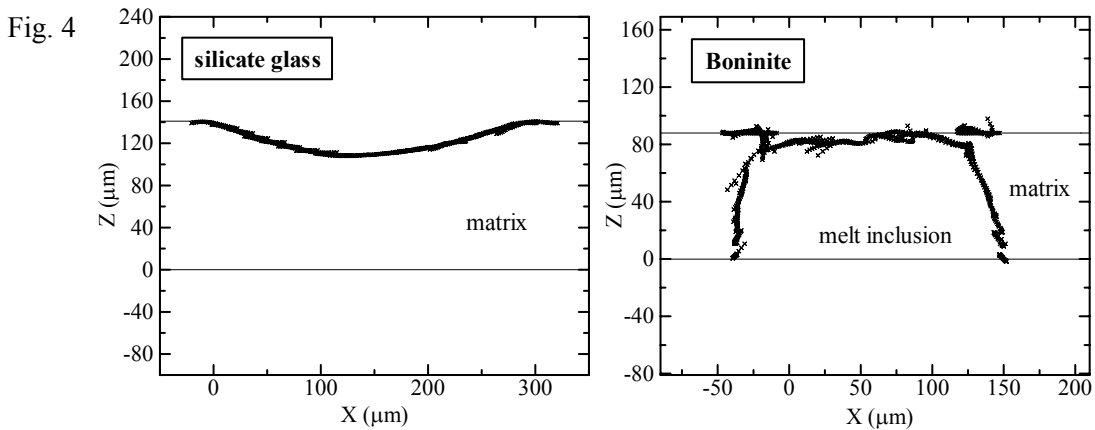


To obtain the shape of the melt inclusion, we applied the ERCS method. We irradiated a sample with the proton micro beam of $30 \mu\text{m}$ such that only one proton passes through the melt inclusion like Fig. 3, and obtained crossing length through the melt inclusion, $d_{+,j}$, from the formula (eq. (5)) derived from eq. (4).

$$E_{L,R}^i(x_i, \theta_j) - E_{L,R}^f(x_f, \theta_j) = (\rho - \rho') a'' (1 - b'') d_{+,j}(x_i, \theta_j) \quad (5)$$

Here the angle θ covers from $45-2.9$ to $45+2.9$ degrees. We measured two samples. One was a silicate-glass sample which had a cavity cropped out on the beam exit side, and the other was the Boninite sample which had a melt inclusion cropped out on the beam incident side. The thicknesses of these samples were 141 and $88 \mu\text{m}$, respectively. The adopted “ a ” and “ b ” values for the silicate-glass were 0.184 and -0.768 , respectively, and the density is $2.83 \text{ [g/cm}^3\text{)}$, while the adopted “ a ” and “ b ” values for the Boninite were 0.0201 and -0.752 , respectively. We constructed the obtained experimental data-set $d_{+,j}$ consistently and obtained the shape of the cavity and the melt inclusion as shown in Fig. 4.

By using the shape information measured from this method, we can analyze the sum energy spectrum accurately to obtain the depth profile of hydrogen content inside the small melt inclusion.



References

- [1] B.L. Cohen, C.L. Fink and J.H. Degnan, J. Appl. Phys., **43**, 19 (1972)

4.8 Development of ERCS hydrogen analysis for geological samples

T.Komatsubara, K.Sasa, K.Miyakawa, S.Ishii, Y.Yamato, K.Satou, M.Kurosawa

Hydrogen analysis for melt inclusions is very important for geological science to understand dynamical mechanism of magmatic activities. The melt inclusion is tiny object found in a volcanic quartz which can be regarded as a specimen of the melting magma. Since the size of the melt inclusion is in range from 10 to several hundred micro meters, microbeam is necessary for the analytical study.

In order to analyze hydrogen content, proton-proton elastic recoil coincidence spectrometry (ERCS) has been performed. For the evaluation of the hydrogen density profile, a practical method has been developed. By using this new method, measured sum energy spectrum can be modified to become depth profile of hydrogen density.

For the calibration of the hydrogen intensity, mylar, kapton and polyethylene films were irradiated as the standard materials. As the lowest point of the hydrogen concentration, a metallic foil of Ti(H) was irradiated in which the Ti(H) sample was provided by NIST and the hydrogen weight ratio was reported as 49 ppm. All of the measured values were well proportional to the calibrated hydrogen densities.

For the observation of the beam shape by using the micro scope system, several fluorescent materials were irradiated and examined. Synthetic ruby showed brightest luminescence of red color. It could be most suitable to identify weak intensity of a dim beam profile. A thin plate of synthetic spinel also exhibited quite bright luminescence of green color. When a slice of a scheelite was irradiated, the beam profile was clearly observed as the dark blue spot. The scheelite could be useful for the evaluation of the beam size without strong halation.

In order to achieve higher detection efficiency, new surface barrier Si detectors have been installed with the larger solid angle. The detection area of the new detectors is 300 mm² and the effective thickness is 1500 mm. Larger detector windows of ϕ 8 mm in diameter were also newly installed in front of the detectors at 40 mm from the irradiation point. Detection solid angle is increased to be more than twice.

For the improvement of S/N ratio in the measured proton spectrum, origins of the background are considered as; (1) edge scattering at the detector windows, (2) scattering at aluminum foils of the light shield, (3) chance coincidence, (4) pile up, and (5) dispersion of incident beam. For the reduction of the edge scattering, inner surfaces of the detector windows were polished to be mirror surfaces. Pile up rejection system is installed by connecting PUR signal from ORTEC 572 amplifier to SEIKO ADC1821.

Contribution of the chance coincidence is measured to be about 10 % of total background. In this measurement, a quartz target of 0.2 mm in thickness was irradiated by 100 pA proton beam.

As a sample of the clean spectrum, sum energy spectrum for a mylar sample is shown in Fig. 1. Peak to total ratio of 93% has been achieved.

Acknowledgements

This work is supported in part by the Grant-in-Aid for Science Research of Japan Ministry of Education, Culture, Sports, Science and Technology, under grant no. 165404036.

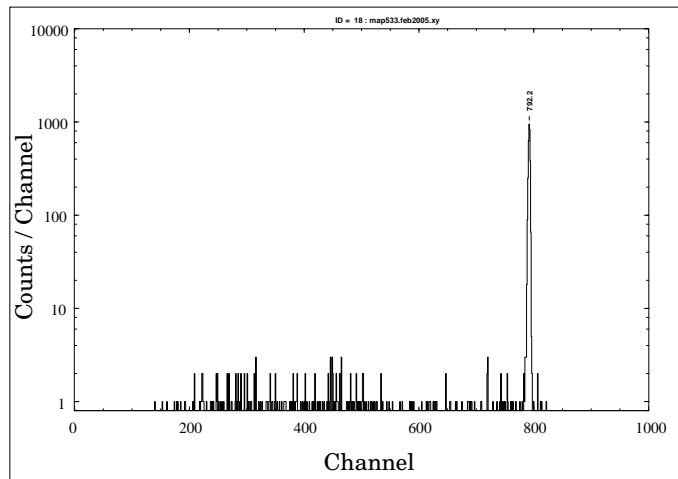


Fig.1 Measured sum spectrum for one mylar target of $2.5 \mu\text{m}$ in thickness. Back ground is reduced to be only 7% with respect to the mylar peak intensity.

4.9 Trace element determination of silicate rock reference material JB-1a by using particle-induced X-ray emission

M. Kurosawa, K. Shima, S. Ishii, K. Sasa, and T. Komatsubara

Particle-induced X-ray emission (PIXE) is a nondestructive analytical technique based on the measurement of characteristic X-rays induced by a proton microbeam of MeV energy directed onto the specimen surface. This technique demonstrates a precision and an accuracy of within $\pm 10\%$ for most elements at levels of a few $\mu\text{g g}^{-1}$ to tens $\mu\text{g g}^{-1}$ in glasses and minerals [1–3]. However, there have been few PIXE analyses for silicate rock reference materials. Thus, we have determined trace-element concentrations in fused glasses of a rock reference material issued by the Geological Survey of Japan determined using PIXE to investigate the suitability of quantification for the analysis of trace elements in solid samples.

Samples used in this study were a fused-glass bead prepared from silicate rock reference powders JB-1a (basalt). The rock powder was fused in a platinum capsules by means of a radio-frequency heating furnace. A small piece (1 mm) of the glass was mounted in an epoxy resin and polished using a 0.3-mm alumina paste. No compositional zoning or crystalline inclusions were observed in the glass bead by optical microscopy. To check for chemical homogeneity, major-element compositions were analyzed with an electron microprobe (EPMA).

PIXE analyses were carried out using a 4-MeV proton beam [4, 5]. The beam incidence was normal to the sample surface, and the X-ray measurement take-off angle was 45° . A 150- μm -thick aluminum filter was used to attenuate the intense X-rays from Si in the sample and to prevent the entry into the detector of protons scattered from samples. The beam current was set at 0.6–1.3 nA and the collected beam charge was 0.95–4.61 μC . The beam size was about $100 \times 100 \mu\text{m}^2$. The sample was analyzed at three points across the glass bead. Quantification was performed on the basis of the model of Campbell [6], in which total X-ray intensities of an element generated from a proton-beam path in a

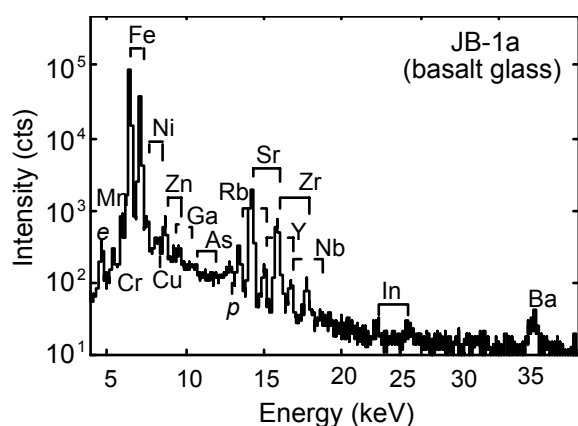


Fig. 1 X-ray spectrum of JB-1a glass recorded using 4.61 μC of 4MeV protons with 150- μm aluminum filter.

sample are calculated by considering the attenuation of the energy of the incident protons and the absorption of the X-rays by the sample matrix. Theoretical X-ray intensities for each element per $1 \mu\text{g g}^{-1}$ of a sample matrix with known major-element composition are first calculated by volume integration using the physical parameters of the sample materials and the measurement conditions. The measured X-ray intensities for each element of interest in the sample are divided by the theoretical X-ray intensities per $1 \mu\text{g g}^{-1}$ and are converted to the element concentration. Details of the quantification method are presented elsewhere [5].

In a measured spectrum of JB-1a (Fig. 1), the K_{α} and K_{β} peaks from Cr, Mn, Fe, Ni, Cu, Zn, Ga, As, Rb, Sr, Y, Zr, Nb, In, and Ba were observed. The In peak is due to excitation of In paste in the Si (Li) detector by a weak γ -ray emitted from the sample during the measurement. In Fig.1, e - and p -peaks are an escape peak and pile-up peak of the intense Fe K_{α} line, respectively. The K_{β} X-ray lines of Ni, Rb, Sr, and Y overlap with the K_{α} lines of Cu, Y, Zr, and Nb, respectively. When peaks for two elements overlapped, intensity for each element of interest was calculated on the basis of measurements of the K_{β} peak intensities and the previously measured K_{α}/K_{β} area intensity ratio for each element at 4-MeV proton irradiation.

The present determined values for all the elements, except for Cu, agreed well (within the RSDs) with the PIXE values at determined at Guelph University [3] (Table 1). In addition, almost all the trace-element concentrations agreed with the reference values [7] to within $\pm 7\%$ (average). These good agreements demonstrate the appropriateness of the present quantification method for almost trace elements

in a solid sample. The values of Mn, Ni, and Cu showed relatively large differences ($<20\%$). A K_{α} X-ray peak of Mn was located at the low-energy side tail (shoulder) of the intense Fe K_{α} peak. Thus, the differences for Mn may be due to a slight error in the background subtraction for the peaks of interest adjacent to the intense X-ray peaks. The large discrepancy for Cu could be ascribed to adsorption by the platinum capsule during sample preparation [3]. The difference between the present and Guelph PIXE values could also be due to a heterogeneous distribution of Cu generated by the adsorption. The Ni values determined by both PIXE show a good agreement, so the large difference between the PIXE and the reference values requires further study.

Table 1 Trace-element concentrations in JB-1a basalt glass determined by PIXE

	Present-PIXE* ($\mu\text{g g}^{-1}$)	Guelph PIXE ($\mu\text{g g}^{-1}$)	Reference ($\mu\text{g g}^{-1}$)	Dif. (%)
Cr	380 \pm 15		392	3
Mn	979 \pm 54	817 \pm 126	1150	17
Fe	62372 \pm 912	59700 \pm 2300	63300	1
Ni	115 \pm 4	118 \pm 2	139	21
Cu	34 \pm 1	26 \pm 3	56.7	65
Zn	83 \pm 1	84 \pm 6	82.1	1
Ga	16 \pm 1	18 \pm 1	17.9	9
As	2.5 \pm 0.3	3 \pm 1	2.30	8
Rb	39 \pm 4	39 \pm 4	39.2	1
Sr	433 \pm 5	464 \pm 3	442	2
Y	24 \pm 1	22 \pm 2	24	0
Zr	136 \pm 3	141 \pm 10	144	6
Nb	26 \pm 3	27 \pm 4	26	1
Ba	504 \pm 26	503 \pm 73	504	0

* Present-PIXE: average concentrations (3 replicates) and the standard deviations (1s) at the present measurements; Guelph PIXE: PIXE measurements at the Guelph University [3]; Reference: the reference values [7]; Dif.: (present-PIXE value - Reference value)/(present-PIXE value).

References

- [1] C. G. Ryan et al, Nucl. Instr. and Meth. B47(1990)55.
- [2] G. K. Czamanske et al., Amer. Mineral. 78(1993)893.
- [3] M. Kurosawa et al., Chem. Geol. 160(1999)241.
- [4] M. Kurosawa et al., Nucl. Instr. and Meth. B142(1998)599.
- [5] M. Kurosawa et al., Geochim. Cosmochim. Acta 67(2003)4337.
- [6] J.L.Campbell, Particle-Induced X-ray Emission Spectrometry (PIXE), eds. S.A.E. Johansson et al., John Wiley (New York), (1995), p19.
- [7] N. Imai et al., Geochem. J. 29(1995)91.

5.

TECHNICAL REPORT

5.1 Design of a new slit system for beam analyzing magnet

S. Ishii

According to an improvement schedule, a slit system of an energy analyzing magnet is replaced to new one. The main purpose of this replacement is to be able to control the slits from the remote section such as a control and measuring room. The adjustment of the width and/or the offset of the object and image slits were manually operated at the local control stage by a tandem operator at the request of users. These works caused undesirable interruption on the experiments because not only the operator had to enter the analyzer magnet room for the operation but also the reproducibility of the slit position was not guaranteed. Therefore, in order to improve the circumstance of the slits operation, the new slit system has been installed. The system consists of two computer controllable slit apparatuses. One is 4-hold slits apparatus and another one is 2-hold slits one.

The 4-hold, $\pm X$ and $\pm Y$, slits apparatus is installed into the object focus point of the analyzing magnet. Each slit has a motor driver and can be moved independently by the electric power. The slit driver consists of a variable speed motor and a set of torque control gear as show in Fig. 1. The slit is coupled with the motor by a precise timing belt in order to ensure the precise positioning. A precise digital dial gauge is selected as a read out appliance of the slit position. The specification of the motor driven 4-hold slit is listed up on the Table 1.

On the other hand, the 2-hold, $\pm Y$, slits apparatus is installed in the image focus point of the magnet. A model BDS6 slit system, which is distributed commercially by the NEC Co., USA, is introduced and modified. An induction motor is changed to the variable speed motor and the high precise digital dial gage is installed. The specification of the motor driven 2-hold slit is also listed up on the Table 1.

Adjustment Resolution	25 μm
Adjustment Sensitivity	1.59 mm/1turn
Power Rating	1000 W/1slit
Range of Adjustment	-7.9 mm ~ 19 mm
Cooling	Pure Water (0.5 l/min)

Table 1. Specification of The Slit Appliance

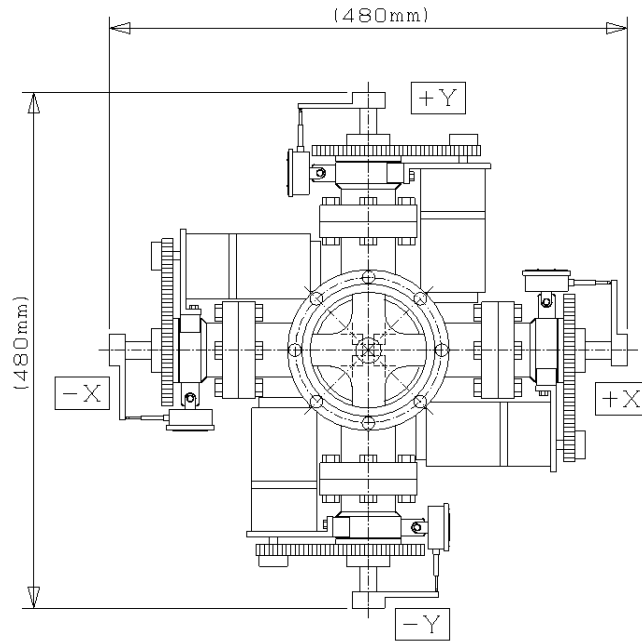


Fig. 1 Drawing of the newly designed slit control system of the object slits. It is planned to be install at the focus of the beam analyzing magnet.



Fig. 2 Photograph of the newly assembled image slit system.

5.2 Development of a beam slit controller by using XPort and Web I/O

Y. Yamato

In parallel with the installation of a newly developed remote controllable slit system, a control program has been developed. This program can operate co-currently six slits with two, Manual and Automatic, control modes. Under the Manual mode, the slit can be moved step by step with the click of a computer mouse. On the other hand, once the Automatic mode is selected, the slit can be moved automatically to the preset position. Fig. 1 shows the configuration of the control system. A slit position is read with a Digimatic Indicator ID-C112, Mitsutoyo Co. Japan. The ID-C112 works as a digital dial gauge for the position measurement. The slit position which is digitized by the ID-C112 is transferred to a RS-232C multiplexer and converted to 9600b RS-232C communication signal. The RS-232C multiplexer can throw four digital position signals into one RS-232C signal. Then, this RS-232C signal is transferred to a XPort device in which the RS-232C protocol is converted to 100Mb Ethernet protocol. Finally, a PC gets the information of the slit positions from the XPort through an Ethernet .

A slit motor, US206-401, ORIENTAL MOTOR Co. Japan, is operated with a set of a Web I/O RO-16 device and a relay terminal. The Web I/O is controlled by the PC through the Ethernet and controls the motor rotation through the relay terminal. In order to protect the device from an unexpected discharge, a PhotoMOS relay is used as an output element of the Web I/O. Total response time of the Web I/O and relay terminal is 5 ms and is sufficient for our usage.

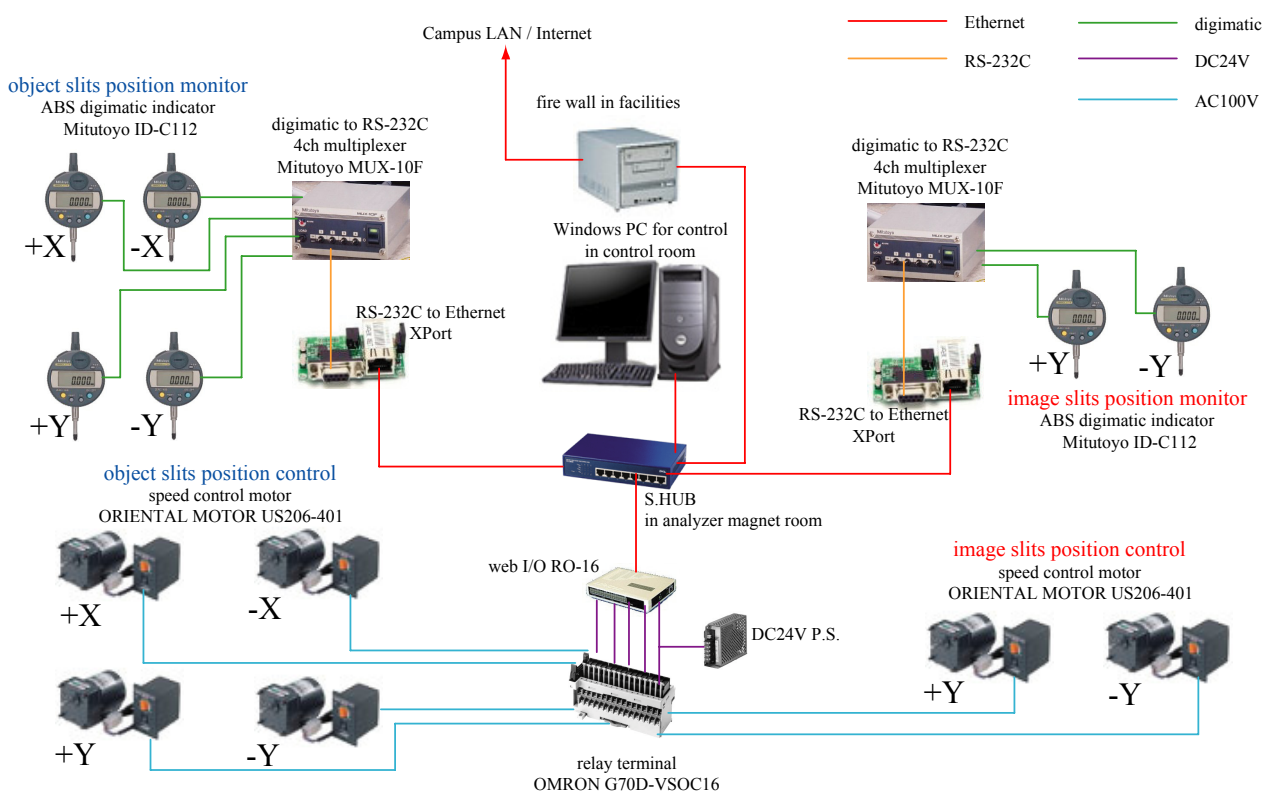


Fig.1. Control system chart.

The opening and closing speed of the slit are 0.008 mm/s and 0.04 mm/s, respectively. An emergency switch is prepared to quit the motor operations quickly when something happened. A control program is written with Visual C++ for Windows by using a multithread programming technique.

Fig. 2 shows a user interface for the slit operation. The interface is divided into two screens. The current positions of the six slits are displayed in a left side screen in Fig.2. On the other hand, the slits are controlled interactively through a right hand screen in Fig.2. The slit can be moved with the IN/OUT button operations on the right hand screen by watching the current slit position on the left hand screen. The slit can be moved also automatically. Following the set of the slit position where you want with a keyboard, the slit can be moved to the specified point by clicking the Automatic button. Six slits can be controlled simultaneously with one operation of the Automatic button. In order to protect from unexpected collision of slit, a software limit switch is installed in the program. Two kinds of programs are developed. One is a suitable for the normal usage. The slit can be moved quickly with the limited, $\sim 10 \mu\text{m}$, positioning accuracy. When the accurate positioning is requested, another program is used. The speed is about 10 times lower than that of former one but the positioning accuracy might be better. Fig. 2 and Fig.3 demonstrate the user interface of the high speed and of the high accuracy versions, respectively.



Fig.2. Screen shot about the speed priority



Fig.3. Screen shot about the highly accurate

References

- [1] Y. Yamato, The beam slits controlled by means of XPort and Web I/O, Proceedings of the technological meeting 2005, Osaka University, (2005) 3-02.
- [2] Y. Yamato, Remote control of beam slits (Example of applying XPort and Web I/O), University of Tsukuba, Technical report No.25(2005) 24-29.

6.

RELATED TOPICS

6.1 Mass measurements by isochronous storage ring in RIKEN RI beam factory

A. Ozawa, I.Arai, T.Komatsubara, K.Sasa, Y.Tagishi, M.Yamaguchi, T.Suzuki¹, T.Yamaguchi¹, T.Ohtsubo², N.Fukunishi³, A.Goto³, T.Ohnishi³, H.Okuno³, H.Takeda³, M.Wakasugi³, Y.Yamaguchi³, Y.Yano³, T.Kikuchi⁴

A mass measurement of unstable nuclei is a valuable tool in nuclear structure allowing to discover new shell effects, nuclear shapes and decay properties. Moreover, the mass measurement is important to determine the astrophysical r -process path. Presently, there are three major techniques to measure the mass of unstable nuclei; a measurement in a Penning trap [1], a measurement in heavy ion storage ring [2], and a measurement in cyclotron [3].

We propose a new scheme of precise mass measurements for short lived ($T_{1/2} < 100\text{ms}$) unstable nuclei in RIKEN RI beam factory. The scheme is based on high-energy RI beams produced by fragmentation or uranium fission. The scheme consists of three major devices, as shown in Fig. 1; 1) a long injection line to measure velocity

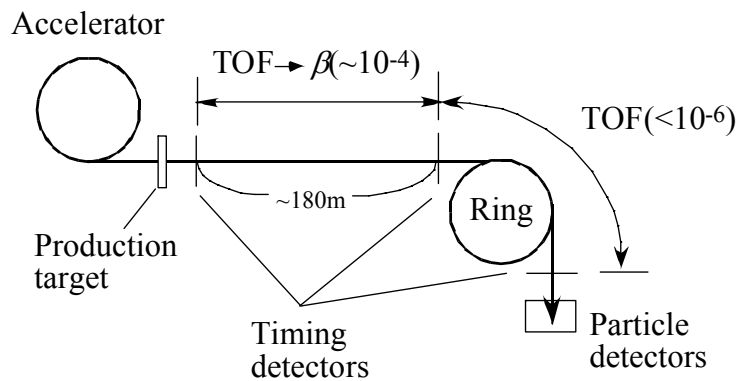


Fig.1. Proposed scheme of mass measurements

of the beams with high resolution ($\sim 10^{-4}$), 2) an injector for individual injection [4], that can be possible by the present kicker magnet technology with the long injection line, 3) an isochronous storage ring to measure TOF with high resolution ($\sim 10^{-6}$). In the isochronous ring, there is no acceleration, that provides the large acceptance for different species (different m/q). Mass resolution of $\sim 10^{-6}$ and $\sim 10^{-2}$ acceptance for m/q can be achieved by the scheme. And this scheme allows us to identify particles event-by-event mode and to correct the resolution after the measurements, that are indispensable for RI beams based on fragmentation and uranium fission. Fast response of the injector and design of the isochronous storage ring are key issues for this project. They are now in progress at University of Tsukuba and RIKEN.

References

- [1] G.Bollen, Nucl Phys. A 693 (2001) 3.
- [2] H.Geissel and H.Wollnik, Nucl Phys. A 693 (2001) 19.
- [3] M.Chartier et al., Phys. Rev. Lett. 77 (1996) 2400. .
- [4] I.Meshkov et al., Nucl. Instr. Meth. A 523 (2004) 262.

¹ Saitama University, Saitama 338-0825, Japan

² Niigata University, Niigata 950-2102, Japan

³ RIKEN, Wako, Saitama 351-0106, Japan

⁴ Utsunomiya University, Utsunomiya, Tochigi 321-0912, Japan

6.2 Design of the isochronous storage ring and the injection line for mass measurements in RIKEN RI beam factory

M. Yamaguchi¹, I. Arai¹, A. Ozawa¹, Y. Tagishi¹, T. Komatsubara¹, K. Sasa¹, T. Suzuki², T. Yamaguchi², T. Ohtsubo³, Y. Yano⁴, A. Goto⁴, M. Wakasugi⁴, H. Okuno⁴, N. Fukunishi⁴, T. Ohnishi⁴, H. Takeda⁴, Y. Yamaguchi⁵, T. Kikuchi⁶

The isochronous storage ring and the injection line for mass measurements of rare RI beams will be constructed in RIKEN RI beam factory. The measurements are going to achieve the relative uncertainty of about 10^{-6} . The conceptual design of the isochronous storage ring and the injection line was considered.

For the high accuracy, we must measure the velocities of the nuclei before the injection to the ring, so that the injection line will be a long one. In order to save the cost of the injection line, we will use magnets of the storage ring TARN-II [1] for the injection line. In our present design, vertical double achromatism was made almost through the injection line. Horizontally, the beam is dispersive one at the kicker magnet of the ring.

The isochronous storage ring consists of eight sectors magnets in the present design. The circumference is 70 m. The central orbit radius is 4.2 m. The maximum magnetic field is 1.5 Tesla. The radial width is 25 degree. The magnetic fraction is 0.55. It has eight straight sections. The length of each section is 5.5 m. The maximum beta of the injection particle is 0.57. The maximum momentum is 200 MeV/A. Momentum dispersion is $\pm 1\%$. The emittance is a few π mmmrad. Isochronicity is about 10^{-7} .

The edges of the magnets are straight ones. The tilting angle is 9.5 degrees. In this case, we can achieve the isochronicity of 10^{-4} . To achieve the isochronicity less than 10^{-4} , we should use trim coils and generate harmonic field. In the ideal case, we can achieve the isochronicity of 10^{-8} .

A computer simulation code of the isochronous ring was made. The magnetic field is calculated with hard edge approximation. Each magnetic sector are sliced into 1000 thin sectors. The trajectory in the magnetic field is circular. Magnetic field in each thin sector is uniform and equal to the value at its entrance.

Monte Carlo simulation will be made with the computer code MOCADI [2]. The beam optics of BigRIPS and the injection line is represented as a series of transfer matrices in the code. The limitation on the beam radii by the beam ducts are also incorporated. The paths of nuclei in the ring are calculated by a library function dynamically linked to MOCADI. Through this simulation, we will estimate the integrated performance of the injection line and the ring.

References

- [1] T.Katayama et al., Part. Accel. 32 (1990) 2105
- [2] N.Iwasa et al., Nucl. Instr. Meth. B126, (1997) 284

¹Univ. of Tsukuba, ²Saitama Univ., ³Niigata Univ., ⁴RIKEN, ⁵Univ. of Tokyo, CNS, ⁶Utsunomiya Univ.

6.3 Reaction of gold cluster cations with silane at high temperature

T.Sugaya, M.Kubo, K.Sugawara¹ and I.Arai

Small clusters have been intensively investigated. Especially gold clusters are of significant interest due to their pronounced difference in various properties compared with the bulk[1]. They are promising building block for electronic devices and other functional nanoscale materials. We have studied the reactivity of transition metal, vanadium, niobium, tantalum, tungsten and gold, cluster cations with pure silane SiH₄ at room temperature (300K) previously. Our present experiment intends an investigation of the reaction of gold cluster cations with SiH₄ at high temperature instead.

The experimental setup mainly consists of an external cluster source and a Fourier Transform Ion Cyclotron Resonance (FT-ICR) mass spectrometer. Gold cluster cations, Au_n⁺ (n=1-9), were produced by laser vaporization of rotating gold rod. They were introduced into an FT-ICR chamber and trapped by magnetic and electrostatic field in the FT-ICR cell heated at 493K. After the thermalization by collisions with argon atoms, the cluster ions reacted with SiH₄ whose pressure was kept at 1×10⁻⁸Torr there. We measured the mass spectra in the reaction time 0.1s-15s and obtained the reaction rate constants of Au_n⁺ (n=1-9), Au_nSi⁺ (n=1-9), Au_nSiH₂⁺ (n=1-3) with SiH₄, i.e., k1, k2, k3.

A main reaction process was the following

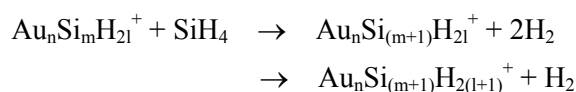


Fig.1. shows a comparison of the present results at 493K and the previous ones at 300K for reaction rate constants. It indicates that the reaction rate constants don't change appreciably in those two cases. Clusters are generally known to have the melting point lower than the bulk, and Fthenakis *et al.* reported a transition temperature much lower in value than the one produced by their calculation, in particular, ≈280-320K[2]. But our experimental results suggest that gold clusters and gold-silicon clusters don't have a transition temperature between 300K and 493K. In other words a great change of their structures such as a phase transition doesn't seem to occur in this temperature region. Furthermore while the reaction rate constant k1 of Au_n⁺ with SiH₄ is well reproduced by Langevin model, which is independent of temperature and calculated as ~1×10⁻⁹ cm³s⁻¹ in this case, reactions of Au_nSi⁺ (n=2-5) and Au_nSiH₂⁺ with SiH₄ show considerable difference from the model. It is empirically known that the reaction rate constant depends on the temperature[3]. According to it, the reaction rate constant at 493K should be about fifteen times as large as the one at 300K. However, the observed differences aren't so much. It is suggested that the reactions of Au_nSi⁺ and Au_nSiH₂⁺ with SiH₄ are different from the conventional reaction mechanism.

¹ Nanotechnology Research Institute, National Institute of Advanced Industrial Science and Technology, Tsukuba, 305-8565, Japan.

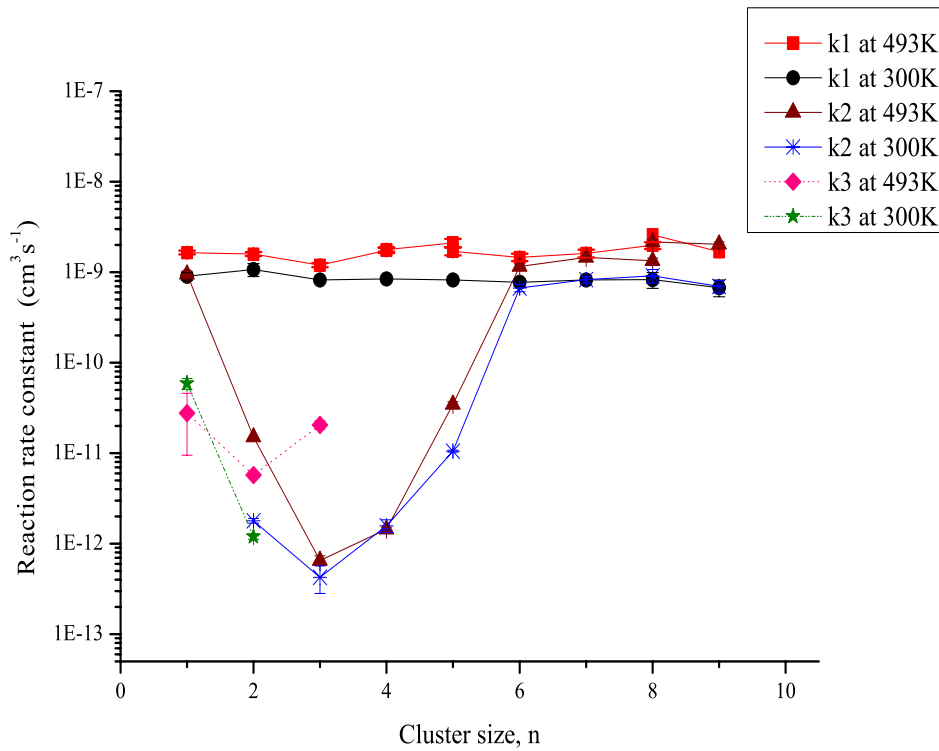


Fig.1. The reaction rate constants of Au_n^+ ($n=1-9$), Au_nSi^+ ($n=1-9$), $Au_nSiH_2^+$ ($n=1-3$) with SiH_4 , i.e., k_1 , k_2 , k_3 , at 493K and 300K.

References

- [1] D.M.Cox, R.Brickman, K.Creegan and A.Kaldor, *Z.Phys.D-Atoms, Molecules and Cluster* 19,3533 (1991)
- [2] Z.Fthenakis, A.N.Andriotis and M.Menon, *J.Chem.Phys* 119,20,22 (2003)
- [3] Y.Kaneko, *the Introduce to the Atomic Collision* (Baifukan,1999)

7. LIST OF PUBLICATIONS

The publications listed here are those released in the fiscal year 2004 by all the workers listed on §11.

7.1 Journals

ACCELERATOR AND EXPERIMENTAL FACILITIES

1. K.Sasa, I. Arai, M. kurosawa, T. Nakagawa,
“Preliminary experiments on laser coupling with an electron cyclotron resonance ion source for trace element analysis”, Rev. Sci. Instr. **75** No.5 1928-1930 (2004).
2. K.Sasa,
“Tandem Accelerator Complex at University of Tsukuba”, J. Part. Accel. Soc. Jpn. **Vol.1**, No.1, 44 (2004).
3. L. Maunoury, J.U. Andersen, H. Cederquist, B. Huber, P. Hvelplund, R. Leroy, B. Manil, J. Y. Pacquet, U.V. Pedersen, J. Rangama, S. Tomita,
“MONO1001: A source for singly charged ions applied to the production of multicharged fullerene beams”, Rev. Sci. Instr. **75**, 1884 (2004)

NUCLEAR PHYSICS

4. M. Yamaguchi, Y. Tagishi, Y. Aoki, N. Kawachi, N. Okumura, N. Yoshimaru,
“Measurement of proton polarization in the $^{208}\text{Pb}(d, p)^{209}\text{Pb}$ reaction at an incident energy of 20 MeV”, Nucl. Phys. **A747**, pp 3-13 (2005).
5. M.Petrascu, A.Constantinescu, I.Cruceru, M.Giurgiu, A.Isbasescu, M.Isbasescu, H.Petrascu, C.Bordeanu, I.Tanihata, T.Kobayashi, K.Morimoto, K.Katori, M.Chiba, Y.Nishi, S.Nishimura, A.Ozawa, T.Suda, K.Yoshida,
“Pre-emission of correlated neutrons in the fusion of ^{11}Li halo nuclei with Si targets”, Phys. Rev. **C69**, 011602(R) (2004).
6. A.Yoshida, K.Morita, K.Morimoto, D.Kaji, T.Kubo, Y.Takahashi, A.Ozawa, I.Tanihata,
“High-power rotating wheel targets at RIKEN”, Nucl. Instr. and Meth. **A521**, 65-71 (2004).
7. Z.Elekes, Zs.Dombradi, A.Krasznahorkay, H.Baba, M.Csatlos, L.Csige, N.Fukuda, Zs.Fulop, Z.Gacsi, J.Gulyas, N.Iwasa, H.Kimugawa, S.Kubono, M.Kurokawa, X.Liu, S.Michimasa, T.Minemura, T.Motobayashi, A.Ozawa, A.Saito, S.Shimoura, S.Takeuchi, I.Tanihata, P.Thirot, Y.Yanagisawa, K.Yoshida,
“Decoupling of valence neutrons from the core in ^{16}C ”, Phys. Lett. **B 586**, 34-40 (2004).

8. D.Q.Fang, T.Yamaguchi, T.Zheng, A.Ozawa, M.Chiba, R.Kanungo, T.Kato, K.Morimoto, T.Ohnishi, T.Suda, Y.Yamaguchi, A.Yoshida, K.Yoshida, I.Tanihata, "One-neutron halo structure in ^{15}C ", *Phys. Rev. C* **69**, 034613 (2004).
9. A.Ozawa, "Recent experiments for interaction and reaction cross-sections", *Nucl. Phys. A* **734**, 315-318 (2004).
10. C. Wu, Y.Yamaguchi, A.Ozawa, R.Kanungo, I.Tanihata, T.Suzuki, D.Q.Fang, T.Suda, T.Ohnishi, M.Fukuda, N.Iwasa, T.Ohtsubo, T.Izumikawa, R.Koyama, W.Shinozaki, M.Takahashi, "Study of the density distribution of ^{17}C from reaction cross section measurement", *Nucl. Phys. A* **739**, 3-14 (2004).
11. H.Jeppesen, R.Kanungo, B.Abu-Ibrahim, S.Adhikari, M.Chiba, D.Fang, N.Iwasa, K.Kimura, K.Maeda, S.Nishimura, T.Ohnishi, A.Ozawa, C.Samanta, T.Suda, T.Suzuki, I.Tanihata, Q.Wang, C.Wu, Y.Yamaguchi, K.Yamada, A.Yoshida, T.Zheng, "One- and two-neutron removal from ^{15}O ", *Nucl. Phys. A* **739**, 57-66 (2004).
12. K.Morita, K.Morimoto, D.Kaji, H.Haba, E.Ideguchi, J.C.Peter, R.Kanungo, K.Katori, H.Koura, H.Kudo, T.Ohnishi, A.Ozawa, T.Suda, K.Sueki, I.Tanihata, H.Xu, A.V.Yeremin, A.Yoneda, A.Yoshida, Y.-L.Zhao, T.Zheng, S.Goto, F.Tokanai, "Production and Decay Properties of $^{272}111$ and its Daughter Nuclei", *J. Phys. Soc. Jpn.* **73**, 1738-1744 (2004).
13. A.Ozawa, "Reaction cross-sections for carbon isotopes", *Nucl. Phys. A* **738**, 38-44 (2004).
14. A.Ozawa, "Measurements of Reaction Cross-Sections and Determination of Nucleon Matter Density Distributions", *Horizons in World Physics*, **Vol. 244**, 301-321 (2004).
15. D.Cortina-Gil, J.Fernandez-Vazquez, F.Aumann, T.Baumann, J.Benlliure, M.J.G.Borge, L.V.Chulkov, U.Datta Pramanik, C.Forssen, L.M.Fraile, H.Geissel, J.Gerl, F.Hammache, K.Itahashi, R.Janik, B.Jonson, S.Mandal, K.Markenroth, M.Meister, M.Mocko, G.Munzenberg, T.Ohtsubo, A.Ozawa, V.Prezado, V.Pribora, K.Riisager, H.Scheit, R.Schrieder, G.Schrieder, H.Simon, B.Sitar, A.Stolz, P.Strmen, K.Summerer, I.Szarka, H.Weick, "Shell structure of the near-dripline nucleus ^{23}O ", *Phys. Rev. Lett.* **93**, 062501 (2004).
16. M.Chiba, R.Kanungo, B.Abu-Ibrahim, S.Adhikari, D.Q.Fang, N.Iwasa, K.Kimura, K.Maeda, S.Nishimura, T.Ohnishi, A.Ozawa, C.Samanta, T.Suda, T.Suzuki, I.Tanihata, Q.Wang, C.Wu, Y.Yamaguchi, K.Yamada, A.Yoshida, T.Zheng, "Neutron removal studies on ^{19}C ", *Nucl. Phys. A* **741**, 29-41 (2004).
17. K.Morita, K.Morimoto, D.Kaji, T.Akiyama, S.Goto, H.Haba, E.Ideguchi, R.Kanungo, K.Katori, H.Koura, H.Kudo, T.Ohnishi, A.Ozawa, T.Suda, K.Sueki, H.Xu, T.Yamaguchi, A.Yoneda,

- A. Yoshida, Y.-L. Zhao,
 “Experiments on the Synthesis of Element 113 in the reaction $^{209}\text{Bi}(^{70}\text{Zn}, n)^{278}113$ ”, *J. Phys. Soc. Jpn.* **73**, 2593-2596 (2004).
18. Z. Elekes, Zs. Dombradi, A. Saito, N. Aoi, H. Baba, K. Demichi, Zs. Fulop, J. Gibelin, T. Gomi, H. Hasegawa, N. Imai, M. Ishihara, H. Iwasaki, S. Kanno, S. Kawai, T. Kishida, T. Kubo, K. Kurita, Y. Matsuyama, S. Michimasa, T. Minemura, T. Motobayashi, M. Notani, T. Ohnishi, H. J. Ong, S. Ota, A. Ozawa, H. K. Sakai, S. Shimoura, E. Takeshita, S. Takeuchi, I. Tanihata, M. Tamaki, Y. Togano, K. Yamada, Y. Yanagisawa, K. Yoneda,
 “Bound excited states in ^{27}F ”, *Phys. Lett.* **B 599**, 17-22 (2004).
19. Y. Yamaguchi, C. Wu, T. Suzuki, A. Ozawa, D. Q. Fang, M. Fukuda, N. Iwasa, T. Izumikawa, H. Jeppesen, R. Kanungo, R. Koyama, T. Ohnishi, T. Ohtsubo, W. Shinozaki, T. Suda, M. Takahashi, I. Tanihata,
 “Density distribution of ^{17}B from a reaction cross-section measurement”, *Phys. Rev.* **C 70**, 054320 (2004).
20. K. Matsuta, Y. Tagishi, T. Nagatomo, H. Fujiwara, M. Yamaguchi, A. Ozawa, T. Yasuno, A. Chiba, M. Fukuda, M. Mihara, K. Minamisono, T. Minamisono,
 “Production of polarized ^{20}F by polarized deuteron beam and the beta-ray angular distribution”, *Genshikaku Kenkyu*, **Vol. 49**, No. 4, 31-36 (2005).
21. R. J. Li, Y. J. Ma, X. G. Wu, Y. H. Zhang, L. H. Zhu, S. Y. Wang, M. F. Li, G. D. Liang, X. Z. Cui, X. F. Li, G. Y. Zhao, J. B. Lu, Y. Z. Liu, Z. M. Wang, G. S. Li, S. X. Wen, C. X. Yang, T. Komatsubara, K. Furuno,
 “Identification of high-spin states in odd-odd ^{126}I ”, *High Energy Physics and Nuclear Physics-Chinese Edition* **29** (1): 1-4 (2004).
22. C. Y. Xie, X. H. Zhou, Y. Zheng, Y. H. Zhang, Z. Liu, Z. G. Gan, T. Hayakawa, M. Oshima, T. Toh, T. Shizuma, J. Katakura, Y. Hatsukawa, M. Matsuda, H. Kusakari, M. Sugawara, K. Furuno, T. Komatsubara,
 “Level structure of ^{146}Tb ”, *Eur. Phys. J.* **A19**, pp.7-9 (2004).
23. C. B. Moon, T. Komatsubara, K. Furuno,
 “Band structures in ^{116}I ”, *Nucl. Phys.* **A730**, pp.3-22 (2004).
24. C. B. Moon, T. Komatsubara,
 “Yrast band based on the proton $h(11/2)$ orbital in ^{125}I ”, *Journal of the Korean Physical Society* **45** (4): L791-L794 OCT (2004).
25. S. Y. Wang, Y. J. Ma, T. Komatsubara, Y. Z. Liu, Y. H. Zhang, K. Furuno, T. Hayakawa, J. Mukai, Y. Iwata, T. Morikawa, G. B. Hagemann, G. Sletten, J. Nyberg, D. Jerrestam, H. J. Jensen, J. Espino, J. Gascon, N. Gjorup, B. Cedervall, P. O. Tjom,
 “Structure of the $\pi g(7/2) [404]7/2(+)$ band in odd proton nucleus ^{123}I ”, *Chinese Physics Letters* **21** (6): 1024-1026 JUN (2004).

26. S.Y. Wang, Y.J. Ma, T. Komatsubara, Y.Z. Liu, Y.H. Zhang, G.D. Liang, K. Furuno, T. Hayakawa, J. Mukai, Y. Iwata, T. Morikawa, G.B. Hagemann, G. Sletten, J. Nyberg, D. Jerrestam, H.J. Jensen, J. Espino, J. Gascon, N. Gjomp, B. Cederwall, P.O. Tjom, "High-spin level scheme of ^{126}Cs ", High Energy Physics and Nuclear Physics-Chinese Edition **28** (5): 491-494 MAY (2004).
27. P. Luo, Y.H. Zhang, X.H. Zhou, M.L. Liu, Y.X. Guo, Z. Liu, X.G. Lei, L.T. Song, Y. Zheng, H.L. Wang, H.P. Yu, C.Y. Xie, Y.J. Ma, Y. Sasaki, K. Yamada, H. Ohshima, S. Yokose, M. Ishizuka, T. Komatsubara, K. Furuno, "Experimental observation of high spin states in ^{135}La nucleus", High Energy Physics and Nuclear Physics-Chinese Edition **28** (5): 495-501 MAY (2004).
28. Y. Zheng, X.H. Zhou, Y.H. Zhang, T. Hayakawa, M. Oshima, Y. Toh, T. Shizuma, J. Katakura, Y. Hatsukawa, M. Matsuda, H. Kusakari, M. Sugawara, K. Furuno, T. Komatsubara, "Multi-quasiparticle excitations in ^{145}Tb ", Journal of Physics G-Nuclear and Particle Physics **30** (4): 465-479 APR (2004).
29. P. Luo, M.L. Liu, Z. Liu, Y.H. Zhang, X.H. Zhou, Y.X. Guo, Y.J. Ma, Y. Sasaki, K. Yamada, H. Ohshima, S. Yokose, M. Ishizuka, T. Komatsubara, K. Furuno, "In-beam gamma-ray spectroscopy of level structure in ^{134}Ba ", High Energy Physics and Nuclear Physics-Chinese Edition **28** (3): 268-273 MAR (2004).
30. T. Hayakawa, N. Iwamoto, T. Shizuma, T. Kajino, H. Umeda, K. Nomoto, "Evidence for nucleosynthesis in the supernova γ process: Universal scaling of for p nuclei", Phys. Rev. Lett. **93**, 161102-1-4 (2004).

ATOMIC AND SOLID STATE PHYSICS, AND CLUSTER SCIENCE

31. H. Kudo, M. Nagata, H. Wakamatsu, S. Tomita, "Resonant coherent excitation of C^{5+} in Si observed with backward electron spectroscopy", Nucl. Instr. and Meth. **B229**, 227-231 (2005).
32. B. Liu, P. Hvelplund, S.B. Nielsen, S. Tomita, "Formation of C_{60}^{2-} in collisions between C_{60}^{-} and Na atoms", Phys. Rev. Lett. **92**, 168301 (2004).
33. M.R. Calvo, J.U. Andersen, P. Hvelplund, S.B. Nielsen, U.V. Pedersen, J. Rangama, S. Tomita, J.S. Forster, "Photophysics of protoporphyrin ions in vacuo: Triplet-state lifetimes and quantum yields", J. Chem. Phys. **120**, 5067 (2004).
34. J.U. Andersen, H. Cederquist, J.S. Forster, B.A. Huber, P. Hvelplund, J. Jensen, B. Liu, B. Manil, L. Maunoury, S.B. Nielsen, U.V. Pedersen, J. Rangama, H.T. Schmidt, S. Tomita, H.

- Zettergren,
 “Photodissociation of protonated amino acids and peptides in an ion storage ring. Determination of Arrhenius parameters in the high-temperature limit”, *Phys. Chem.* **5**, 2676-2681 (2004).
35. B. Liu, P. Hvelplund, S.B. Nielsen, S. Tomita,
 “Hydrogen loss from nucleobase nitrogens upon electron attachment to isolated DNA and RNA nucleotide anions”, *J. Chem. Phys.* **121**, 4175-5179 (2004).
36. J. Jensen, H. Zettergren, H.T. Schmidt, H. Cederquist, S. Tomita, S.B. Nielsen, J. Rangama P. Hvelplund, B. Manil, B.A. Huber,
 “Ionization of C₇₀ and C₆₀ molecules by slow highly charged ions: A comparison”, *Phys. Rev.* **A69**, 053203 (2004).
37. S.B. Nielsen, J.U. Andersen, P. Hvelplund, B. Liu, S. Tomita,
 “Biomolecular ions in accelerators and storage rings”, *J. Phys. B: At. Mol. Opt. Phys.* **37**, R25-56 (2004).
38. A. Negishi, N. Kariya, K.I. Sugawara, I. Arai, H. Hiura, T. Kanayama,
 “Size-selective formation of tungsten cluster-containing silicon cages by the reactions of W_n⁺ (n=1~5) with SiH₄,” *Chem. Phys. Lett.*, **388**, 463-467 (2004).
39. M. Onoda, T. Ohki, Y. Uchida,
 “The role of two types of trellis layer for metal-insulator transition and antiferromagnetic order in the one-dimensional conductor V₆O₁₃”, *J. Phys.: Condens. Matter* **16** No 43, 7863-7871, 3 November (2004).
40. M. Onoda,
 “The crystal structures and quasi-one-dimensional electronic properties of Ag_{1+x}V₃O₈ and Na_{1+x}V₃O₈”, *J. Phys.: Condens. Matter* **16** No 49, 8957-8969 (15 December 2004).
41. Y. Hata, Y. Mihara, T. Mochiku, J. Suzuki, I. Kakeya, K. Kadowaki, E. Kita, H. Yasuoka,
 “Redistribution of Fe ion and superconductivity of FeSr₂YCu₂O_{6+y} system”, *Physica C*, **417**, 17-24 (2004).

ION BEAM ANALYSIS AND APPLICATION

42. Y. Nagashima, R. Seki, T. Matsuihiro, T. Takahashi, K. Sasa, K. Sueki, M. Hoshi, S. Fujita, K. Shizuma, H. Hasai,
 “Chlorine-36 in granite samples from the Hiroshima A-bomb site”, *Nucl. Instr. and Meth.* **B223**, pp 782-787, (2004).

43. K. Furuno, M. Kurosawa, T. Komatsubara, K. Sasa, Y. Yamato, S. Ishii, H. Oshima,
“Development of a method for the quantitative analysis of hydrogen in minerals with a high-energy proton microbeam”, *Japanese Magazine of Mineralogical and Petrological Sciences*, **33**, 51 (2004).
44. K. Awazu, M. Fujimaki, Y. Ohki, T. Komatsubara
“Three-dimensional lithography for rutile TiO₂ single crystals using swift heavy ions”, Engineered porosity for microphotonics and plasmonics/MRS proceedings (Wehrspohn Garcia-Vidal Notomi Scherer) **Vol. 797**, No. 1, pp. 69-74 (2004).
45. K. Kitazato, M. Kurosawa,
“Highly-silicic glass inclusions in eucrites and diogenites”, *Antarctic Meteorite Research*, Proceedings of the NIPR Symposium on Antarctic Meteorites, **17**, 200-208 (2004).

7.2 International conferences

1. H. Kudo,
“Energy spectra of electrons emitted from solids bombarded by MeV atom clusters”, Satellite Int. symposium of IISC-15 “*Interaction of Particle Beams with Matter*” Okayama, Oct. 14-15 (2004).
2. H. Kudo, S. Tomita, W. Iwazaki, R. Uchiyama, M. Furutani, H. Wakamatsu, T. Shimada, K. Shima, K. Sasa, S. Ishii, JAERI:K. Narumi, H. Naramoto, Y. Saitoh, S. Yamamoto,
“Energy spectra of electrons emitted from solids bombarded by MeV atom clusters”, 15th International Workshop on Inelastic Ion-Surface Collisions, Ise-Shima, Japan, Oct. 18-22, (2004)
3. S. Tomita, J.U. Andersen, B. Concina, P. Hvelplund, B. Liu, S.B. Nielsen, H. Cederquist, J. Jensen, H.T. Schmidt, H. Zettergren, B. Manil, B.A. Huber, J. Rangama,
“Decay of C₆₀²⁻ formed in collisions of C₆₀⁻ with Na”, 12th International Symposium on Small Particles and Inorganic Clusters (ISSPIC-12), September 6-10, Nanjing, China (2004).
4. H. Tanimoto, N. Yagi, H. Mizubayashi,
“Giant Irradiation Effects in FCC Nanocrystalline Metals”, International Symposium on Metastable, Mechanically Alloyed and Nanocrystalline Materials (ISMANAM) 2004, August 22 - 26, Sendai, Japan (2004).
5. K. Satou, K. Komatsubara, K. Sasa, S. Ishii, Y. Yamato, K. Miyakawa, M. Kurosawa,
“Hydrogen analysis for geoscience by using nuclear micro beam”, The 5th Italy-Japan Symposium, *Recent Achievements and Perspectives in Nuclear Physics*, (**INVITED TALK**), Naples, November 3-6 (2004).

6. K. Awazu, Y. Nagasawa, Y. Ohki, T. Komatsubara

Photonic crystals of titanium dioxide fabricated by the swift heavy ions, the 22nd international conference on nuclear tracks in solids, (*INVITED TALK*), Barcelona, Spain, Oct. 27th (2004).

8. THESES

Ph. D. Theses

Akio Kiyomichi Study of identified hadron spectra and yields at mid-rapidity in $\sqrt{s_{NN}} = 200$ GeV Au+Au Collisions

M. Sc. Theses

Masaya Oka Measurement of yield and identified charged hadron at intermediate p_T range in Au+Au collisions · $\sqrt{s_{NN}} = 200$ GeV from RHIC-PHENIX experiment

Masashi Iijima $^{118}\text{Sn}(d,p_0)$ reaction below Coulomb barrier

Yoshihiko Nagata Charged hadron identification with aerogel cherenkov counter and electro-magnetic Calorimeter at RHIC-PHENIX experiment

Takayuki Kawagishi Measurement of HBT interferometry at $\sqrt{s_{NN}} = 200$ GeV Au+Au collisions

Tomoyasu Shohjo Research and development of time projection chamber for cosmic ray test

Shinsuke Hamajima Simulation of gas aggregation cluster source by means of DSMC method

Takuya Shinba Measurements of analyzing powers for the $^6\text{Li}+d$ reaction at deuteron energy of 110keV

Toshiki Suzuki Time-of-flight mass spectrometry of neutral cluster produced by gas-aggregation cluster source

Tomohiro Shimada Sputtering by Al molecular ions

9. SEMINARS

<u>Date</u>	<u>Title and Speaker</u>
2004	
May	12 Polarized ^3He target for low-energy charged particle scattering experiments: <i>T. Katabuchi (North Carolina State Univ.)</i>
Jun	23 Cancer diagnosis and therapeutic use of an endogenous chromophore, porphyrin: <i>H. Matsui (Univ. of Tsukuba, Inst. of Clinical Medicine)</i>
Nov.	12 Study of single particle spectra and yields at mid-rapidity in $\sqrt{s_{NN}} = 200$ GeV Au+Au collisions: <i>A. Kiyomichi (RIKEN)</i>
Dec.	15 Measurement of yield and identified charged hadron at intermediate p_T range in Au+Au collisions $\cdot \sqrt{s_{NN}} = 200$ GeV from RHIC-PHENIX experiment: <i>M. Oka (Univ. of Tsukuba)</i>
Dec.	15 $^{118}\text{Sn}(d,p_0)$ reaction below Coulomb barrier: <i>M. Iijima (Univ. of Tsukuba)</i>
Dec.	22 Charged hadron identification with aerogel Cherenkov counter and electromagnetic calorimeter at RHIC-PHENIX experiment: <i>Y. Nagata (Univ. of Tsukuba)</i>
Dec.	22 Measurement of HBT Interferometry at $\sqrt{s_{NN}} = 200\text{GeV}$ Au+Au collisions: <i>T. Kawagishi (Univ. of Tsukuba)</i>
2005	
Jan.	6 Study of identified hadron spectra and yields at mid-rapidity in $\sqrt{s_{NN}} = 200$ GeV Au+Au collisions: <i>A. Kiyomichi (RIKEN)</i>
Jan.	12 Research and development of time projection chamber for cosmic ray test: <i>T. Shohjo (Univ. of Tsukuba)</i>
Jan.	19 Simulation of gas aggregation cluster source with use of DSMC method: <i>S. Hamajima (Univ. of Tsukuba)</i>
Jan.	19 Measurement of analyzing powers for the $^6\text{Li}+d$ reaction at deuteron energy of 110keV: <i>T. Shinba (Univ. of Tsukuba)</i>
Jan.	26 Time-of-flight mass spectrometry of neutral cluster produced by gas-aggregation cluster source: <i>T. Suzuki (Univ. of Tsukuba)</i>
Feb.	16 Study of identified hadron spectra and yields at mid-rapidity in $\sqrt{s_{NN}} = 200$ GeV Au+Au collisions: <i>A. Kiyomichi (RIKEN)</i>

10. SYMPOSIA

Polarization Phenomena in light ion reactions

26 November, 2004

Room C305, Tandem Accelerator Complex,

Research Facility Center for Science and Technology, University of Tsukuba

1. Opening remark : *Y.Aoki (Univ. of Tsukuba)*
2. Polarization Physics at UTTAC : *Y.Tagishi (Univ. of Tsukuba)*
3. ${}^6\text{Li}(d,p)$ and (d,α) reactions at very low energies : *Y.Yamaguchi (Univ. of Tsukuba)*
4. Spin tensor decomposition of scattering amplitudes and its applications : *M.Tanifuji (Hosei Univ.)*
5. Study of low energy ${}^2\text{H}(d,p){}^3\text{H}$ reaction by using four body Faddeev-Yakubovsky equation : *E.Uzu (Science University of Tokyo)*
6. Production of ${}^{20}\text{F}$ by using polarized deuterons and its beta-ray angular distributions : *K.Matsuta (Osaka Univ.)*
7. Some topics in SPIN2004 : *K.Hatanaka (RCNP)*
8. Polarize target now and then : *N.Horikawa (Chubu Univ)*
9. Physics on unstable nuclear beam and polarized target : *T.Uesaka (CNS)*
10. Folding model analysis of elastic scattering of ${}^6\text{He}$ from polarized protons : *Y.Iseri (Chiba-Keizai Univ.)*
11. Brain science by using fMRI of mm size resolving powers : *K.Katori*
12. Study of Gamow-Teller transitions by using high resolution $({}^3\text{He},t)$ reactions : *Y.Simbara (Osaka Univ.)*
13. Probing three body forces by using medium energy proton-deuteron scattering : *K.Sekiguchi (RIKEN)*
14. Transfer reaction and resonant behavior in low energy $\alpha+{}^6\text{He}$ scattering : *M.Itoh (Univ. of Tsukuba)*
15. Direct measurement of formation cross sections of (α, n) reaction by using short lived ${}^8\text{Li}$ beams : *H.Ishiyama (KEK)*
16. Developing CDCC program for heavy ion reactions and its application to elastic scattering of ${}^8\text{Li}$ from ${}^{208}\text{Pb}$: *Y.Aoki (Univ. of Tsukuba)*
17. Closing remark : *M.Tanifuji (Hosei Univ.)*

Atomic-collision-induced electronic excitation and related phenomena 2005

17-18 March, 2005

Room C305, Tandem Accelerator Complex,

Research Facility Center for Science and Technology, University of Tsukuba

1. Opening address: *H. Kudo (Univ. of Tsukuba)*
2. Atomic processes in the collisions of MeV light ions and atoms: *K. Ishii (Tohoku Univ.)*
3. Analysis of fluid inclusion in crust by means of PIXE: *M. Kurosawa (Univ. of Tsukuba)*
4. 20-year research and development of carbon foils and reminiscence of Professor Shima: *I. Sugai (KEK)*
5. Stopping power and charge exchange for heavy ions in plasma: *Y. Oguri (Tokyo Inst. Tech.)*
6. Charge exchange data and density effect for 6 MeV/u heavy ions passing through thin foils: *Y. Sato (National Inst. Radiological Sciences)*
7. Stopping powers in the high-velocity region: *N. Sakamoto (Nara Women's Univ.)*
8. Electronic excitation and ionization of projectiles and targets in the collision of MeV energy ions: *K. Shima (Univ. of Tsukuba)*
9. New horizons of atomic collision studies with MeV ions and liquid targets: *A. Itoh (Kyoto Univ.)*
10. Production of charged liquid drops for EUV emission and micro-particle production: *H. Shibata (Kyoto Univ.)*
11. Abnormal energy loss of low energy ions passing through an ultra-thin carbon film: *T. Hattori (Tokyo Inst. Tech.)*
12. Present status of micro-fabrication using heavy ion beams: *K. Awazu (AIST)*
13. Interactions of GeV heavy ions with materials –from fundamental processes to applications for material modifications: *A. Iwase (Univ. of Osaka Pref.)*
14. Research activities with ion beams at UTTAC: *K. Sasa (Univ. of Tsukuba)*
15. Time evolution of reversible transformations of metal films induced by fast ion irradiation: *H. Tsuchida (Kyoto Univ.)*
16. Measurements of electrons emitted from carbon foils bombarded by fast carbon clusters: *S. Tomita (Univ. of Tsukuba)*
17. Resonant coherent excitation of multiply ionized heavy ions by quasi-photons in a crystal field: *T. Azuma (Tokyo Metropolitan Univ.)*
18. Closing address: *K. Shima (Univ. of Tsukuba)*

11. LIST OF PERSONNEL

Tandem Accelerator Complex

H. Kudo	Director, Professor
K. Shima	Professor
T. Komatsubara	Assistant Professor
K. Sasa	Assistant Professor
S. Ishii	Mechanical Engineer
H. Kimura	Computer Engineer
H. Oshima	Electric Engineer
Y. Tajima	Mechanical Engineer
T. Takahashi	Electric Engineer
Y. Yamato	Electric Engineer
K. Satou	Research Fellow
R. Seki	Technical Assistant
M. Ohki	Administrative Staff

Scientific Guests and Fellows

K. Awazu	National Lab. Advanced Industrial Science and Technology
Y. Nagasawa	Waseda Univ.
T. Ikeda	Waseda Univ.
M. Ebihara	Tokyo Metropolitan Univ.
T. Ohura	Tokyo Metropolitan Univ.
S. Ryuhan	Tokyo Metropolitan Univ.
H. Ishiyama	KEK
H. Miyatake	KEK
Jong Junsan	KEK
N. Yoshikawa	KEK
M. Tanaka	KEK
Y. Watanabe	KEK
T. Hayakawa	JAERI
T. Shizuma	JAERI
H. Sasaki	Tsukuba Nano-Tech.
T. Toriyama	Musashi Institute of Technology
T. Kawahata	Musashi Institute of Technology
T. Iizuka	Musashi Institute of Technology
S. Nishimura	RIKEN
M. Nishimura	RIKEN
T. Kishida	RIKEN
S. Kubono	CNS
H. Yamaguchi	CNS
A. Saito	CNS
He Jianjun	CNS
H. Fujikawa	CNS
A. Guilherme	CNS
Y. Wakabayashi	Kyushu Univ.
N. Okumura	Nagano College of Technology
K. Matsuta	Osaka Univ.

T. Mihara	Osaka Univ.
T. Nagatomo	Osaka Univ.
H. Fujiwara	Osaka Univ.
S. Kamishiro	Osaka Univ.
I. Sugai	KEK
Y. Takeda	KEK
M. Oyaizu	KEK
H. Kawakami	KEK
Jan San	China Institute of Atomic Energy

Research Members

Inst. of Physics

T. Aoki	Y. Aoki	I. Arai	S. Esumi	S. Katoh
T. Komatsubara	Y. Miake	M. Onoda	A. Ozawa	K. Sasa
K. Satou	Y. Tagishi	M. Yamaguchi		

Inst. of Applied Physics

E. Kita	H. Kudo	K. Shima	N. Tomita	A. Uedono
H. Yanagihara				

Inst. of Material Science

T. Koyano	H. Mizubayashi	K. Takita	H. Tanimoto	
-----------	----------------	-----------	-------------	--

Inst. of Geoscience

M. Kurosawa	K. Suzaki	N. Tase		
-------------	-----------	---------	--	--

Inst. of Chemistry

K. Sueki

Inst. of Basic Medical Science

Y. Nagashima

Graduate Students

Doctoral Degree Programs of Pure and Applied Science

Y. Fujii	K. Fujiwara	D. Fukuhara	M. Furutani	J. Hasegawa
M. Hasegawa	A. Hatanaka	S. Igarashi	T. Ikeda	K. Ikeuchi
Y. Ishibashi	T. Isobe	Y. Ito	M. Konno	M. Kubo
H. Masui	K. Masuo	K. Miki	K. Miyakawa	Y. Nagata
Y. Nakamura	M. Nakazumi	M. Narisawa	M. Oka	A. Rikukawa
S. Sakai	T. Satou	J. Sawahata	K. Shibata	Y. Shimizu
M. Shimomura	S. Takagi	K. Takao	H. Tokano	R. Uchiyama
K. Uehara	N. Umada	H. Wakamatsu	N. Yagi	K. Yamagishi
T. Yasuno				

Master's Degree Programs of Science and Engineering

T. Hinuma	M. Iijima	T. Kawagishi	T. Shimada	T. Shinba
T. Shojo	S. Suzuki	Y. Tsuruga	H. Uematsu	

Master's Degree Programs of Environmental Science

Y. Tosaki

Undergraduates

J. Baba

H. Kasai

T. Nishimura

T. Sugaya

A. Chiba

H. Kato

A. Sasaki

T. Takahashi

T. Ebisawa

N. Kawai

E. Sato

R. Tanabe

K. Ishibashi

A. Kondo

R. Sawai

A. Yamada

T. Ishikawa

H. Mishiba

Y. Sinmura

S. Yoda